Applications of Micro/Nanoscale Optical Resonators: Plasmonic Photodetectors and Double-Disk Cavity Optomechanics

Thesis by

Jessie Rosenberg

In Partial Fulfillment of the Requirements

for the Degree of

Doctor of Philosophy

California Institute of Technology

Pasadena, California

2010

(Defended December 8, 2009)

To my mother, father, and all of the friends, near and far, who have supported me.

Acknowledgments

First and foremost, I want to thank my advisor, Professor Oskar Painter. Your scientific brilliance, creativity, and boundless energy will forever serve as an inspiration.

Thanks, also, to Qiang Lin. You have always been so generous with your knowledge, and never balked at answering any question, seemingly trivial or otherwise. Our collaboration over these past months has been an experience of immeasurable value for me.

Thanks to Raviv Perahia, for your companionship through five years and three different offices; for all the conversations, and questions, and answers. It's been a delight. Thanks, also, to my other officemates, past and present: Orion Crisafulli, Qiang Lin, Thiago Alegre.

Thanks to the senior members of the group, Kartik Srinivasan, Paul Barclay, Matt Borselli, and Tom Johnson, for the truly phenomenal amount of work you put in to get the group started, and for sharing that knowledge and experience with those of us who followed. Thanks to Darrick Chang, for so many fruitful discussions.

Thanks to the recently graduated and current members of the group, Raviv Perahia, Chris Michael, Matt Eichenfield, Thiago Alegre, Ryan Camacho, Jasper Chan, Amir Safavi-Naeini, Jeff Hill, Alex Krause, Daniel Chao, Chaitanya Rastogi, and Justin Cohen, for making the group such a dynamic and vibrant scientific environment. Thanks to the old guard for sharing knowledge and discoveries and stories along the way, and thanks to the new students for carrying everything on into the future - and hopefully doing it all even better than we did.

Thanks to Professor Sanjay Krishna's group at the University of New Mexico, for such a valuable collaboration, and for being so welcoming to a visitor. In particular, thanks to Rajeev Shenoi, for the work we did together, and for being a great host.

Thanks to all the excellent staff at Caltech, who always were willing to contribute their time to help out.

Thanks to all of my friends, Caltech students or otherwise, nearby or far away. I can't even begin to name everyone who had such an impact, but know that you are valued. In particular, a

heartfelt thanks to Eve Stenson, Neil Halelamien, Megan Nix, Jen Soto, and Jay Daigle. Thanks to every person on the organizational team of the Caltech Ballroom Dance Club.

Thanks, above all, to my mother and father, for being the best and most supportive parents I could have asked for.

Thanks, everyone.

Abstract

Optical resonators present the potential to serve vital purposes in many emergent technologies that require spectral filtering, high optical intensities, or optical delays. By scaling down the optical resonators to the micro or nanoscale, the relevant phenomena can increase significantly in magnitude, while the device geometries become suitable for chip-scale and integrated processing. In this thesis, research is presented on several valuable resonator geometries and implementations, beginning with a more standard all-optical design, and continuing on to investigate the novel phenomena and applications which are made possible when optical and mechanical structures can be synergistically combined.

First, the design and experimental implementation of a plasmonic photonic crystal spectral and polarization filtering element is presented. This resonator scheme, in addition to allowing for a tailorable frequency and polarization response for single detector pixels, also increases the absorption of a thin layer of detector material by utilizing the unique optical properties of metal to confine light more tightly within the detector active region. Demonstrated in the valuable mid-infrared regime, this method of producing pixel-integrated multispectral detectors could find application in biological sensing and spectroscopy, missile tracking and guidance, and night vision.

Following this discussion, progress is presented in the relatively new field of cavity optomechanics: utilizing mechanically compliant optical resonators to couple to, control, and read out mechanical motion via optical forces. The use of optical resonators allows the generally weak optical forces to be increased in strength by orders of magnitude due to the many passes light makes within the resonator, while miniaturizing optomechanical devices into a convenient form factor for on-chip applications. Using a fully silicon-compatible double-disk-geometry optomechanical resonator, extremely large optomechanical coupling and very high optical quality factors are shown, enabling the demonstration of regenerative mechanical amplification, high compression factor optomechanical cooling, coherent mechanical mode mixing, and wide-bandwidth all-optical wavelength routing. Applications to ground-state cooling of mesoscopic devices, tunable optical buffering, photonic-

phononic quantum state transfer, channel routing/switching, pulse trapping/release, and tunable lasing are discussed.

Contents

List of Figures

List of Tables

Preface

The startup of a research lab, especially one with such an extensive range of facilities, is a truly overwhelming proposition requiring a daunting amount of effort. I was fortunate enough to join the group at a rather fortuitous time, when the group was mature enough to have essentially all fully functioning labs, but all of the original group members, with their tremendous experience born from setting up everything in the lab, were still around and generously willing to share their knowledge.

I immediately began work on a project started by Kartik Srinivasan and Raviv Perahia, that I imagined would occupy my entire graduate career: the patterning of photonic crystals in metal films, to create spectrally sensitive pixels in mid-infrared detector material grown by our collaborators, Prof. Sanjay Krishna's group at the University of New Mexico. Though undoubtedly fraught with unforeseeable complexities, the path to working devices seemed straightforward, and dovetailed well with the many other photonic crystal efforts then under investigation in the lab.

My first major task, occupying nearly the entirety of my first summer in the lab, was to become a fully functional user of our group cleanroom. We patterned some initial devices, and I also got started learning about theory and doing some modeling in Matlab, as well as becoming familiar with our group's home-built finite difference time domain code. With some initial dubious successes on the processing front, I also spent time working with Orion Crisafulli in doing a thorough investigation of the properties of metal-insulator-metal waveguides, which became quite useful later.

With a full plate of classwork interspersed, this occupied the first few years of my graduate career, splitting my time between experiment and theory. We made several sets of photonic crystal devices, but never saw clear resonant spectral enhancement correlating with the photonic crystal patterns, which baffled us for quite some time. In the end, we finally realized that, due to the particulars of the device fabrication, the apertures that we were patterning photonic crystals on were, in fact, only a small fraction of the open area of the devices: there was a large outer area of exposed detector material that had no photonic crystal patterning or covering of metal, and this background scattering was completely overwhelming our signal.

After that discovery, and another round of device processing followed by my first visit to the testing facilities at the University of New Mexico, we finally had our first clear success: spectrally sensitive detector pixels with a resonance frequency having a direct correspondence to the designed photonic crystal patterns. We celebrated, and I flew home to continue doing modeling. One more processing run followed, on a new optimized detector material grown by the Krishna group to have more quantum dot layers in a stable configuration, and we finally had data that we were satisfied with.

Unfortunately, the simulations proved to be somewhat more difficult. The detector devices, containing both metals and thick waveguide layers, required a very fine simulation mesh, proving a strain on computational power. While I attempted to find methods to extract the numbers we wanted, we also encountered processing difficulties in attempting to fabricate the double-metal detector devices that we predicted would give us better results. In the end, although further progress in this area seemed achievable with a fair amount of additional effort, we decided to focus on finishing up what we already had accomplished.

As that project ended, then, I was freed up to begin something else. At the time, Qiang Lin was intensely busy with the first demonstrations of the double-disk optomechanical resonators, so the obvious thing for me to do was to join him to provide some additional manpower. With the process optimization I had done working on the photonic crystal detectors, I was well-situated to help optimize the double-disk processing, and I started to learn about cavity optomechanics at the same time. The project started out as a crash course in fiber-optic testing for me, since the detector testing I had done had all been free-space-based, but in the end we came out with some very nice results and a world of possibilities to investigate.

The next task we tackled was modifying the double-disk geometry into a very flexible structure that could achieve large static displacements with only a small applied optical force. Developing the “spiderweb” geometry devices – double-ring structures with inner spokes, and rings to stabilize the mechanics – went surprisingly quickly, with few fabrication setbacks, and we were able to begin testing those devices with a minimum of delay. In the end, we had demonstrated a new type of all-optical tunable resonator, with applications to a variety of fields in optical communications, as well as nonlinear and quantum optics.

Emboldened by our successes in both of those endeavors, we returned to complete the work on coherent mechanical mode mixing Qiang had been working on in the original double-disk geometry. With the help of fruitful discussions with Darrick Chang, we completed the theoretical underpin-

nings of the work, and expanded the original idea to encompass the potential for slow-light effects relying on the long phononic timescale rather than the relatively quite short photonic one, as well as the eventual possibility for quantum state transfer between phonons and photons.

Looking into the future, there is still a lot of work to be done: cavity optomechanics remains a wide-open field. I see the possibilities presented by this and all the other innovative work being done in the field, and I can only be excited for what will undoubtedly come next.

This thesis begins by presenting the work on plasmonic photonic crystal mid-infrared photodetectors, beginning with the theory and an experimental demonstration of single-metal waveguide devices, and continuing to expand the theory to discuss double-metal devices. Continuing on, work on dynamic backaction in double-disk resonators is presented, followed by the demonstration of coherent mechanical mode mixing in the same device structure. Finally, the work on the flexible double-ring "spiderweb" optomechanical resonators is discussed, finishing with several appendices on the experimental and mathematical details of the optomechanical work presented in this thesis.

Chapter 1

Plasmonic Resonators for Multispectral Mid-Infrared Detectors

1.1 Introduction

Optical sensors in the mid-infrared wavelength range are extremely important in a wide variety of areas, such as night vision, missile guidance, and biological spectroscopy [1]. Currently, the best mid-infrared detectors are based on mercury-cadmium-telluride (MCT). MCT detectors are very efficient, but large-area focal-plane arrays are difficult and expensive to grow due to difficulties with the epitaxial growth of mercury-based compounds [2, 3]. More recently, other detector materials have become more common, but they have various limitations in the required direction of incoming light, such as in quantum well detectors, or in detector efficiency, as in quantum dot or dots-in-a-well (DWELL) detectors [4, 5]. With the use of a resonant cavity, it becomes possible to increase the detector efficiency many times over by greatly extending the interaction length between the incoming light and the active material. Instead of incoming light making only one pass through the active region, in a resonant detector the light can make hundreds of passes.

The presence of a resonator can also make each pixel frequency and polarization specific [6–8], allowing for a hyperspectral and hyperpolarization sensor without the need for any external grating or prism. There are many applications for frequency and polarization-sensitive detectors. A hyperspectral detector array could function as a spectrometer on a chip, filtering incoming signals through the use of hundreds of highly sensitive detector pixels. A hyperpolarization detector could be used in a camera to provide an additional layer of information which can be combined with frequency and intensity data to better distinguish between different objects in an image.

The current dominant technologies in the field of multispectral imaging rely on the use of either

a broadband focal plane array (FPA) with a spinning filter wheel in front of it [9], or a bank of FPAs with a dispersive element such as a grating or prism to separate light of different frequencies. These methods are limited by the often high cost and complexity of such systems. However, when spectral sensitivity is encoded at the pixel level within a single focal plane array, multi-spectral detection becomes much more practical for use in a wide range of applications. In addition, the use of pixel-integrated resonators to provide spectral sensitivity can dramatically increase the efficiency of the detector due to the many passes light makes within the resonator.

The resonator system we investigate here is composed of a photonic crystal cavity for in-plane confinement, and a plasmonic waveguide [10, 11], composed of either a single or a double-layer of metal, for the vertical confinement. This resonator design, combining the benefits of a plasmonic waveguide and a photonic crystal cavity, has a number of advantages. The plasmonic waveguide serves multiple purposes: it serves as a superior top contact (or in the double-metal case, top and bottom contact) for the detector device providing enhanced extraction efficiency; it provides strong vertical confinement (nearly total confinement, for the double-metal structure) of the resonator mode within the active region; and it increases the index contrast in the photonic crystal, enhancing the in-plane confinement of the resonator mode and enabling strong confinement even with a very shallow photonic crystal etch extending only through the top metal layer [12, 13]. The photonic crystal patterning also serves a dual purpose: it provides in-plane confinement to the resonator mode, serves as a grating coupler to couple normal-incidence light into the in-plane direction of the detector, and provides a mechanism for freely adjusting the polarization response of the detector pixel.

In the past, many promising schemes have been proposed and/or demonstrated illustrating various aspects of these concepts: optical resonators to provide spectral [14] or spectral and polarization filtering [15–17], enhanced confinement of light to increase material absorption [14, 16–18], and metallic gratings to enable strong confinement without the necessity for deep etching [15, 17, 18]. We have also demonstrated plasmonic photonic crystal designs with the maximum field intensity at the top metal interface to allow for thinner devices and increase field overlap with the active region versus metallic Fabry Perot-based structures, in both deep-etched [19] and shallow-etched [13] single-metal-layer implementations. Here we detail the design and experimental demonstration of the shallow-etch single-metal resonators, and expand those design principles to propose a highly-efficient shallow-etch double-metal cavity design for hyperspectral and hyperpolarization, strongly enhanced mid-infrared detection. Both single-metal and double-metal designs are detector material agnostic, are easily incorporated into current FPA processing techniques, and do not involve the

damage or removal of any detector active region material, providing significantly increased flexibility and functionality with a minimal increase in complexity. This work was originally presented in Refs. [13, 20].

1.2 Photonic Crystal Design

A significant obstacle to using resonant cavities to enhance detector absorption and provide spectral and polarization sensitivity is achieving sufficient input coupling from free-space light. Commonly such resonators, with their high confinement, have only very poor phase-matching to a normal incidence free-space beam such as that which we would ideally like to detect for imaging applications. However, with suitable design and optimization of the plasmonic photonic crystal structure, it becomes possible to achieve significant free-space coupling, and indeed, even move towards achieving critical coupling (as will be discussed in Section 1.6).

We used group theory to design a frequency and polarization sensitive photonic crystal structure suitable for coupling efficiently to normal incidence light. The simplest polarization-sensitive resonator design would be a one-dimensional grating. However, it is beneficial to choose a fully-connected photonic crystal design in order to take full advantage of the increased current extraction efficiency from the plasmonic metal layer serving as the top contact of the detector device, as well as allowing for continuous variation between polarization-sensitive and polarization-insensitive devices. Therefore, we analyze a square-lattice structure here, and describe how stretching the lattice in one direction can split the degenerate modes of the structure and create a strong polarization sensitivity for use in imaging applications.

The bandstructure of a square lattice photonic crystal is shown in Fig. 1.1(a), calculated using plane wave expansion. The ratio of circular hole radius r to lattice spacing a used was $r/a = 0.32$, and the index of the material was taken to be the effective index of the double metal plasmon waveguide, $n_{\text{eff}} = 3.24$. Details of the plasmon effective index calculation are discussed in Section 1.5. There are no band gaps for this structure, however there are several flat-band regions. The group velocity of these band-edge modes is close to zero, therefore the light travels very slowly and is effectively confined within the patterned region. Band-edge modes are ideal for applications such as detectors, as the mode volume is large, allowing more of the active region to be contained within the resonator. There are a number of flat-band regions within the bandstructure in Fig. 1.1(a), but we are interested in the modes at the Γ-point. The Γ-point corresponds to normal-incidence modulo

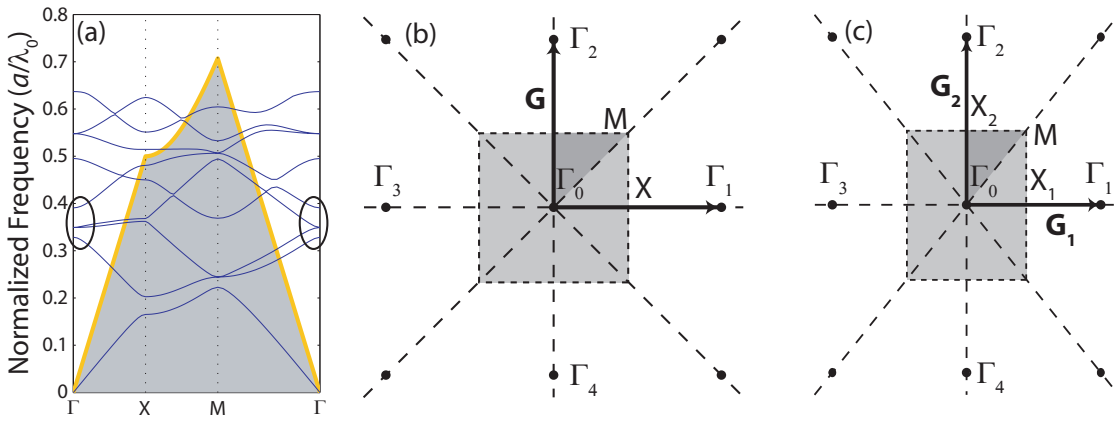

Figure 1.1: (a) In-plane guided mode TM-like bandstructure plot of a square-lattice photonic crystal ($n_{\text{eff}} = 3.24$) with $r/a = 0.32$. The light line is shown in yellow, and the modes of interest are circled. (b) Reciprocal lattice for an unstretched photonic crystal. (c) Reciprocal lattice for a stretched photonic crystal.

a reciprocal lattice vector, so the Γ-point modes are capable of coupling normal-incidence light into the in-plane direction of the detector. In addition, the Γ-point modes are above the light line, and therefore leak into the air, enabling them to couple more easily to an input free space beam. We investigated the four lowest-order Γ-point modes, circled in Fig. 1.1(a), using group theory [21, 22].

The point group symmetry of the square photonic crystal lattice, with reciprocal lattice shown in Fig. 1.1(b), is C_{4v}. The in-plane field of the unperturbed waveguide is given by $\mathbf{E}_{\mathbf{k}}(\mathbf{r}) = \hat{z}e^{-(\mathbf{k})\cdot\mathbf{r}}$, with $\mathbf{k}$ and $\mathbf{r}$ representing the in-plane wavenumber and spatial position, respectively. When the structure is patterned, coupling will occur between waveguide modes with similar unperturbed frequencies, and propagation constants that differ by a reciprocal lattice vector $\mathbf{G}$.

There is one Γ-point within the first Brillouin zone (IBZ), at $(0,0)k_\Gamma$, with $k_\Gamma = 2\pi/a$. Since we are interested in modes with nonzero k-vectors in the in-plane direction, we will consider the nearest Γ-points in the surrounding Brillouin zones, at $(\pm(1,0)k_\Gamma, \pm(0,1)k_\Gamma)$. These points are labeled in Fig. 1.1(b). The group of the wave vector, the symmetry group of a plane wave modulo $\mathbf{G}$, is C_{4v} at the Γ-point. The character table of C_{4v} is shown in Table 1.1.

The star of $\mathbf{k}$ ($\star\mathbf{k}$) at the Γ-point is the set of independent Γ-points within the region. In this case, $\star\mathbf{k}$ is given, not uniquely, by $\mathbf{k}_{\Gamma_1}$. This will be our seed vector. We find the symmetry basis for the modes at that satellite point by applying the symmetry operations of the group of the wave vector to the seed vector. In this case, the basis is $(\mathbf{E}_{\mathbf{G}_1}, \mathbf{E}_{-\mathbf{G}_1}, \mathbf{E}_{\mathbf{G}_2}, \mathbf{E}_{-\mathbf{G}_2})$. Projecting this symmetry

Table 1.1: Point Group character tables for the square and rectangular lattice.

C_{4v}	E	C_2	$2C_4$	$2\sigma_v$	$2\sigma_d$	C_{2v}	E	C_2	σ_x	σ_y
A_1	1	1	1	1	1	A_1	1	1	1	1
A_2	1	1	1	- 1	-1	A_2	1	1	-1	-1
B_1	1	1	-1	1	-1	B_1	1	-1	-1	1
B_2	1	1	-1	-1	1	B_2	1	-1	1	-1
E	2	-1	0	0	0					

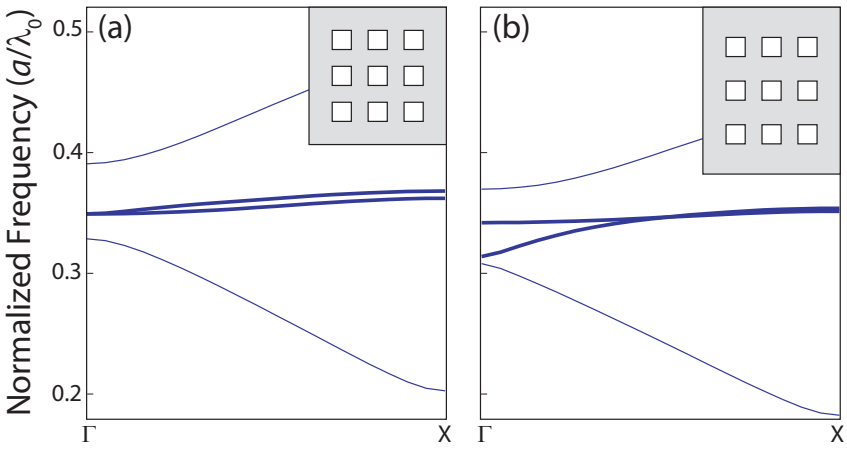

Figure 1.2: 2D bandstructure plots near the gamma point of (a) a square lattice and (b) a rectangular lattice, stretched by 10%. The dipole-like modes are shown in bold.

basis onto the irreducible representation (IRREP) spaces of C_{4v}, we find the modes:

$$\begin{aligned}
\mathbf{E}_{A_1} &= \hat{z}(\cos(\mathbf{k}_{\mathbf{G}_1}\cdot\mathbf{r}) + \cos(\mathbf{k}_{\mathbf{G}_2}\cdot\mathbf{r})),\\
\mathbf{E}_{B_1} &= \hat{z}(\cos(\mathbf{k}_{\mathbf{G}_1}\cdot\mathbf{r}) - \cos(\mathbf{k}_{\mathbf{G}_2}\cdot\mathbf{r})),\\
\mathbf{E}_{E,1} &= \hat{z}(\sin(\mathbf{k}_{\mathbf{G}_2}\cdot\mathbf{r})),\\
\mathbf{E}_{E,2} &= \hat{z}(\sin(\mathbf{k}_{\mathbf{G}_1}\cdot\mathbf{r})),
\end{aligned} \tag{1.1}$$

where A_1, B_1, and E are IRREP spaces of C_{4v} (see Table 1.1), and $\mathbf{r}$ has its origin at the center of the air hole. Considering that modes with more electric field concentrated in areas with high dielectric constant tend to have lower frequency than those with electric field concentrated in low dielectric regions [23], we can order the modes by frequency. E is a two dimensional IRREP, so generates two degenerate modes. We associate this pair of modes $\mathbf{E}_{E,1}, \mathbf{E}_{E,2}$ with the second and third frequency bands, which is in agreement with the bandstructure in Fig. 1.1(a). These degenerate modes, with dipole-like symmetry and the spatial pattern given in Eqs. 1.1, radiate with a far-field pattern which is uniform: in the case of a finite structure, a Gaussian-like far-field without anti-nodes.

In order to achieve polarization sensitivity, we need to split these two degenerate dipole-like modes. To do this, we stretch the photonic crystal lattice (not the photonic crystal holes) in one direction, giving the reciprocal lattice shown in Fig. 1.1(c). The effect of stretching the lattice on the four lowest-order Γ-point modes is shown in Fig. 1.2. The symmetry group of this perturbation is C_{2v}; the character table for C_{2v} is shown in Table 1.1. Using the compatibility relations between C_{4v} and C_{2v}, we find the new set of modes:

$$\begin{aligned}
\mathbf{E}_{A_1,1} &= \hat{z}(\cos(\mathbf{k}_{\mathbf{G}_1}\cdot\mathbf{r}) + \cos(\mathbf{k}_{\mathbf{G}_2}\cdot\mathbf{r})),\\
\mathbf{E}_{A_1,2} &= \hat{z}(\cos(\mathbf{k}_{\mathbf{G}_1}\cdot\mathbf{r}) - \cos(\mathbf{k}_{\mathbf{G}_2}\cdot\mathbf{r})),\\
\mathbf{E}_{B_1} &= \hat{z}(\sin(\mathbf{k}_{\mathbf{G}_2}\cdot\mathbf{r})),\\
\mathbf{E}_{B_2} &= \hat{z}(\sin(\mathbf{k}_{\mathbf{G}_1}\cdot\mathbf{r})).
\end{aligned} \tag{1.2}$$

These modes are plotted in Fig. 1.10. The C_{4v} two-dimensional representation E decomposes into $B_1 \oplus B_2$ under C_{2v}, therefore the dipole-like modes are no longer degenerate. This is in agreement with what we see in the bandstructure of the stretched lattice, Fig. 1.2(b).

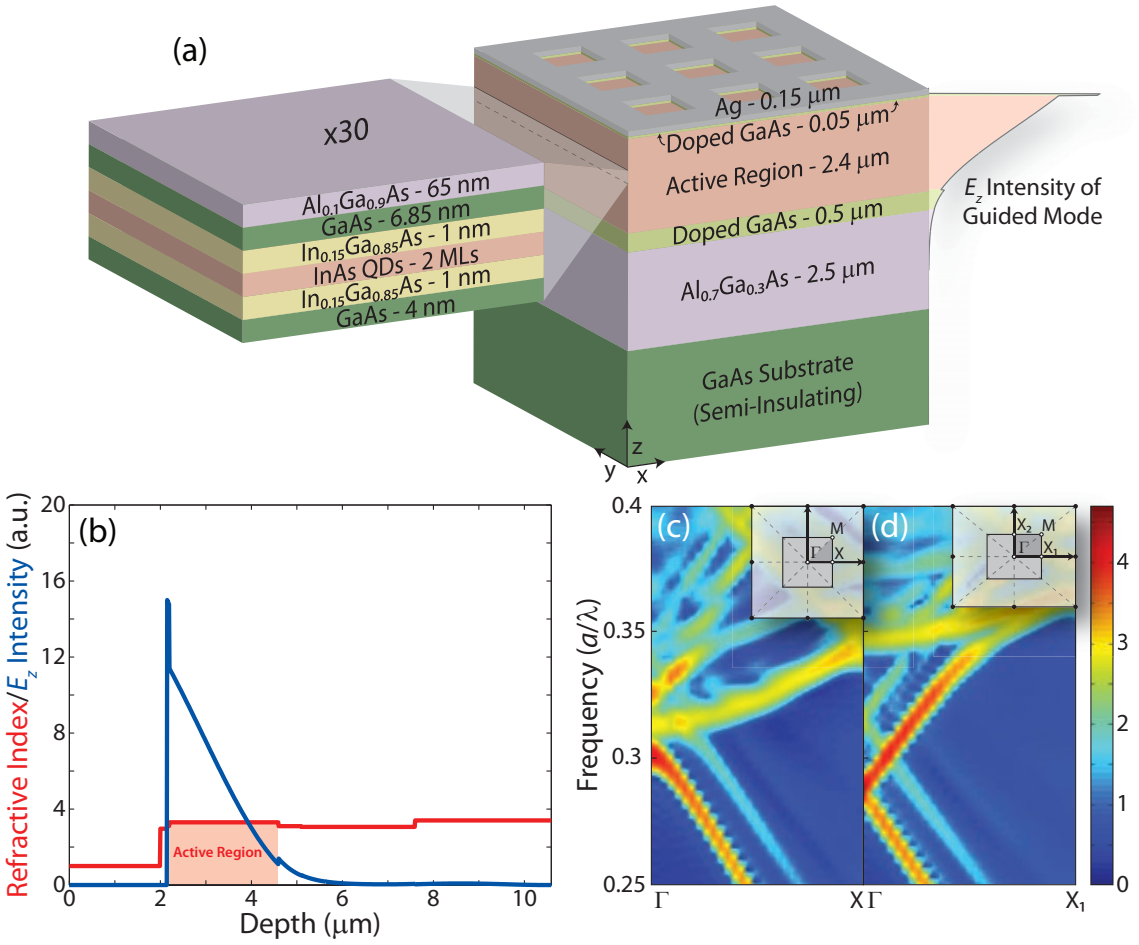

Figure 1.3: (a) A crossectional image of several lattice constants of the single-metal DWELL detector design. (b) E_z intensity profile of the fundamental plasmon waveguide mode (blue) and the real part of the refractive index of the layers (red), with the detector active region highlighted. (c) FDTD bandstructure for the unstretched single-metal photonic crystal structure shown in (a) in the region between the Γ and X points. (d) FDTD bandstructure between the Γ and X_1 points for a single-metal photonic crystal structure stretched and compressed by 10% in the x and y directions, respectively.

1.3 Single-Metal Plasmon Resonator Design

In addition to the in-plane confinement provided by the photonic crystal pattern discussed in Section 1.2, it is necessary to confine the light in the vertical direction as well. We begin with a single-metal design suitable for straightforward fabrication (as experimentally demonstrated in [13]), and then expand the discussion to consider a double-metal design that mimics the top and bottom contact layers in detector focal plane arrays for easy integration. As we operate in the mid-infrared frequency range, we are far from the plasmon resonance frequency of metals, typically in the ultraviolet; operating in this regime avoids the very high metal losses that occur at frequencies closer to the plasmon frequency, and allows the mode to extend farther into the active region of the detector.

The single-metal resonant cavity consists of a single layer of metal with etched square holes in a square lattice periodic array. A representation of several lattice constants of the device structure is shown in Fig. 1.3(a). The plasmonic layer provides the vertical confinement, confining the optical mode with a maximum at the surface of the metal (Fig. 1.4(b,c)), while the etched air-holes create a PC pattern to confine the light in-plane. Combined together, this resonator design provides full 3D confinement, significantly increasing the amount of time light spends within the detector active region, and therefore enhancing the probability of detection. Due to the strong index contrast between the surface plasmon [10, 11, 24] mode beneath the metal regions and the dielectric-confined mode beneath the air holes, this plasmonic PC grating is strong enough to generate an in-plane confined resonant mode without etching into the detector active material [12, 25], allowing a resonator to be fabricated without damaging or removing active material. The numerical and symmetry analysis presented in Sec. 1.2 and Ref. 20 shows that the two degenerate dipole-like in-plane modes of the structure (Fig. 1.4(b-d)) couple most easily from free space. Further improvements in the free-space coupling efficiency were performed by optimizing the top metal thickness and hole size. In addition, as the two dipole-like modes couple to orthogonal polarizations of incoming light, a stretch of the PC lattice breaks the degeneracy of the two modes, splitting their resonance frequencies and thus achieving high polarization selectivity [6, 16].

The single-metal resonant DWELL detector structure we study is shown in Fig. 1.3(a), along with the 1D E_z intensity profile of the fundamental plasmon waveguide mode in Fig. 1.3(b) (not including the effects of the photonic crystal holes). The vertical confinement factor of this mode within the active region of the detector is $\eta = 91\%$, in strong contrast to the generally much lower confinement factor of purely dielectric waveguides. This extremely high confinement, even for a

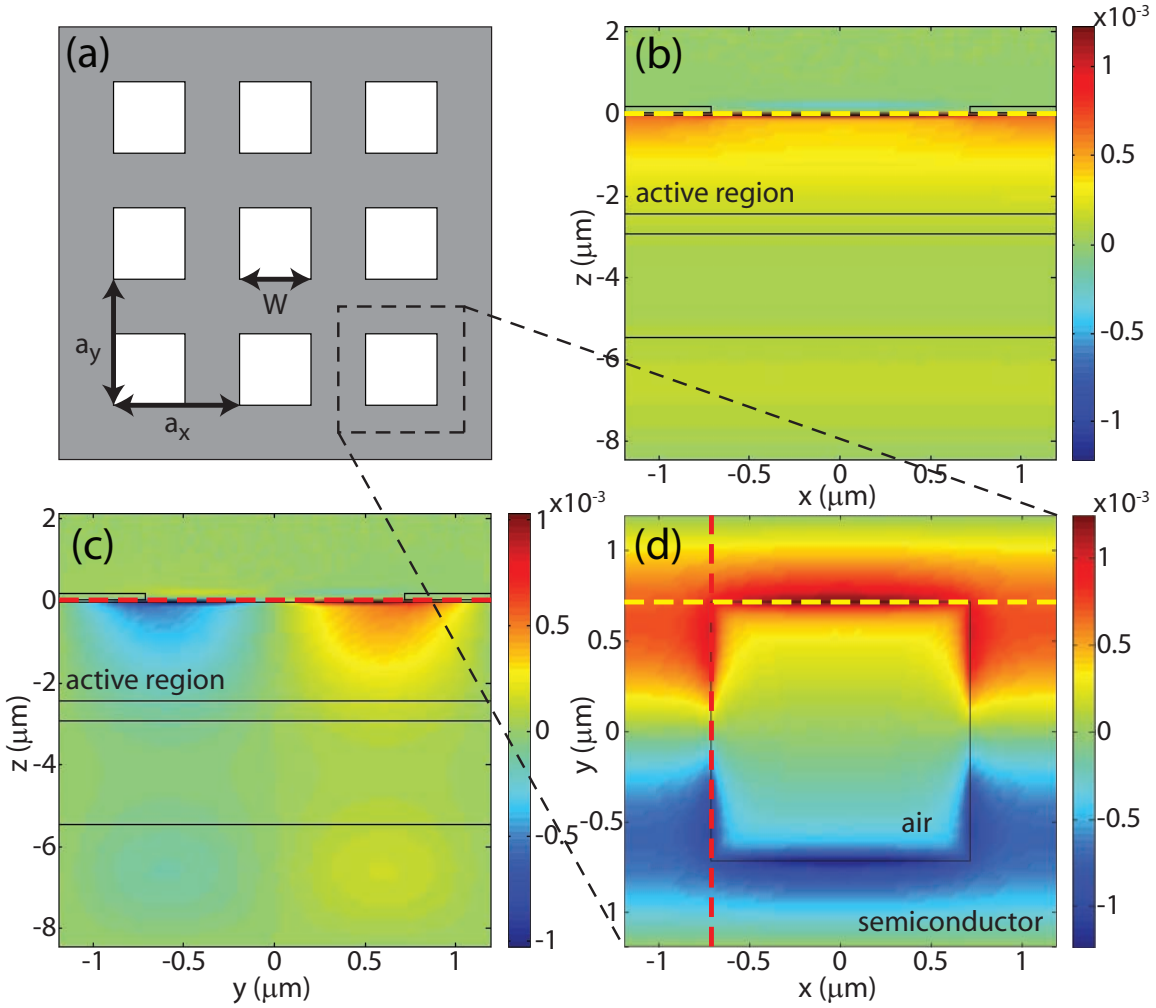

Figure 1.4: (a) A diagram of the unstretched PC structure showing relevant dimensions. The expanded plots show the E_z mode profile for one lattice constant of one of the two dipole modes for an unstretched PC lattice in (b) the x-z plane along the hole edge, (c) the y-z plane along the hole edge, and (d) the x-y plane just beneath the metal-semiconductor interface, for a structure with lattice constant $a = 2.38$ μm, $\bar{W} = 0.6$, and metal thickness $t = 150$ nm.

waveguide utilizing only a single layer of metal, immediately showcases the benefits of choosing a plasmon-based photonic crystal design.

Figure 1.4(a) shows relevant dimensions of the structure; we define the normalized hole width as $\bar{W} = 2W/(a_x + a_y)$. Field profiles along different planes for the square lattice dipole-like mode are plotted in Fig. 1.4(b-d) over a single unit cell; the other dipole mode has the same field pattern, rotated by 90 degrees in the x-y plane. The simulated active region absorption corresponding to this mode is 10.9%, given an approximate 2% single-pass absorption in the DWELL material, and corresponds to an expected resonant responsivity enhancement of 5-6 times that of a control sample with no plasmonic layer or PC patterning.

The TM square lattice single-metal plasmonic photonic crystal bandstructure for the region near the Γ-point is shown in Fig. 1.3(c), calculated using finite difference time domain (FDTD) methods with metal material properties from Ref. 26. The simulated structure has a lattice constant of $a = 2.939$ μm, a hole width W vs. lattice constant ratio of $\bar{W} = 0.567$, and a metal thickness of $t_m = 150$ nm, and shows Γ-point modes which are in good agreement with the group theory predictions in the previous section. Figure 1.3(d) shows the same bandstructure region for a lattice stretched and compressed by 10% along the $\hat{x}$- and $\hat{y}$- axes respectively, with the two dipole modes showing a significant frequency splitting, also as predicted. These two 3D FDTD simulations match up well with the 2D plane-wave expansion bandstructure predictions shown in Fig. 1.2, with the addition of visible higher-order vertical modes from the single-metal plasmon waveguide. The double-metal waveguide structure can be designed such that these higher-order vertical modes are eliminated.

The overall quality factor of the two degenerate dipole modes in the unstretched-lattice case (for resonator parameters given in the caption to Fig. 1.5) is calculated to be $Q_{\text{per}} = 48$ for a perfectly periodic structure, not including the in-plane quality factor, Q_{xy}, which can be increased indefinitely by adding more lattice constants to the resonator structure. By simulating the structure as excited by an incoming, normal incidence plane wave, we can measure the percentage of the incoming light absorbed within the active region. The simulated DWELL active region absorption corresponding to this mode is $A_t = 11.5\%$ (Fig. 1.5(a)), with material parameters specified so as to reproduce the approximate DWELL material single-pass absorption, $A_{\text{DWELL}} = 2\%$. This corresponds to an expected responsivity enhancement factor of $E \equiv A_t/A_{\text{DWELL}} = 5.75$ at the resonant wavelength, versus a sample with no top patterned plasmonic metal layer at the same wavelength (Fig. 1.5). Note that this enhancement factor is not normalized to the area of the holes in the plasmonic metal,

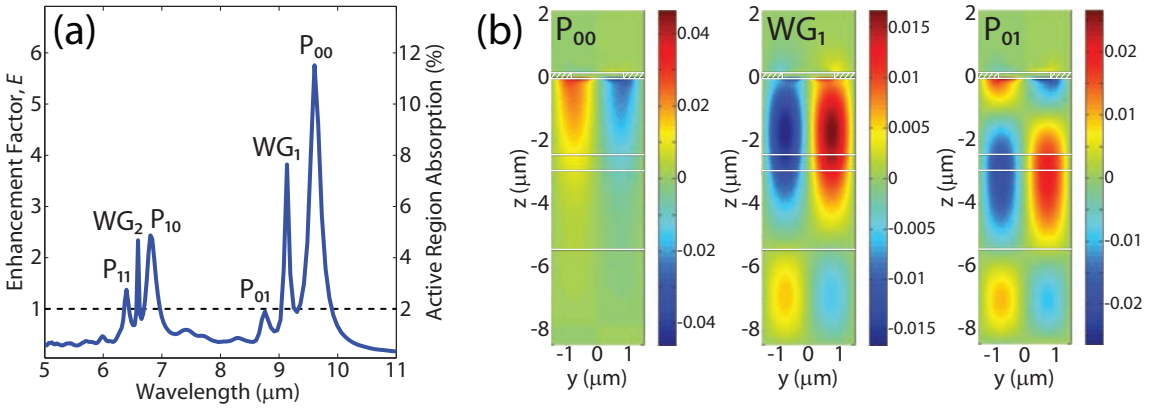

Figure 1.5: (a) FDTD simulated enhancement factor and active region absorption vs. wavelength, based on a 2% single-pass absorption, using a structure with lattice constant $a = 2.939$ μm, $\bar{W} = 0.567$, and metal thickness $t_m = 150$ nm. (b) E_z mode profiles in the y-z plane at the hole edge for the three longer-wavelength peaks in (a), for one lattice constant. The three shorter-wavelength peaks have similar vertical field profiles, but are higher-order in the x-y plane.

as is typically done in the case of 'extraordinary' transmission through thin metal layers [24]; the absorption values are compared over the same physical region of detector material.

The simulated active region absorption, A_t, and enhancement factor, E, are plotted versus frequency in Fig. 1.5(a), showing the fundamental plasmon mode at 9.6 μm and a series of higher-order modes at shorter wavelengths. The mode P_{xy} corresponds to the x^{th}-order in-plane and y^{th}-order vertical plasmon waveguide mode. Thus P_{00} corresponds to the fundamental plasmon mode as discussed above. WG_1 and WG_2 are the first and second-order TM waveguide modes of the structure, and Fig. 1.5(b) shows that they have a lower overlap with the metal surface than the plasmon modes. Thus their Q_{per} is higher than the plasmon modes for the perfectly periodic structure simulated, as can be seen in Fig. 1.5(a), but their in-plane Q-factor, Q_{xy}, will be very small due to their minimal interaction with the photonic crystal grating. As the overall absorption enhancement factor is lower for these modes even in the infinite-structure limit, we conclude that the response of this resonator structure will be dominated by the surface plasmon-guided modes.

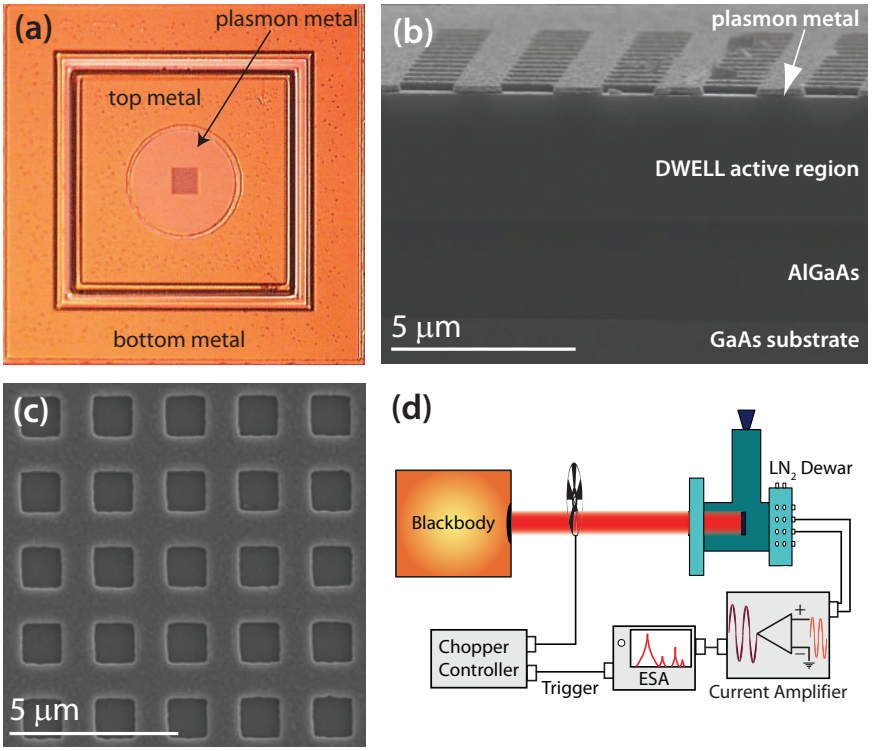

Figure 1.6: (a) Optical image of the fabricated device indicating the top, bottom and plasmon metallizations. (b) Cross-sectional SEM of the fabricated square-lattice device indicating the plasmon metal and device layers. (c) SEM image of the fabricated square-lattice PC pattern on the plasmon metallization. (d) Schematic of the setup used for measuring responsivity and detectivity of the fabricated devices. Responsivity measurements were performed by illuminating the sample with a calibrated Mikron M365 blackbody at $T = 800$ K. The blackbody radiation was modulated at a frequency of 400 Hz using a chopper and this signal was used as a trigger for the SRS 760 fast Fourier transform (FFT) spectrum analyzer. The photocurrent was amplified using a SRS 570 low noise amplifier and then measured in the spectrum analyzer.

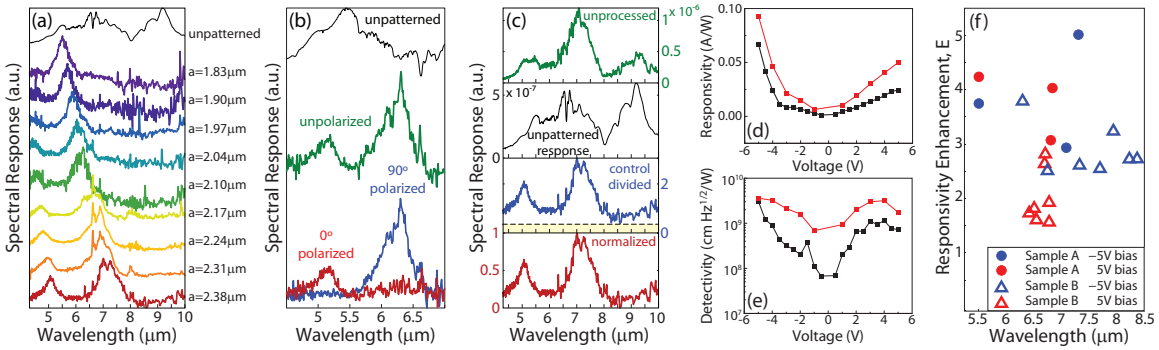

Figure 1.7: (a) Normalized spectral response from square lattice devices at a bias of 5 V, indicating tuning of peak wavelength with the lattice constant. (b) Normalized spectral response from a rectangular lattice device ($a_x = 1.65$ μm, $a_y = 2.02$ μm) at a bias of -5 V. The response to unpolarized light is shown in green, and beneath is the response to light polarized at 0 degrees (red) and 90 degrees (blue) relative to the shorter lattice constant dimension of the lattice. (c) Data processing of the $a = 2.38$ μm device response. The unprocessed data (green) is divided by the unpatterned DWELL response to show the resonances independently of the base detector response. The background scattering from other regions of the sample (yellow) is then subtracted from the control divided data (blue) and normalized, to give the final spectral response (red) that is plotted in Fig. 1.7(a,b). (d) Measured responsivity and (e) detectivity of a stretched lattice device with $a_x = 1.78$ μm and $a_y = 2.16$ μm (red), and a control device (black). (f) Measured peak responsivity enhancement E versus resonant device wavelength for two samples at positive and negative bias.

1.4 Single-Metal Experimental Demonstration

To test these predictions, we fabricated two detector samples: sample A with a square lattice PC, and sample B with a rectangular lattice PC having a lattice constant stretching ratio $a_y/a_x = 1.2$. Figure 1.6(a-c) shows representative images of the fabricated devices. All of the PC patterns had the same normalized hole width ($\bar{W} \sim 0.6$), but different lattice constant values, and therefore different resonant wavelengths determined by the scaling of the pattern. The spectral response of the surface-plasmon resonant detectors was measured at 30 K using a Nicolet 870 Fourier transform infrared spectrometer (FTIR) with the patterned detector sample used in place of the standard FTIR detector. Responsivity and detectivity measurements were performed at 77 K using the experimental setup shown in Fig. 1.6(d). To separate out the background scattering and the frequency response of the DWELL material from the resonant enhancement, we perform data processing as shown for a typical spectral response measurement in Fig. 1.7(c).

As predicted, by varying the lattice constant and symmetry of the patterned grating, we are able to tailor the wavelength and polarization response of each detector pixel. Figure 1.7(a) shows the resonant spectral response from a set of representative detector pixels on sample A, varying

the peak wavelength response from 5.5 μm to 7.2 μm by choosing PC lattice constants in a range from 1.83 μm to 2.38 μm. The linewidth of these resonances is ~ 0.9 μm, providing strong spectral sensitivity within the broad background DWELL response which covers more than 5 μm. In addition to the fundamental surface plasmon resonant mode, we also observe a higher-order plasmon mode as predicted by the FDTD simulations in Fig. 1.4(b), at a wavelength in good agreement with the theory. In order to generate a polarization-sensitive response, we stretch the lattice constant in one direction (sample *B*), splitting the resonant detector response into two well-separated peaks as shown in the green curve of Fig. 1.7(b). By varying the polarization of the light incident on the detector, we show that these two peaks correspond to orthogonal linear polarization directions of incoming light, as represented by the blue and red curves of Fig. 1.7(b). The high polarization extinction between the two curves indicates clearly the strong polarization dependence in our device. The experimentally measured spectral peaks are broadened relative to the FDTD simulated values in Fig. 1.4(b) due to the finite extent of the PC pattern ($\sim$50 μm in diameter), and therefore the limited in-plane confinement.

To characterize the efficiency of the detector response and the resonant enhancement, we define and measure the responsivity and detectivity of samples *A* and *B* as follows. The peak responsivity was computed using the expression

$$R_p = \frac{I_0}{\int_{\lambda_1}^{\lambda_2} R_N(\lambda) L_e(\lambda, T) A_s A_d \frac{t F_F}{r^2} d\lambda} \tag{1.3}$$

where $R_N(\lambda)$, I_0, L_e, T, A_s, and A_d are the normalized spectral response, measured photocurrent, the black body spectral excitance, the black body source temperature, the area of the source, and the area of the detector, and r, t, F_F are the distance between the source and the detector, the transmission of the window and geometrical form factor, respectively. The lower and upper wavelength bounds of the detector response are given by λ_1 and λ_2. The detectivity D^* is then

$$D^* = \frac{\sqrt{A_d \Delta f}}{i_n} R_p \tag{1.4}$$

where A_d is the detector area, Δf is the noise equivalent bandwidth ofour measurement, and i_n is the noise current.

Compared to a control (unpatterned) sample, the plasmonic PC patterned devices provide a strong enhancement of responsivity and a corresponding increase in detectivity across an applied

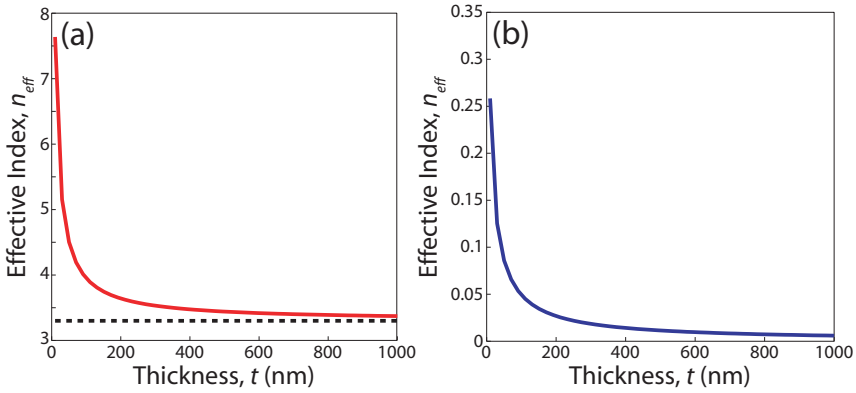

Figure 1.8: The (a) real (red) and (b) imaginary (blue) parts of the dielectric constant dispersion relation of an Ag/GaAs/Ag waveguide vs. waveguide thickness t, for a free-space wavelength of $\lambda = 10\ \mu$m. The GaAs core index is indicated by a dotted black line.

bias range from -5 V to 5 V, as shown in Fig. 1.7(d) and (e). The enhancement factor E is defined as $E = R(\lambda_i)/R_c(\lambda_i)$, where $R(\lambda_i)$ is the responsivity of the patterned detector at the resonant wavelength and $R_c(\lambda_i)$ is the responsivity of the control sample at the same wavelength. In Fig. 1.7(f), we show enhancement factors across a range of wavelengths reaching as high as 5X for sample A, and 4X for sample B.

1.5 Double-Metal Plasmon Resonator Design

Though we have shown, theoretically and experimentally, that a single-metal plasmonic device can have high active-region confinement and reasonable Q-factors, we can move to a double-metal design to increase both of these quantities even further. The double-metal structure brackets the active region with a thin layer of plasmonic metal on either side, and the photonic crystal holes are etched only into the top metal layer, as before. All of the advantages of the single-metal device are preserved, while the substrate loss can be essentially eliminated and the detector active region vertical confinement can approach 100%. These are achieved at the price of higher plasmonic metal loss, but in the mid-infrared region, this loss is not prohibitive.

In choosing the ideal waveguide thickness, t, for the double-metal (or metal-insulator-metal, MIM) plasmonic waveguide, there are several considerations. Figure 1.8 shows the variation of mode effective index n_{eff} with waveguide thickness for a Ag/GaAs/Ag waveguide at a free-space wavelength of $\lambda = 10\ \mu$m. As the waveguide thickness decreases and more energy moves into the metal regions, both the real (Fig. 1.8(a)) and the imaginary (Fig. 1.8(b)) parts of the effective index

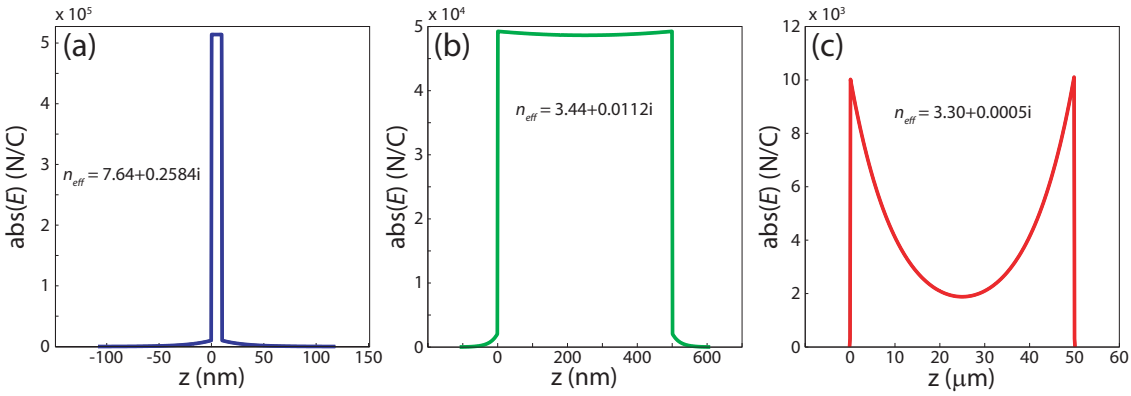

Figure 1.9: The field profile for Ag/GaAs/Ag plasmon waveguides with a thickness t of (a) 10 nm, (b) 500 nm, and (c) 50 μm are shown, for a free-space wavelength of $\lambda = 10\,\mu$m. The effective index n_{eff} for each plasmon waveguide is also given.

increase. A high real part of the effective index is beneficial, because it increases the index contrast of the photonic crystal by increasing the contrast between the photonic crystal holes and the metal-covered regions (the double-metal waveguide). A higher index contrast increases the strength of the photonic crystal perturbation, improving the in-plane confinement Q_{xy} of the resonator. If the index contrast is high enough, the photonic crystal holes can be etched only into the top metal, without removing material from the detector active region. In the double-metal case, this condition is even easier to achieve than in the single-metal case. However, the imaginary part of the effective index is proportional to the loss in the waveguide, and must be minimized. Therefore a waveguide width must be chosen to balance the competing factors of index contrast and loss.

The field profiles of three Ag/GaAs/Ag plasmon waveguides are shown in Fig. 1.9, with the calculated effective index n_{eff}, for a free-space wavelength of $\lambda = 10\,\mu$m. Though the effective index values shown here would seem to generate only a low index contrast with the core dielectric material ($n_{GaAs} = 3.3$) for reasonable waveguide thicknesses, it must be considered that these simulations do not take into account the effect of the photonic crystal holes etched in the metal. In fact, it can be shown [12, 25] that the presence of holes in a metal layer has the effect of lowering the effective plasmon frequency of that layer without significantly raising losses, increasing the real but not the imaginary part of the waveguide effective index. Thus, the actual combined photonic crystal and plasmon structure will have a considerably higher index contrast than would be expected from these effective index values. This is demonstrated via simulations of the full 3D structure which show that, even with the photonic crystal holes etched only into the top metal layer, we still achieve significant

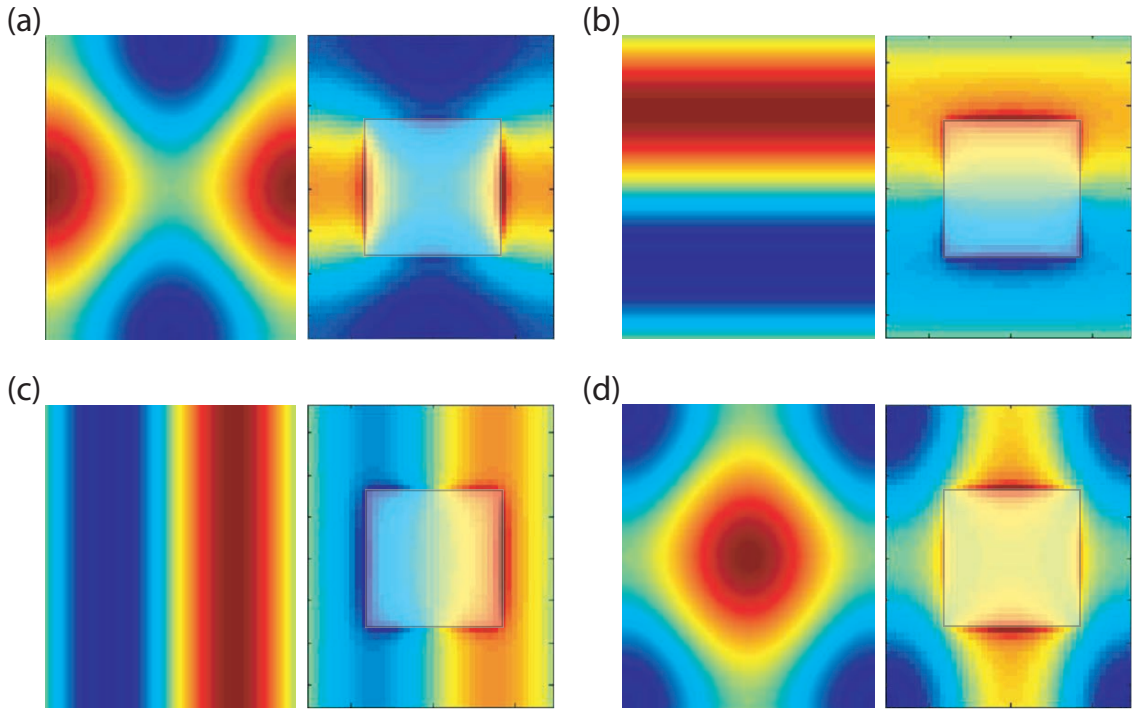

Figure 1.10: A comparison of the FDTD simulated and group theory predicted E_z field profiles for the four lowest gamma-point modes of a 20% stretched lattice, in order of increasing frequency. The modes, labeled according to C_{2v} designations, are (a) $A_{1,1}$, (b) B_2, (c) B_1, (d) $A_{1,2}$. The group theory predictions are shown on the left, while the FDTD results, including the effects of the photonic crystal air hole (overlaid white square), are shown on the right. The FDTD fields shown are 2D slices of the full simulations taken just below the top metal layer, inside the active region.

in-plane confinement and vertical coupling.

Full structure simulations (photonic crystal plus plasmon waveguide) were performed using the FDTD method on a perfectly periodic lattice (as before, due to computational constraints), with a lattice stretched by 20%. These FDTD simulations confirm the results of our separate photonic crystal and plasmon waveguide simulations. Figure 1.10 shows the FDTD field plots (left) in comparison with the group theory mode plots (right). Though the presence of the air-hole distorts the shape of the modes in the center of the FDTD images, at the outside of the simulation region it can be seen that the simple group theory calculations have accurately predicted the mode shapes given by the more complex FDTD simulations.

We have also investigated the far-field profiles of the four Γ-point modes, through examining the spatial fourier transform of E_z. Due to time-reversal symmetry, the field profile of a mode that can be coupled into the resonator is equivalent to the field profile of the resonator mode propagated

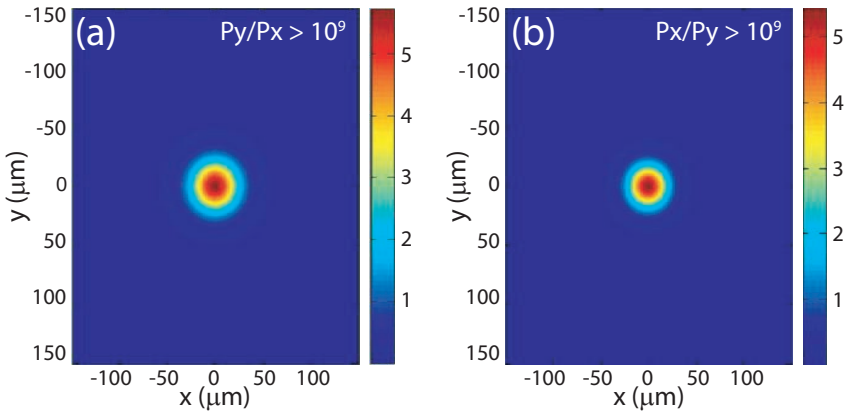

Figure 1.11: Far-field plots at $z = 90\ \mu$m of the two Γ-point dipole modes in a stretched-lattice structure with $\bar{W} = 0.5309$ and $a_y/a_x = 1.2$. (a) B_2 mode power density, with dominant $\hat{y}$-polarization. (b) B_1 mode power density, with dominant $\hat{x}$-polarization. For both B_1 and B_2 modes, the polarization selectivity is calculated to be greater than 10^9, limited entirely by error in the numerical simulation.

out into the far-field, therefore these far-field plots indicate the mode-shapes and polarizations that couple most strongly from free space to the resonator mode. Far-field plots of the two fundamental stretched-lattice dipole modes, B_1 and B_2, are shown in Fig. 1.11, generated from an 10X10 tiled array of the FDTD simulated field profile (itself one lattice constant in size) and apodized using a Gaussian function with a standard deviation of two lattice constants (a_x and a_y, respectively) in the x and y directions. We can see from Fig. 1.11(a,b) that the B_1 and B_2 modes are well-suited for coupling to incident free-space light, since the far-field profile has a single lobe at normal incidence and does not contain any anti-nodes, in agreement with the group theory predictions from Section 1.2.

1.6 Critical Coupling

After optimizing the large-scale resonator design and choosing photonic crystal modes which have the largest coupling to normal-incident light, it still remains to find the best values for the design parameters to increase detector absorption, and to determine the fundamental limits on absorption enhancement for these two (single-metal and double-metal) resonator designs. We find that, for the double-metal resonator, the absorption is greatest at the point of critical input coupling, whereas we find a different optimal point for the single-metal resonator, as the parasitic substrate loss increases along with the detector absorption as the input coupling is increased.

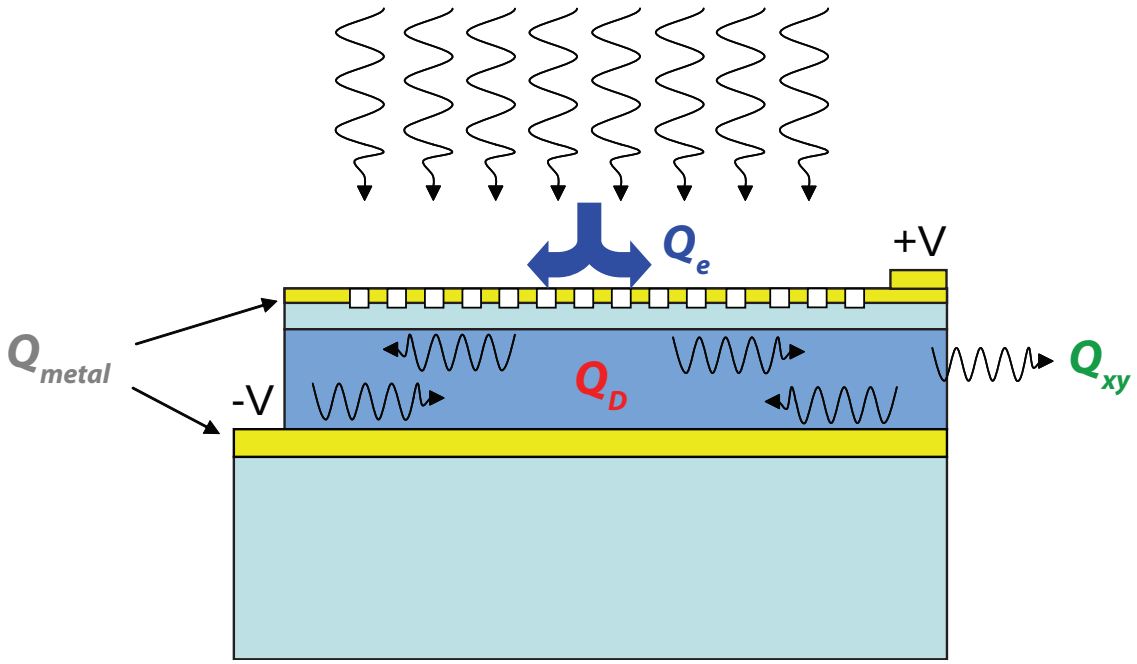

Figure 1.12: The dominant loss mechanisms within a double-metal plasmonic photonic crystal resonant detector.

Critical coupling occurs when the external coupling to the resonator (the resonator "coupling loss") is equal to the total internal cavity loss from all other loss mechanisms. When that condition occurs, the reflection coefficient goes to zero, and all of the incident light at the resonance frequency is absorbed in the resonator [27]. Figure 1.12 shows the various scattering and absorption processes that are involved in near normal incidence resonant detection. The reflection from the cavity is given by

$$R = \frac{\Delta^2 + \left(\frac{\gamma_0 - \gamma_e}{2}\right)^2}{\Delta^2 + \left(\frac{\gamma_t}{2}\right)^2}, \tag{1.5}$$

where $\Delta = \omega - \omega_0$ is the frequency detuning from the resonance frequency ω_0, γ_0 is the intrinsic cavity loss rate, γ_e is the vertical coupling rate to free space, and $\gamma_t = \gamma_0 + \gamma_e$. The loss rates γ are related to the Q-factors given previously by $\gamma = n\lambda Q/2\pi c$. It is clear from Eq. 1.5 that, when the cavity is excited on-resonance ($\Delta = 0$), the reflection goes to zero when $\gamma_0 = \gamma_e$, when the rate at which the cavity can be fed from free space is equal to the sum of all the internal cavity loss rates. This is the critical coupling condition.

From the expression for the reflection in Eq. 1.5, we can write the power dropped into the cavity

(not only the absorbed power, but all of the power not reflected):

$$P_d = P_{in}(1-R) = P_{in}\frac{\gamma_0\gamma_e}{\Delta^2 + \left(\frac{\gamma_t}{2}\right)^2}, \tag{1.6}$$

where P_{in} represents the power incident on the cavity. Therefore the fractional absorption efficiency into the i-th loss channel is

$$p_i = \frac{\gamma_i}{\gamma_0}\frac{P_d}{P_{in}} = \frac{\gamma_i\gamma_e}{\Delta^2 + \left(\frac{\gamma_t}{2}\right)^2}. \tag{1.7}$$

We can enumerate the loss mechanisms in Fig. 1.12, such that $\gamma_0 = \gamma_D + \gamma_{\text{metal}} + \gamma_{xy} + \gamma_{\text{sub}}$, corresponding to the (beneficial) detector absorption, the metal absorption, the in-plane loss, and the substrate loss, respectively. The in-plane loss can always be made negligible, by adding more lattice constants to the photonic crystal patterning region to increase the in-plane confinement strength relative to the other loss mechanisms. In the single-metal case, we can consider $\gamma_{\text{sub}} = m\gamma_e$, representing a mode coupling into the substrate that is m times larger than that into the air due to the higher substrate refractive index; in the double-metal case, $m \sim 0$ due to the thick bottom layer of plasmon metal.

The fractional absorption into the DWELL detector material is then, at resonance, given by

$$p_D = \frac{4\gamma_D\gamma e}{[(m+1)\gamma_e + \gamma_{\text{metal}} + \gamma_D]^2}. \tag{1.8}$$

From this expression, we see that the maximum fractional absorption occurs at

$$\gamma_e = \frac{\gamma_D + \gamma_{\text{metal}}}{1+m}. \tag{1.9}$$

As the input coupling γ_e can be adjusted by varying resonator parameters, this maximal condition should be readily achievable, corresponding to a fractional absorption into the detector material of

$$p_{D,\max} = \frac{\gamma_D}{(1+m)(\gamma_D + \gamma_{\text{metal}})}. \tag{1.10}$$

For the double-metal case in which $m \sim 0$, the maximal detector absorption occurs at the pure critical coupling condition, $\gamma_e = \gamma_D + \gamma_{\text{metal}}$. In this case, the fractional power absorbed is primarily limited by the relatively small metal losses in the mid-infrared region. For the silver plasmon waveguides simulated in this work, we find a metal loss quality factor of $Q_{\text{metal}} = 149$, in comparison to the

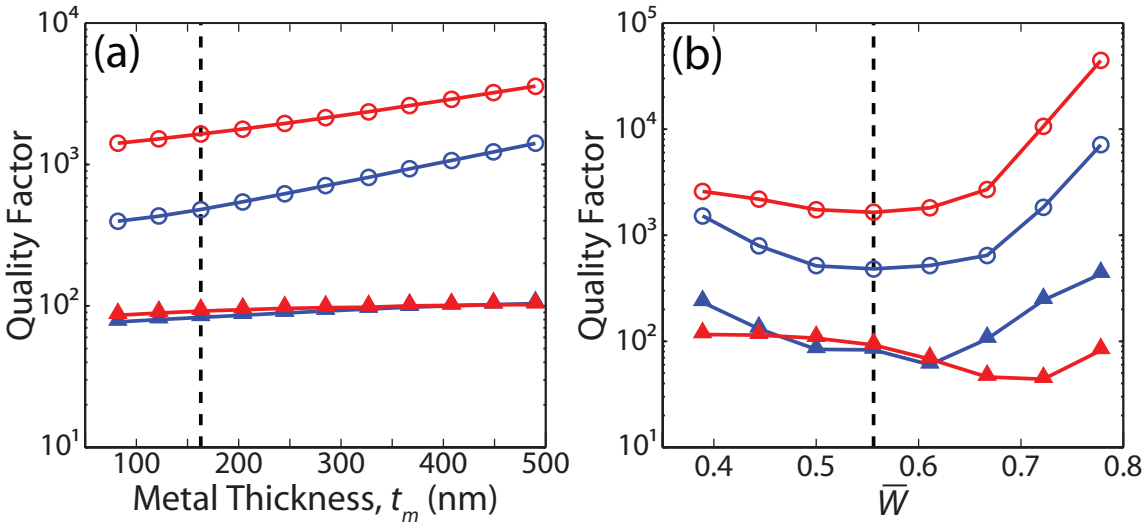

Figure 1.13: (a) Variation of external coupling and substrate loss quality factors, Q_e and Q_{sub}, with metal thickness t_m, and (b) with $\bar{W}$ for the fundamental (blue) and higher-order (red) modes of the unstretched single-metal photonic crystal lattice. Open circles represent Q_e and filled triangles represent Q_{sub}. A dotted line marks the value of the parameter held constant in the opposing plot.

estimated DWELL detector absorption quality factor of $Q_D = 188$. This indicates that 55.8% of the incoming light will be absorbed in the active material for the optimal external coupling quality factor of $Q_e = 83$.

There are many free parameters in this resonator structure which can be optimized in order to achieve the optimal input coupling value. Choosing two of the most significant, the normalized hole width, $\bar{W}$, and the top metal thickness, t_m, we investigate their effect on Q_e for both the single-metal unstretched lattice (Fig. 1.13) and double-metal stretched-lattice (Fig. 1.14, with a lattice stretching ratio of 1.2) structures. With variation of $\bar{W}$, shown in Figs. 1.13(b) for single-metal and 1.14(b) for double-metal, the overall trend for both structures is the same, showing a curve most likely due to a combination of factors: the increased hole size provides a larger aperture through which light can escape, decreasing the Q_e; but the larger air hole also distorts the shape of the mode, causing it to generate a less pure far-field profile which does not match as well with a free-space beam. In contrast, the variations in quality factor with changes in the top metal thickness, shown in Figs. 1.13(a) for single-metal and 1.14(a) for double-metal, illustrate vertical quality factors Q_e of both dipole-like modes increasing monotonically as the top metal becomes thicker. Varying the top metal thickness t_m is an effective way to change Q_e to better match the internal loss, and thus more closely approach critical coupling, without changing the mode frequency.

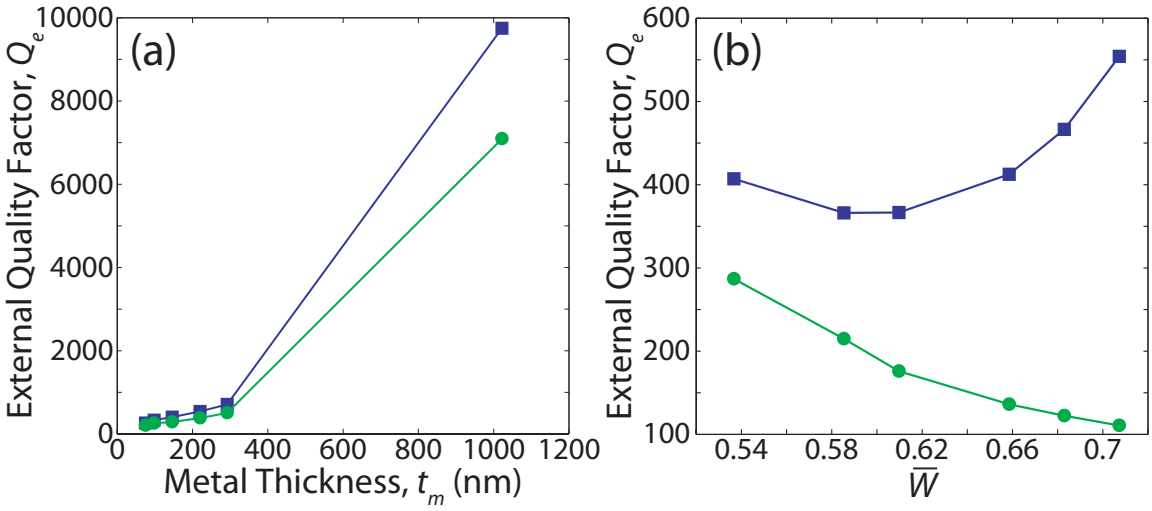

Figure 1.14: Variation of vertical coupling quality factor Q_e of the B_1 (blue square) and B_2 (green circle) modes of the double-metal photonic crystal lattice with changing (a) t_m and (b) $\bar{W}$.

Though the behavior as hole size and metal thickness are varied is similar for both single-metal and double-metal structures, the double-metal structure has a lower achievable Q_e, indicating more favorable external coupling conditions; the stretching of the photonic crystal lattice does not significantly decrease Q_e.

1.7 Conclusion

We have designed a plasmonic photonic crystal resonator utilizing either a single-metal or double-metal plasmon waveguide for use in mid-infrared photodetectors, and experimentally demonstrated single-metal devices with responsivity enhancement of up to 5X. This resonator design shows good frequency and polarization selectivity for use in hyperspectral and hyperpolarization detectors. We theoretically analyzed the conditions for optimal detector absorption enhancement, and by varying the photonic crystal hole size and top metal thickness, we adjusted the vertical coupling efficiency to more closely match the resonator loss, moving towards achieving critical coupling. Additional increases in coupling efficiency or reductions in loss could bring the system to near 100% absorption in the detector. This resonator can be optimized for use at any wavelength from the terahertz to the visible with suitable scaling of the photonic crystal holes and waveguide width, and can easily be modified to suit any detector material, since no photonic crystal holes are etched into the active region itself.

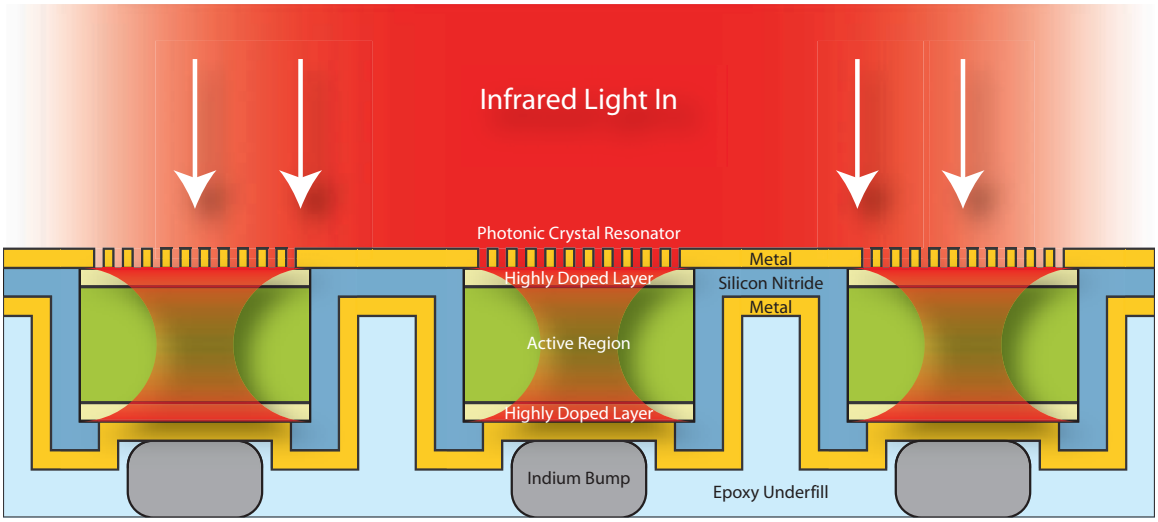

Figure 1.15: A design schematic for a resonant double-metal plasmonic photonic crystal FPA.

The flip-chip bonding method of focal plane array (FPA) fabrication naturally lends itself to use with a double-metal resonant cavity, with only the top metal photonic crystal lithography step differing from standard process techniques. DWELL FPAs have already been demonstrated with hybridization to a readout integrated circuit [4, 28]. In Fig. 1.15, a proposed FPA schematic is shown, illustrating the ease with which double-metal plasmonic photonic crystal resonators can be incorporated into current FPA designs and presenting the possibility to achieve highly sensitive mid-infrared spectral and polarization imaging at low cost.

Chapter 2

Double Disk Optomechanical Resonators

2.1 Introduction

Many precision position measurement devices involve the coupling of mechanical degress of freedom to an electromagnetic interferometer or cavity [29, 30]. Today, cavity-mechanical systems span a wide range of geometries and scales, from multi-kilometer long gravitational-wave detectors [31] to coupled nanomechanical-microwave circuits [32]. For the sensitive detection and actuation of mechanical motion, each of these systems depend upon "dynamical backaction" [33, 34] resulting from the position-dependent feedback of electromagnetic wave momentum. Recent work in the optical domain has used the scattering radiation pressure force to both excite and dampen oscillations of a micro-mechanical resonator [35–41], with the intriguing possibility of self-cooling the mechanical system down to its quantum ground-state. As has been recently proposed [42, 43] and demonstrated [44, 45], the optical gradient force within guided-wave nanostructures can be orders-of-magnitude larger than the scattering force. In this work we combine the large per-photon optical gradient force with the sensitive feedback of a high quality factor whispering-gallery microcavity. The cavity geometry, consisting of a pair of silica disks separated by a nanoscale gap, shows extremely strong dynamical backaction, powerful enough to excite giant coherent oscillations even under heavily damped conditions (mechanical $Q \approx 4$). In vacuum, the threshold for regenerative mechanical oscillation is lowered to an optical input power of only 270 nanoWatts, or roughly 1000 stored cavity photons, and efficient cooling of the mechanical motion is obtained with a temperature compression factor of 13 dB for 4 microWatt of dropped optical input power. These properties of the double-disk resonator make it interesting for a broad range of applications from sensitive force

and mass detection in viscous environments such as those found in biology [46, 47], to quantum cavity-optomechanics in which a versatile, chip-scale platform for studying the quantum properties of the system may be envisioned. This work was initially presented in Ref. 48.

2.2 Optomechanical coupling and dynamic backaction

The per photon force exerted on a mechanical object coupled to the optical field within a resonant cavity is given by $\hbar g_{\mathrm{OM}}$, where $g_{\mathrm{OM}} \equiv \mathrm{d}\omega_c/\mathrm{d}x$ is a coefficient characterizing the dispersive nature of the cavity with respect to mechanical displacement, x. In a Fabry-Perot (Fig. 2.2a) or microtoroid resonator (Fig. 2.2b), the optical force manifests itself as a so-called scattering radiation pressure due to direct momentum transfer from the reflection of photons at the cavity boundary [49, 50]. As the momentum change of a photon per round trip is fixed inside such cavities, while the round-trip time increases linearly with the cavity length, the radiation pressure per photon scales inversely with the cavity size. In contrast, for the gradient optical force the cavity length and the optomechanical coupling can be decoupled, allowing for photon momentum to be transfered over a length scale approaching the wavelength of light [42, 43]. This method was recently employed in a silicon photonic circuit to manipulate a suspended waveguide [44]. However, without the feedback provided by an optical cavity or interferometer, the optical force only provides a static mechanical displacement.

In the case of a cavity optomechanical system, dynamical backaction can be quantified by considering the magnitude of the damping/amplification that an input laser has on the mechanical motion. For a fixed absorbed optical input power in the bad-cavity limit ($\kappa \gg \Omega_m$), the maximum rate is given by

$$\Gamma_{m,\mathrm{opt}} \approx \left(\frac{3 \quad \overline{3} g_{\mathrm{OM}}^2}{\kappa_i^3 \omega_c m_x}\right)\left(\frac{1}{(1+K)^2}\right) P_d, \tag{2.1}$$

where ω_c is the optical cavity resonance frequency, m_x is the motional mass of the optomechanical system, P_d is the optical power dropped (absorbed) within the cavity, and $K \equiv \kappa_e/\kappa_i$ is a cavity loading parameter (κ_i, the intrinsic energy loss rate of the optical cavity; κ_e, the energy coupling rate between external laser and internal cavity fields). The effectiveness of the coupling between the optical and mechanical degrees of freedom can thus be described by a back-action parameter, $B = g_{\mathrm{OM}}^2/\left(\kappa_i^3 \omega_c m_x\right)$, which depends upon the motional mass, the per-photon force, and the optical cavity Q-factor.

2.3 Double-disk fabrication, optical, and mechanical design

Here we describe the design, fabrication, and characterization of a nano-optomechanical system (NOMS) consisting of a pair of optically thin disks separated by a nanoscale gap. The double-disk structure (Fig. 2.2c) supports high-Q whispering-gallery resonances, and provides back-action several orders of magnitude larger than in previously demonstrated gradient force optomechanical systems [44, 45] (very recent work [51] involving the versatile coupling of external nanomechanical elements to the near-field of a high-Finesse microtoroid has realized very strong dynamical back-action, although still roughly two-orders of magnitude smaller than in our integrated device).

Fabrication of the double-disk whispering-gallery resonator began with initial deposition of the cavity layers. The two silica disk layers and the sandwiched amorphous silicon (α-Si) layer were deposited on a (100) silicon substrate by plasma-enhanced chemical vapor deposition, with a thickness of 340 ± 4 nm and 158 ± 3 nm for the silica and α-Si layers, respectively. The wafer was then thermally annealed in a nitrogen environment at a temperature of $T = 1050$ K for 6 hours to drive out water and hydrogen in the film, improving the optical quality of the material. The disk pattern was created using electron beam lithography followed by an optimized C_4F_8-SF_6 gas chemistry reactive ion etch. Release of the double-disk structure was accomplished using a SF_6 chemical plasma etch which selectively $(30,000 : 1)$ attacks the intermediate α-Si layer and the underlying Si substrate, resulting in a uniform undercut region between the disks extending radially inwards 6 μm from the disk perimeter. Simultaneously, the underlying silicon support pedestal is formed. The final gap size between the disks was measured to be 138 ± 8 nm (shrinkage having occurred during the anneal step). Two nanoforks were also fabricated near the double-disk resonator to mechanically stabilize and support the fiber taper during optical coupling; the geometry was optimized such that the forks introduce a total insertion loss of only $\sim 8\%$.

The final double-disk structure, shown in Fig. 2.4, consists of 340-nm-thick silica disks separated by a ~ 140 nm air gap extending approximately 6 μm in from the disk perimeter (the undercut region). Two different sized cavities are studied here, one large ($D = 90$ μm; Sample I) and one small ($D = 54$ μm; Sample II) in diameter. The small diameter cavity structure represents a minimal cavity size, beyond which radiation loss becomes appreciable ($Q_r \sim 10^8$).

Finite element method (FEM) simulations of the whispering-gallery optical modes of the double-disk structure shows substantial splitting of the cavity modes into even and odd parity bonded and anti-bonded modes (Fig. 2.2(e-f)). Due to its substantial field intensity within the air gap, the bonded

mode tunes rapidly with changing gap size as shown in the inset to Fig. 2.2(g). As the mode confinement in a double-disk NOMS is primarily provided by the transverse boundaries formed by the two disks, the double-disk structure can be well approximated by a symmetric double-slab waveguide shown in Fig. 2.1.

For the bonding mode polarized along the $\hat{e}_y$ direction, the tangential component of the electric field is given by:

$$E_y = \begin{cases} Ae^{-\gamma x}, & x > h + x_0/2 \\ B\cos\kappa x + C\sin\kappa x, & x_0/2 < x < h + x_0/2 \\ D\cosh\gamma x, & -x_0/2 < x < x_0/2 \\ B\cos\kappa x - C\sin\kappa x, & -x_0/2 > x > -h - x_0/2 \\ Ae^{\gamma x}, & x < -h - x_0/2 \end{cases} \tag{2.2}$$

where κ is the transverse component of the propagation constant inside the slabs and γ is the field decay constant in the surrounding area. They are given by the following expressions:

$$\kappa^2 = k_0^2 n_c^2 - \beta^2, \qquad \gamma^2 = \beta^2 - k_0^2 n_s^2, \tag{2.3}$$

where $k_0 = \omega_0/c$ is the propagation constant in vacuum and $\beta = k_0 n_{\text{eff}}$ is the longitudinal component of the propagation constant of the bonding mode. n_{eff} is the effective refractive index for the guided mode. Accordingly, the tangential component of the magnetic field can be obtained through $H_z = \frac{-i}{\mu\omega_0}\frac{\partial E_y}{\partial x}$. The continuity of E_y and H_z across the boundaries requires κ and γ to satisfy the following equation:

$$\kappa\gamma[1 + \tanh(\gamma x_0/2)] = \left[\kappa^2 - \gamma^2 \tanh(\gamma x_0/2)\right] \tan\kappa h, \tag{2.4}$$

which reduces to $\tan\kappa h = \gamma/\kappa$ when $x_0 \quad 0$, as expected.

The circular geometry of the double disk forms the whispering-gallery mode, in which the resonance condition requires the longitudinal component of the propagation constant, β, to be fixed as $2\pi R\beta = 2m\pi$, where R is the mode radius and m is an integer. Thus, any variation on the disk spacing x_0 transfers to a variation on the resonance frequency ω_0 through Eqs. (2.3) and (2.4), indicating that ω_0 becomes a function of x_0. By using these two equations, we find that the optomechanical

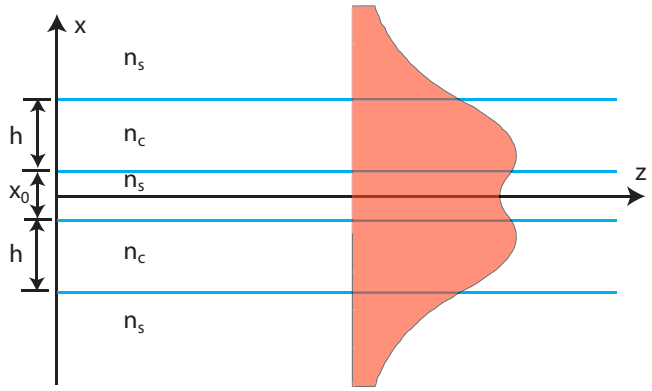

Figure 2.1: Schematic of a symmetric double-slab waveguide. h and x_0 are the slab thickness and the slab spacing, respectively. n_c and n_s are the refractive indices for the slab and surrounding area, respectively.

coupling coefficient, $g_{\mathrm{OM}} = \frac{d\omega_0}{dx_0}$, is given by the general form

$$g_{\mathrm{OM}}(x_0) = \frac{\frac{c\chi\gamma^2}{k_0}\mathrm{sech}^2\left(\frac{\gamma x_0}{2}\right)}{4(n_c^2-n_s^2)\tan\kappa h + n_s^2 x_0 \chi \mathrm{sech}^2\left(\frac{\gamma x_0}{2}\right) + 2\xi\left[(n_c^2\gamma h\csc^2\kappa h + 2n_s^2)\tan\kappa h + \frac{n_s^2\kappa}{\gamma} - \frac{n_c^2\gamma}{\kappa}\right]} \tag{2.5}$$

where $\chi \equiv \kappa + \gamma\tan\kappa h$ and $\xi \equiv 1 + \tanh(\frac{\gamma x_0}{2})$.

When x_0 0, Eq. (2.5) leads to the maximum optomechanical coupling of

$$g_{\mathrm{OM}}(0) = \frac{\omega_0\gamma^3}{2\beta^2 + 2k_0^2 n_c^2 \gamma h}. \tag{2.6}$$

In analogy to Fabry-Perot cavities and microtoroids, the magnitude of the optomechanical coupling can be characterized by an effective length, L_{OM}, defined such that $g_{\mathrm{OM}} \equiv \frac{\omega_0}{L_{\mathrm{OM}}}$. Equation (2.6) infers a minimum effective length

$$L_0 = \frac{2}{\gamma}\left[1 + \frac{k_0^2}{\gamma^2}(n_s^2 + n_c^2\gamma h)\right] = \frac{\lambda_0}{\pi}\frac{n_{\mathrm{eff}}^2 + k_0 h n_c^2\sqrt{n_{\mathrm{eff}}^2 - n_s^2}}{\left(n_{\mathrm{eff}}^2 - n_s^2\right)^{3/2}}, \tag{2.7}$$

which is approximately on the order of the optical wavelength λ_0.

Physically, as the two slabs are coupled through the evanescent field between them with amplitude decaying exponentially with slab spacing at a rate γ [see Eq. (2.2)], the resulting optomechani-

cal coupling can be well approximated by an exponential function

$$g_{\mathrm{OM}}(x_0) \approx g_{\mathrm{OM}}(0)e^{-\gamma x_0}, \tag{2.8}$$

where $g_{\mathrm{OM}}(0)$ is given by Eq. (2.6). As indicated by the red curve in Fig. 2.2(g), Eq. (2.8) provides an excellent approximation for the optomechanical coupling coefficient in a double-disk NOMS. Therefore, the approximate effective length, $L_{\mathrm{OM}} \approx \frac{\omega_0}{g_{\mathrm{OM}}(0)}e^{\gamma x_0}$, agrees well with the results simulated by the finite element method, shown in Fig. 2.2(g), and the effective length decreases roughly exponentially with decreasing disk spacing, reaching a minimum value of 3.8 μm at a resonance optical wavelength of $\lambda_c \approx 1.5$ μm. For the air gap of 138 nm used in this work, the optomechanical coupling is estimated to be $g_{\mathrm{OM}}/2\pi = 33$ GHz/nm ($L_{\mathrm{OM}} = 5.8$ μm), equivalent to 22 fN/photon.

The double-disk structure also supports a number of different micro-mechanical resonances, ranging from radial breathing modes to whispering-gallery-like vibrations of the disk perimeter. The most strongly coupled mechanical resonance is that of the symmetric (i.e., azimuthal mode number, $m = 0$) flapping motion of the disks. With a clamped inner edge and a free outer edge, the mechanical displacement of a double disk exhibiting a flapping mode is generally a function of radius (Fig. 2.3). What matters for the optomechanical effect, however, is the disk spacing at the place where the whispering-gallery mode is located, as that determines the magnitude of the splitting between the bonding and antibonding cavity modes.

As the mechanical displacement actuated by the gradient force is generally small compared with the original disk spacing x_0, we can assume it is uniform in the region of the whispering-gallery mode and define the effective disk spacing $x_m(r_0)$ at the mode center, where r_0 is the radius of the whispering-gallery mode. The effective mechanical displacement is then given by $x_{\mathrm{eff}} = x_m(r_0) - x_0$, corresponding to an effective mechanical potential energy of $E_p = m_x\Omega_m^2 x_{\mathrm{eff}}^2/2$, where m_x is the corresponding effective motional mass and Ω_m is the resonance frequency of the flapping mode. Note that x_{eff} is twice the real displacement at the mode center for a single disk, $x_{\mathrm{eff}} = 2d(r_0)$. E_p reaches its maximum value when the double disk is at rest at its maximum displacement, at which point all of the mechanical energy is stored in the strain energy U_s. Therefore, $E_p = U_s$ and the effective motional mass is given by

$$m_x = \frac{2U_s}{\Omega_m^2[x_m(r_0) - x_0]^2} = \frac{U_s}{2\Omega_m^2 d^2(r_0)}, \tag{2.9}$$

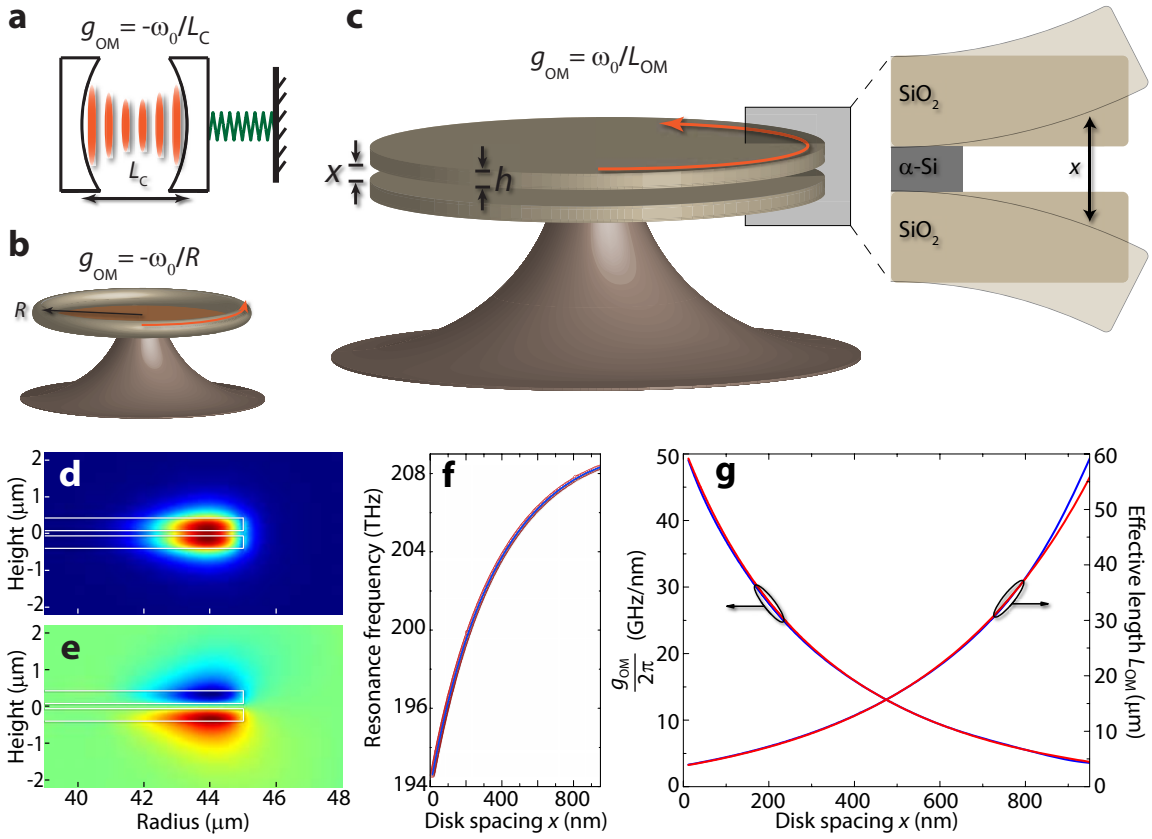

Figure 2.2: Schematic of the corresponding (a) Fabry-Parot and (b) microtoroid optomechanical cavities. (c) Schematic of the double-disk NOMS structure, showing the mechanical flapping motion of the disks. FEM-simulated optical mode profiles of the radial component of the electric field for the (d) bonded mode at $\lambda = 1520$ nm and (e) antibonded mode at $\lambda = 1297.3$ nm. (f) FEM-simulated tuning curve of the bonded mode. (g) Optomechanical coupling coefficient and effective length (blue curves) for the bonded mode. g_{OM} and L_{OM} are both well-approximated by exponential functions (red curves).

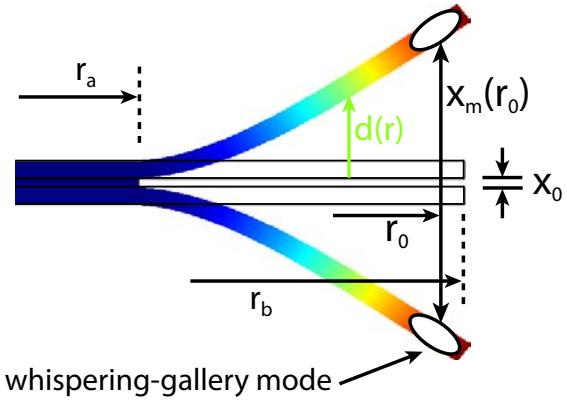

Figure 2.3: Illustration of the disk displacement. x_0 is the disk spacing in the absence of the optical field. r_0 is the radius of the whispering-gallery mode. $x_m(r_0)$ corresponds to the effective disk spacing at the mode center. r_a and r_b are the inner and outer radii of the disk region involved in the flapping motion. $d(r)$ is the mechanical displacement at radius r.

where both U_s and $d(r_0)$ can be obtained from the mechanical simulations by the finite element method.

The relationship between the effective mass and the physical mass of the double-disk NOMS can be found by examining the mechanical potential energy. With a mechanical displacement $d(r)$ for each single disk [Fig. 2.3], we can find the total mechanical potential energy by integrating over the disk regions involved in the flapping motion:

$$E_p = \int_{r_a}^{r_b} \Omega_m^2 d^2(r) \zeta 2\pi r h dr, \tag{2.10}$$

where ζ is the material density, h is the thickness for a single disk, and r_a and r_b are the inner and outer radii of the disk region involved in the flapping motion (see Fig. 2.3). Note that E_p is the total potential energy for the two disks, which is simply two times that of a single one because of the symmetry between the two disks. As the physical mass of a single disk region involved in the flapping motion is given by $m_p = \pi\zeta h(r_b^2 - r_a^2)$, using Eq. (2.10), we find that the effective mass is related to the physical mass through the following expression:

$$m_x = \frac{4m_p}{(r_b^2 - r_a^2)\left[x_m(r_0) - x_0\right]^2} \int_{r_a}^{r_b} r d^2(r) dr = \frac{m_p}{(r_b^2 - r_a^2)\, d^2(r_0)} \int_{r_a}^{r_b} r d^2(r) dr. \tag{2.11}$$

As the whispering-gallery mode is generally located close to the disk edge (*i.e.*, the mode radius $r_0 = 44$ μm in a double disk with $r_b = 45$ μm), $d^2(r)/d^2(r_0) \ll 1$ for most of the region between

r_a and r_b, and Eq. (2.11) shows that $m_x \ll m_p/2$. Therefore, the effective mass is significantly less than half the physical mass of a single disk region. In practice, the effective mass is much smaller than this value because of the real displacement function $d(r)$. For the 90-μm device used in our experiment, with an 6 μm undercut air gap region involved in the flapping motion (Fig. 2.2c and Fig. 2.4), the effective mass is 0.264 nanogram, only about one fifth of the physical mass of a single disk region $m_p = 1.18$ nanogram. The effective mass decreases to 0.145 nanogram for the 54-μm device, due to the decrease in the disk radius. Note that both these values are more than two orders of magnitude smaller than commonly used micromirrors and microtoroids [36–41, 49], and in combination with the large per-photon force, provide a significant enhancement to the dynamic back-action parameter which scales as $g_{\rm OM}^2/m_x$.

2.4 Optical and mechanical characterization

Optical and mechanical measurements were initially performed at room temperature in a one atmosphere nitrogen environment. Fig. 2.6(a) shows the wavelength scan of a large diameter double-disk cavity (Sample I). Several radial-order whispering-gallery modes are evident in the spectrum, all of them of TE-like polarization and bonded mode character. The fundamental TE-like bonded optical mode at $\lambda = 1518.57$ nm is shown in the Fig. 2.6(a) inset, from which an intrinsic optical Q-factor of 1.75×10^6 is inferred, taking into account the mechanical perturbations.

Unlike other microcavities in which the linear transmission is determined only by the cavity loss and dispersion, for the double-disk NOMS, even the small thermal Brownian motions of the flapping mode introduce significant perturbations to the cavity resonance due to the large optomechanical coupling, leading to considerably broadened cavity transmission. Figure 2.5(a) shows an example of the cavity transmission of Sample I. With a small input power of 5.8 μW well below the oscillation threshold, the cavity transmission exhibits intense fluctuations when the laser frequency is scanned across the cavity resonance. As a result, the averaged spectrum of the cavity transmission (red curve) is significantly broader than the real cavity resonance. A correct description of the cavity transmission requires an appropriate inclusion of the optomechanical effect, which is developed in the following.

When the optical power is well below the oscillation threshold and the flapping mode of the double disk is dominantly driven by thermal fluctuations, the mechanical motion can be described

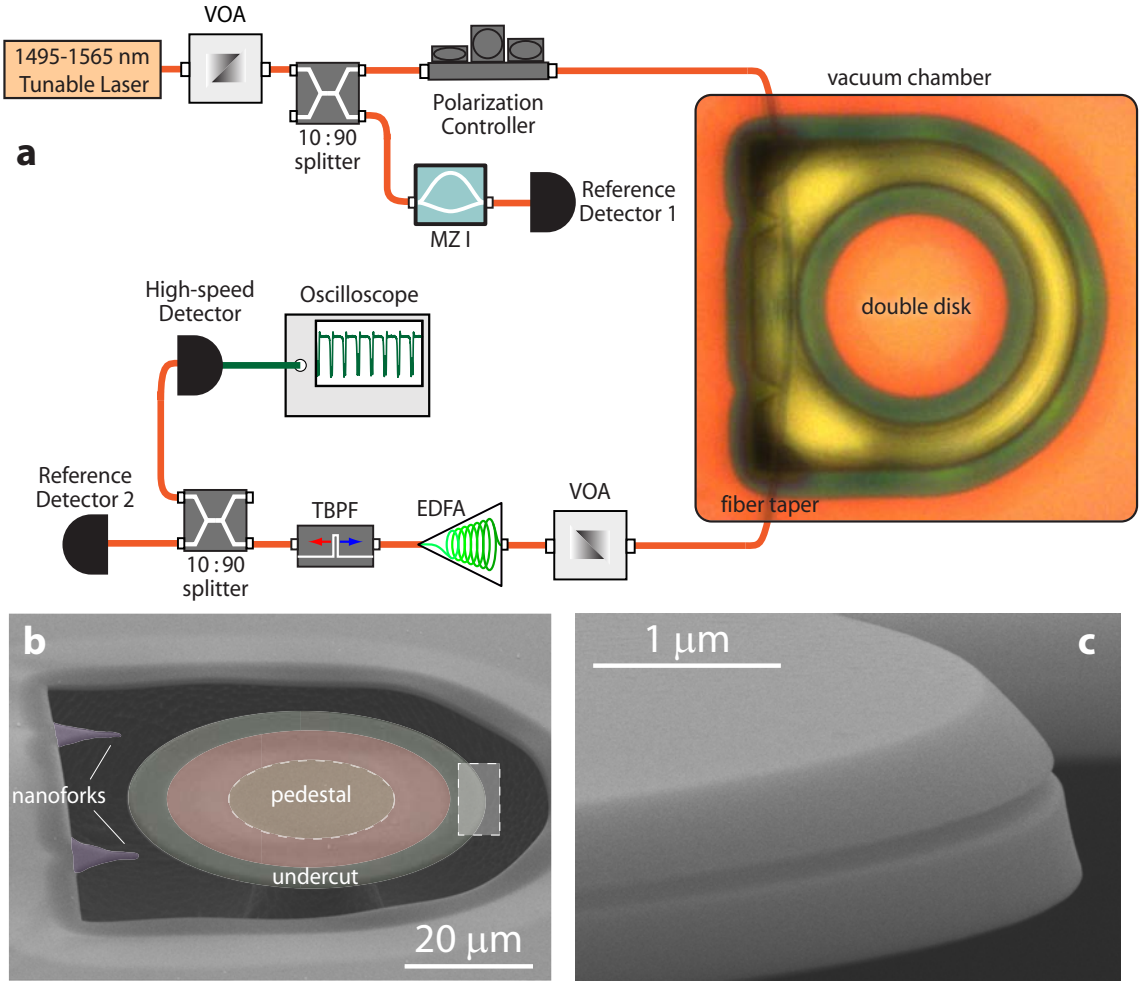

Figure 2.4: (a) Schematic of the experimental setup for optical testing of the double-disk cavity. The cavity input and transmission are both transported through a single-mode silica fiber taper, which is supported by two nanoforks for stable operation. A tunable laser source is used to optically probe and actuate the double-disk structure, with input power controlled by a variable optical attenuator (VOA) and wavelength calibrated by a Mach-Zehnder interferometer (MZI). For experiments performed in a nitrogen environment, the cavity transmission is sent directly to the photodetectors, while it is first amplified by an erbium-doped fiber amplifier (EDFA) for the experiments performed in vacuum. (b,c) Scanning electron microscope images of the 54-μm double-disk NOMS. False color is used to indicate different relevant regions of the device.

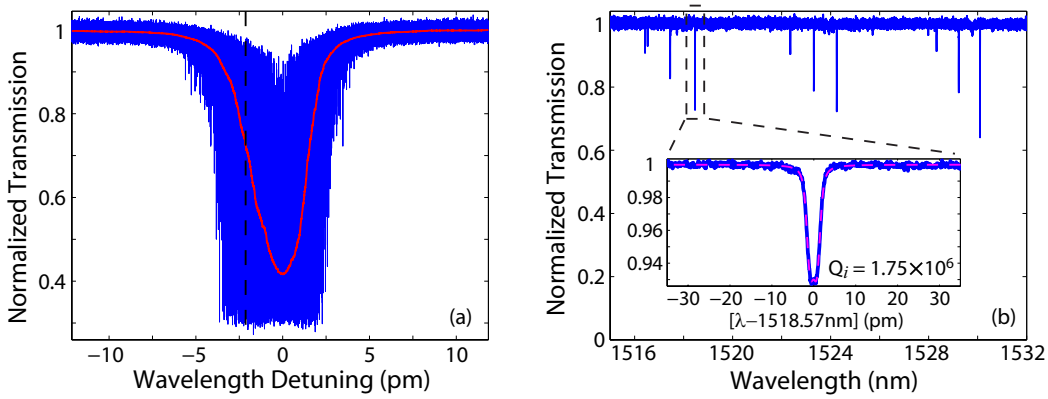

Figure 2.5: (a) The cavity transmission of Sample I in a nitrogen environment, when the laser is scanned across the cavity resonance at 1518.57 nm with an input power of 5.8 μW. The blue curve is the instantaneous signal collected by the high-speed detector and the red curve is the average signal collected by the slow reference detector 2. The slight asymmetry in the transmission spectrum is due to the static component of mechanical actuation when the laser is scanned from blue to red. The dashed line indicates the laser frequency detuning used to record the power spectral density shown in the top panel of Fig. 2.6(b). (b) Linear scan of the averaged cavity transmission of Sample I at an input power of 2.9 μW. The inset shows a detailed scan for the bonding mode at 1518.57 nm, with the experimental data in blue and the theoretical fitting in red.

by the following equation:

$$\frac{d^2x}{dt^2}+\Gamma_m\frac{dx}{dt}+\Omega_m^2 x=\frac{F_T(t)}{m_x}, \tag{2.12}$$

where Ω_m, Γ_m, and m_x are the resonance frequency, damping constant, and effective mass of the flapping mode, respectively. F_T is the Langevin force driving the mechanical Brownian motion, a Markovin process with the following correlation function:

$$F_T(t)F_T(t+\tau) \ = 2m_x\Gamma_m k_B T\delta(\tau), \tag{2.13}$$

where T is the temperature and k_B is Boltzmann's constant. It can be shown easily from Eqs. (2.12) and (2.13) that the Brownian motion of the flapping mode is also a Markovin process with a spectral correlation given by $\widetilde{x}(\Omega_1)\widetilde{x}^*(\Omega_2) \ = 2\pi S_x(\Omega_1)\delta(\Omega_1-\Omega_2)$, where $\widetilde{x}(\Omega)$ is the Fourier transform of the mechanical displacement $x(t)$ defined as $\widetilde{x}(\Omega)=\int_{-\infty}^{+\infty}x(t)e^{i\Omega t}dt$, and $S_x(\Omega)$ is the spectral intensity for the thermal mechanical displacement with the following form:

$$S_x(\Omega)=\frac{2\Gamma_m k_B T/m_x}{(\Omega_m^2-\Omega^2)^2+(\Omega\Gamma_m)^2}. \tag{2.14}$$

The time correlation of the mechanical displacement is thus given by

$$x(t)x(t+\tau) \ = \frac{1}{2\pi}\int_{-\infty}^{+\infty} S_x(\Omega)e^{-i\Omega\tau}d\tau \equiv \ x^2 \ \rho(\tau) \approx \ x^2 \ e^{-\Gamma_m \tau /2}\cos\Omega_m\tau, \tag{2.15}$$

where $x^2 \ = k_BT/(m_x\Omega_m^2)$ is the variance of the thermal mechanical displacement and $\rho(\tau)$ is the normalized autocorrelation function for the mechanical displacement.

To be general, we consider a doublet resonance in which two optical fields, one forward and the other backward propagating, circulate inside the microcavity and couple via Rayleigh scattering from the surface roughness. The optical fields inside the cavity satisfy the following equations:

$$\frac{da_f}{dt} = (i\Delta_0 - \kappa/2 - ig_{\rm OM}x)a_f + i\eta a_b + i \ \ \overline{\kappa_e}A_{in}, \tag{2.16}$$

$$\frac{da_b}{dt} = (i\Delta_0 - \kappa/2 - ig_{\rm OM}x)a_b + i\eta a_f, \tag{2.17}$$

where a_f and a_b are the forward and backward whispering-gallery modes (WGMs), normalized such that $U_j = \ a_j \ ^2$ $(j = f,b)$ represents the mode energy. A_{in} is the input optical wave, normalized such that $P_{in} = \ A_{in} \ ^2$ represents the input power. κ is the photon decay rate for the loaded cavity, and κ_e is the photon escape rate associated with the external coupling. $\Delta_0 = \omega - \omega_0$ is the frequency detuning from the input wave to the cavity resonance and η is the mode coupling coefficient. In the case of a continuous-wave input, Eqs. (2.16) and (2.17) provide a formal solution of the forward WGM:

$$a_f(t) = i \ \ \overline{\kappa_e}A_{in}\int_0^{+\infty}\cos(\eta\tau)f(\tau)e^{-ig_{\rm OM}\int_0^\tau x(t-\tau\,)d\tau}\,d\tau, \tag{2.18}$$

where $f(\tau) \equiv e^{(i\Delta_0-\kappa/2)\tau}$ represents the cavity response. Using Eq. (2.15), we find that the statistically averaged intracavity field is given as:

$$a_f(t) \ = i \ \ \overline{\kappa_e}A_{in}\int_0^{+\infty}\cos(\eta\tau)f(\tau)e^{-\frac{\varepsilon}{2}h(\tau)}d\tau, \tag{2.19}$$

where $\varepsilon \equiv g_{\rm OM}^2 \ x^2$ and $h(\tau)$ is defined as

$$h(\tau) \equiv \iint_0^\tau \rho(\tau_1-\tau_2)d\tau_1 d\tau_2. \tag{2.20}$$

Similarly, we can find the averaged energy for the forward WGM as:

$$\begin{aligned} U_f(t) &= \kappa_e P_{in} \iint_0^{+\infty} f(\tau_1) f^*(\tau_2) \cos(\eta\tau_1) \cos(\eta\tau_2) e^{-\frac{\varepsilon}{2} h(\tau_1 - \tau_2)} d\tau_1 d\tau_2 \\ &= \frac{\kappa_e P_{in}}{2\kappa} \frac{\kappa - i\eta}{\kappa - 2i\eta} \int_0^{+\infty} e^{-\frac{\varepsilon}{2} h(\tau)} \left[f_c(\tau) + f_s^*(\tau) \right] d\tau + c.c., \end{aligned} \tag{2.21}$$

where $f_j(\tau) \equiv e^{(i\Delta_j - \kappa/2)\tau}$ $(j = c, s)$, with $\Delta_c = \Delta_0 + \eta$ and $\Delta_s = \Delta_0 - \eta$. $c.c.$ denotes complex conjugate.

As the transmitted power from the double disk is given by

$$P_T(t) = P_{in} + \kappa_e U_f(t) + i \quad \overline{\kappa_e} \left[A_{in}^* a_f(t) - A_{in} a_f^*(t) \right], \tag{2.22}$$

the averaged cavity transmission, $T \equiv P_T / P_{in}$, thus takes the form

$$T = 1 - \frac{\kappa_e \kappa_i}{2\kappa} \left\{ \left[1 - \frac{i\eta\kappa_e}{\kappa_i(\kappa - 2i\eta)} \right] \int_0^{+\infty} e^{-\frac{\varepsilon}{2} h(\tau)} \left[f_c(\tau) + f_s^*(\tau) \right] d\tau + c.c. \right\}. \tag{2.23}$$

In the case of a singlet resonance, $\eta = 0$ and Eq. (2.23) reduces to the simple form expression

$$T = 1 - \frac{\kappa_e \kappa_i}{\kappa} \int_0^{+\infty} e^{-\frac{\varepsilon}{2} h(\tau)} \left[f(\tau) + f^*(\tau) \right] d\tau. \tag{2.24}$$

In the absence of opto-mechanical coupling, $g_{\mathrm{OM}} = 0$ and Eq. (2.24) reduces to the conventional form of

$$T = 1 - \frac{\kappa_e \kappa_i}{\Delta_0^2 + (\kappa/2)^2}, \tag{2.25}$$

as expected.

Using the theory developed above and fitting the experimental averaged cavity transmission spectrum, we obtain the optical Q factor of the resonance, as shown in Fig. 2.5(b) for Sample I. The same approach is used to describe the cavity transmission of Sample II, given in Fig. 2.6(a).

The radio-frequency (RF) power spectrum of the optical signal transmitted through the cavity (Fig. 2.6(b), top panel) exhibits three clear frequency components at 8.30, 13.6, and 27.9 MHz corresponding to thermally-actuated resonances of the double-disk structure. These values agree well with FEM simulations of the differential flapping mode (7.95 MHz), and the first (14.2 MHz) and second (28.7 MHz) order radial breathing modes (Fig. 2.6c). The strong dynamic back-action of the flapping mode (under thermal excitation) also produces a broadband spectral background in

the RF spectrum with a shoulder at the second harmonic frequency. A correct description of the power spectrum (Fig. 2.6(b), red curve) shows that the flapping mode has a 3-dB linewidth of 2.1 MHz (mechanical Q-factor, $Q_M = 3.95$), limited by the squeeze-film process of the nitrogen gas between the disks [52].

We can describe the power spectral density of the cavity transmission in the presence of mechanical Brownian motion using a linear-perturbation approximation when the optomechanical effects are small, and a non-perturbation theory, accurate for arbitrarily strong optomechanical effects, when the effects are larger. Both analyses are presented here.

If the induced optomechanical perturbations are small, Eq. (2.18) can be approximated as

$$a_f(t) \approx i \quad \overline{\kappa_e} A_{in} \int_0^{+\infty} \cos(\eta\tau) f(\tau) \left[1 - i g_{\mathrm{OM}} \int_0^{\tau} x(t-\tau\,) d\tau \right] d\tau. \tag{2.26}$$

In this case, the transmitted optical field can be written as $A_T(t) = A_{in} + i \quad \overline{\kappa_e} a_f(t) \approx A_0 + \delta A(t)$, where A_0 is the transmitted field in the absence of the optomechanical effect and δA is the induced perturbation. They take the following forms:

$$A_0 = A_{in} \left[1 - \kappa_e \int_0^{+\infty} \cos(\eta\tau) f(\tau) d\tau \right] \equiv A_{in} \hat{A}_0, \tag{2.27}$$

$$\delta A(t) = i g_{\mathrm{OM}} \kappa_e A_{in} \int_0^{+\infty} d\tau \cos(\eta\tau) f(\tau) \int_0^{\tau} x(t-\tau\,) d\tau\,. \tag{2.28}$$

The transmitted power then becomes $P(t) = \ A_T(t)\ ^2 \approx \ A_0\ ^2 + A_0^* \delta A(t) + A_0 \delta A^*(t)$. It is easy to show that $\ \delta A(t)\ = 0$ and $\ P_T(t)\ = \ A_0\ ^2$. As a result, the power fluctuations, $\delta P(t) \equiv P_T(t) - \ P_T(t)\ $, become

$$\delta P(t) \approx g_{\mathrm{OM}} P_{in} \int_0^{+\infty} d\tau u(\tau) \int_0^{\tau} x(t-\tau\,) d\tau\,, \tag{2.29}$$

where $u(\tau) \equiv i\kappa_e \cos(\eta\tau)[\hat{A}_0^* f(\tau) - \hat{A}_0 f^*(\tau)]$. By using Eq. (2.15), we find the autocorrelation function for the power fluctuation to be

$$\delta P(t) \delta P(t+t_0) \ \approx \varepsilon P_{in}^2 \iint_0^{+\infty} d\tau_1 d\tau_2 u(\tau_1) u(\tau_2) \psi(t_0, \tau_1, \tau_2), \tag{2.30}$$

where $\psi(t_0, \tau_1, \tau_2)$ is defined as

$$\psi(t_0, \tau_1, \tau_2) \equiv \int_0^{\tau_1} d\tau_1 \int_0^{\tau_2} d\tau_2 \rho(t_0 + \tau_1 - \tau_2). \tag{2.31}$$

Taking the Fourier transform of Eq. (2.30), we obtain the power spectral density $S_P(\Omega)$ of the cavity transmission to be

$$S_P(\Omega) \approx g_{\rm OM}^2 P_{in}^2 H(\Omega) S_x(\Omega), \tag{2.32}$$

where $S_x(\Omega)$ is the spectral intensity of the mechanical displacement given in Eq. (2.14) and $H(\Omega)$ is the cavity transfer function given by

$$H(\Omega) = \left| \frac{1}{\Omega} \int_0^{+\infty} u(\tau)(e^{i\Omega\tau} - 1) d\tau \right|^2. \tag{2.33}$$

In the case of a singlet resonance, the cavity transfer function takes the form:

$$H(\Omega) = \frac{\kappa_e^2}{\left[\Delta_0^2 + (\kappa/2)^2\right]^2} \frac{4\Delta_0^2(\kappa_i^2 + \Omega^2)}{\left[(\Delta_0 + \Omega)^2 + (\kappa/2)^2\right]\left[(\Delta_0 - \Omega)^2 + (\kappa/2)^2\right]}. \tag{2.34}$$

In most cases, the photon decay rate inside the cavity is much larger than the mechanical damping rate, $\kappa \gg \Gamma_m$. For a specific mechanical mode at the frequency Ω_m, the cavity transfer function can be well approximated by $H(\Omega) \approx H(\Omega_m)$. In particular, in the sideband-unresolved regime, the cavity transfer function is given by a simple form of

$$H = \frac{4\kappa_e^2 \kappa_i^2 \Delta_0^2}{\left[\Delta_0^2 + (\kappa/2)^2\right]^4}. \tag{2.35}$$

Therefore, Eq. (2.32) shows clearly that, if the optomechanical effect is small, the power spectral density of the cavity transmission is directly proportional to the spectral intensity of the mechanical displacement.

The situation becomes quite complicated when the optomechanical effects are large. From Eq. (2.22), the autocorrelation function for the power fluctuation of the cavity transmission, $\delta P(t) \equiv P_T(t) - \langle P_T \rangle$, is given by

$$\begin{aligned} \delta P(t_1)\delta P(t_2) \;&= \kappa_e^2 \; U_{f1} U_{f2} \; - \kappa_e \; \left(A_{in}^* a_{f1} - A_{in} a_{f1}^*\right)\left(A_{in}^* a_{f2} - A_{in} a_{f2}^*\right) \\ &+ i\kappa_e^{3/2} \left[\; U_{f1}\left(A_{in}^* a_{f2} - A_{in} a_{f2}^*\right) \; + \; U_{f2}\left(A_{in}^* a_{f1} - A_{in} a_{f1}^*\right) \; \right] \\ &- \left[\kappa_e \; U_f \; + i \; \overline{\kappa_e}\left(A_{in}^* \; a_f \; - A_{in} \; a_f^* \; \right)\right]^2, \end{aligned} \tag{2.36}$$

where $U_{fj} = U_f(t_j)$ and $a_{fj} = a_f(t_j)$ $(j = 1, 2)$. Equation (2.36) shows that the autocorrelation function involves various correlations between the intracavity energy and field, all of which can

be found using Eqs. (2.15) and (2.18). For example, we can find the following correlation for the intracavity field:

$$\begin{aligned}&\left(A_{in}^{*}a_{f1}-A_{in}a_{f1}^{*}\right)\left(A_{in}^{*}a_{f2}-A_{in}a_{f2}^{*}\right)\\&=-\kappa_e P_{in}^{2}\iint_{0}^{+\infty}d\tau_1 d\tau_2 C_1 C_2 e^{-\frac{\varepsilon}{2}(h_1+h_2)}\left[f_1 f_2 e^{-\varepsilon\psi}+f_1 f_2^{*}e^{\varepsilon\psi}+c.c.\right],\end{aligned}\tag{2.37}$$

where, in the integrand, $C_j=\cos(\eta\tau_j)$, $h_j=h(\tau_j)$, $f_j=f(\tau_j)$ (with $j=1,2$), and $\psi=\psi(t_2-t_1,\tau_1,\tau_2)$. $h(\tau)$ and $\psi(t_2-t_1,\tau_1,\tau_2)$ are given by Eqs. (2.20) and (2.31), respectively.

Equations (2.20) and (2.31) show that $h(\tau)$ and $\psi(t_2-t_1,\tau_1,\tau_2)$ vary with time on time scales of $1/\Omega_m$ and $1/\Gamma_m$. However, in the sideband-unresolved regime, $\kappa\gg\Gamma_m$ and $\kappa\gg\Omega_m$. As the cavity response function $f(\tau)$ decays exponentially with time at a rate of $\kappa/2$, the integrand in Eq. (2.37) becomes negligible when $\tau_1\gg 2/\kappa$ or $\tau_2\gg 2/\kappa$. Therefore, $\psi(t_2-t_1,\tau_1,\tau_2)$ can be well approximated as

$$\begin{aligned}\psi(t_2-t_1,\tau_1,\tau_2)&=\frac{1}{2\pi\ x^2}\int_{-\infty}^{+\infty}\frac{S_x(\Omega)}{\Omega^2}e^{-i\Omega(t_2-t_1)}\left(e^{-i\Omega\tau_1}-1\right)\left(e^{i\Omega\tau_2}-1\right)d\Omega\\&\approx\frac{\tau_1\tau_2}{2\pi\ x^2}\int_{-\infty}^{+\infty}S_x(\Omega)e^{-i\Omega(t_2-t_1)}d\Omega=\tau_1\tau_2\rho(t_2-t_1).\end{aligned}\tag{2.38}$$

Similarly, $h(\tau)\approx\tau^2$, since $h(\tau)=\psi(0,\tau,\tau)$. Therefore, Eq. (2.37) becomes

$$\left(A_{in}^{*}a_{f1}-A_{in}a_{f1}^{*}\right)\left(A_{in}^{*}a_{f2}-A_{in}a_{f2}^{*}\right)\ \approx-\kappa_e P_{in}^{2}\Phi(\Delta t,C_1C_2),\tag{2.39}$$

where $\Delta t=t_2-t_1$ and $\Phi(\Delta t,C_1C_2)$ is defined as

$$\Phi(\Delta t,C_1C_2)\equiv\iint_{0}^{+\infty}d\tau_1 d\tau_2 C_1 C_2 e^{-\frac{\varepsilon}{2}\left(\tau_1^2+\tau_2^2\right)}\left[f_1 f_2 e^{-\varepsilon\tau_1\tau_2\rho}+f_1 f_2^{*}e^{\varepsilon\tau_1\tau_2\rho}+c.c.\right],\tag{2.40}$$

with $\rho=\rho(\Delta t)$. Following a similar approach, we can find the other correlation terms in Eq. (2.36). Using these terms in Eq. (2.36), we find that the autocorrelation function of the power fluctuations is given by

$$\delta P(t_1)\delta P(t_2)\ \approx\kappa_e^2 P_{in}^2\Phi(\Delta t,\sigma_1\sigma_2)-\left[\kappa_e\ U_f\ +i\ \ \overline{\kappa_e}\left(A_{in}^{*}\ a_f\ -A_{in}\ a_f^{*}\ \right)\right]^2,\tag{2.41}$$

where $\sigma_j = \sigma(\tau_j)$ $(j = 1,2)$ and $\sigma(\tau)$ is defined as

$$\sigma(\tau) \equiv \left[1 - \frac{\kappa_e(\kappa^2 + 2\eta^2)}{\kappa(\kappa^2 + 4\eta^2)}\right]\cos(\eta\tau) + \frac{\eta\kappa_e}{\kappa^2 + 4\eta^2}\sin(\eta\tau). \tag{2.42}$$

Moreover, Eq. (2.19) and (2.21) show that, in the sideband-unresolved regime, a_f and U_f are well approximated by

$$a_f(t) \approx i \overline{\kappa_e} A_{in} \int_0^{+\infty} \cos(\eta\tau) f(\tau) e^{-\frac{\varepsilon}{2}\tau^2} d\tau, \tag{2.43}$$

$$U_f(t) \approx \kappa_e P_{in} \iint_0^{+\infty} f(\tau_1) f^*(\tau_2) \cos(\eta\tau_1)\cos(\eta\tau_2) e^{-\frac{\varepsilon}{2}(\tau_1-\tau_2)^2} d\tau_1 d\tau_2. \tag{2.44}$$

Therefore, we obtain the final term in Eq. (2.41) as

$$\kappa_e\ U_f\ + i\ \ \overline{\kappa_e}\left(A_{in}^*\ a_f\ - A_{in}\ a_f^*\ \right) \approx -\kappa_e P_{in} \int_0^{+\infty} \sigma(\tau)\left[f(\tau) + f^*(\tau)\right] e^{-\frac{\varepsilon}{2}\tau^2} d\tau. \tag{2.45}$$

Using this term in Eq. (2.41), we obtain the final form for the autocorrelation of the power fluctuations:

$$\delta P(t_1)\delta P(t_2) \approx \kappa_e^2 P_{in}^2 \left[\Phi(\Delta t, \sigma_1\sigma_2) - \Phi(\infty, \sigma_1\sigma_2)\right]. \tag{2.46}$$

It can be further simplified if we notice that the exponential function $e^{\pm\varepsilon\tau_1\tau_2\rho(\Delta t)}$ in Eq. (2.40) can be expanded in a Taylor series as

$$e^{\pm\varepsilon\tau_1\tau_2\rho(\Delta t)} = \sum_{n=0}^{+\infty} \frac{(\pm\varepsilon\tau_1\tau_2)^n}{n!}\rho^n(\Delta t). \tag{2.47}$$

Substituting this expression into Eq. (2.40) and using it in Eq. (2.46), we obtain the autocorrelation function for the power fluctuation in the following form

$$\delta P(t)\delta P(t+t_0) \approx \kappa_e^2 P_{in}^2 \sum_{n=1}^{+\infty} \frac{\varepsilon^n \rho^n(t_0)}{n!}\ \left| G_n^* + (-1)^n G_n \right|^2, \tag{2.48}$$

where G_n is defined as

$$G_n \equiv \int_0^{+\infty} \tau^n \sigma(\tau) f(\tau) e^{-\frac{\varepsilon}{2}\tau^2} d\tau. \tag{2.49}$$

In the case of a singlet resonance, $\eta = 0$ and $\sigma(\tau)$ simplifies considerably to $\sigma = \kappa_i/\kappa$. The autocorrelation function for the power fluctuation is still described by Eq. (2.48).

In general, the power spectral density of the cavity transmission is given by the Fourier transform

of Eq. (2.48):

$$S_p(\Omega) = \kappa_e^2 P_{in}^2 \sum_{n=1}^{+\infty} \frac{\varepsilon^n S_n(\Omega)}{n!} \; G_n^* + (-1)^n G_n \; ^2, \tag{2.50}$$

where $S_n(\Omega)$ is defined as

$$S_n(\Omega) = \int_{-\infty}^{+\infty} \rho^n(\tau) e^{i\Omega\tau} d\tau. \tag{2.51}$$

Eq. (2.14) shows that the spectral intensity of the mechanical displacement can be approximated by a Lorentzian function, resulting in an approximated $\rho(\tau)$ given as $\rho(\tau) \approx e^{-\Gamma_m \tau /2} \cos\Omega_m \tau$ [see Eq. (2.15)]. As a result, Eq. (2.51) becomes

$$S_n(\Omega) \approx \frac{1}{2^n} \sum_{k=0}^{n} \frac{n!}{k!(n-k)!} \frac{n\Gamma_m}{(n\Gamma_m/2)^2 + [(2k-n)\Omega_m + \Omega]^2}. \tag{2.52}$$

Combining Eq. (2.50) and (2.52), we can see that, if the optomechanical coupling is significant, the thermal mechanical motion creates spectral components around the harmonics of the mechanical frequency with broader linewidths. As shown clearly in Fig. 2.6(b), the second harmonic is clearly visible. In particular, if the fundamental mechanical linewidth is broad, various frequency components on the power spectrum would smear out, producing a broadband spectral background, as shown in the top panel of Fig. 2.6(b) for Sample I. This phenomenon is similar to the random-field-induced spectral broadening in nuclear magnetic resonance [53] and atomic resonance fluorescence [54].

This theory can be extended easily for the case with multiple mechanical frequencies. In this case, the power spectrum only only exhibits harmonics of each mechanical frequency, but also their frequency sums and differences. As shown in the bottom panel of Fig. 2.6(b), the frequency components near 0 MHz are the differential frequencies and those near 18-20 MHz are the second harmonic and sum frequencies.

2.5 Regenerative oscillation

2.5.1 Ambient pressure

Despite the near-unity mechanical quality factor of the flapping mode, the powerful dynamic back-action in the double-disk structure provides sufficient compensation of mechanical loss to excite regenerative mechanical oscillation. As shown in Fig. 2.6(d), with an input optical power of 760 μW launched at the blue detuned side of the resonance, the induced parametric mechanical instability

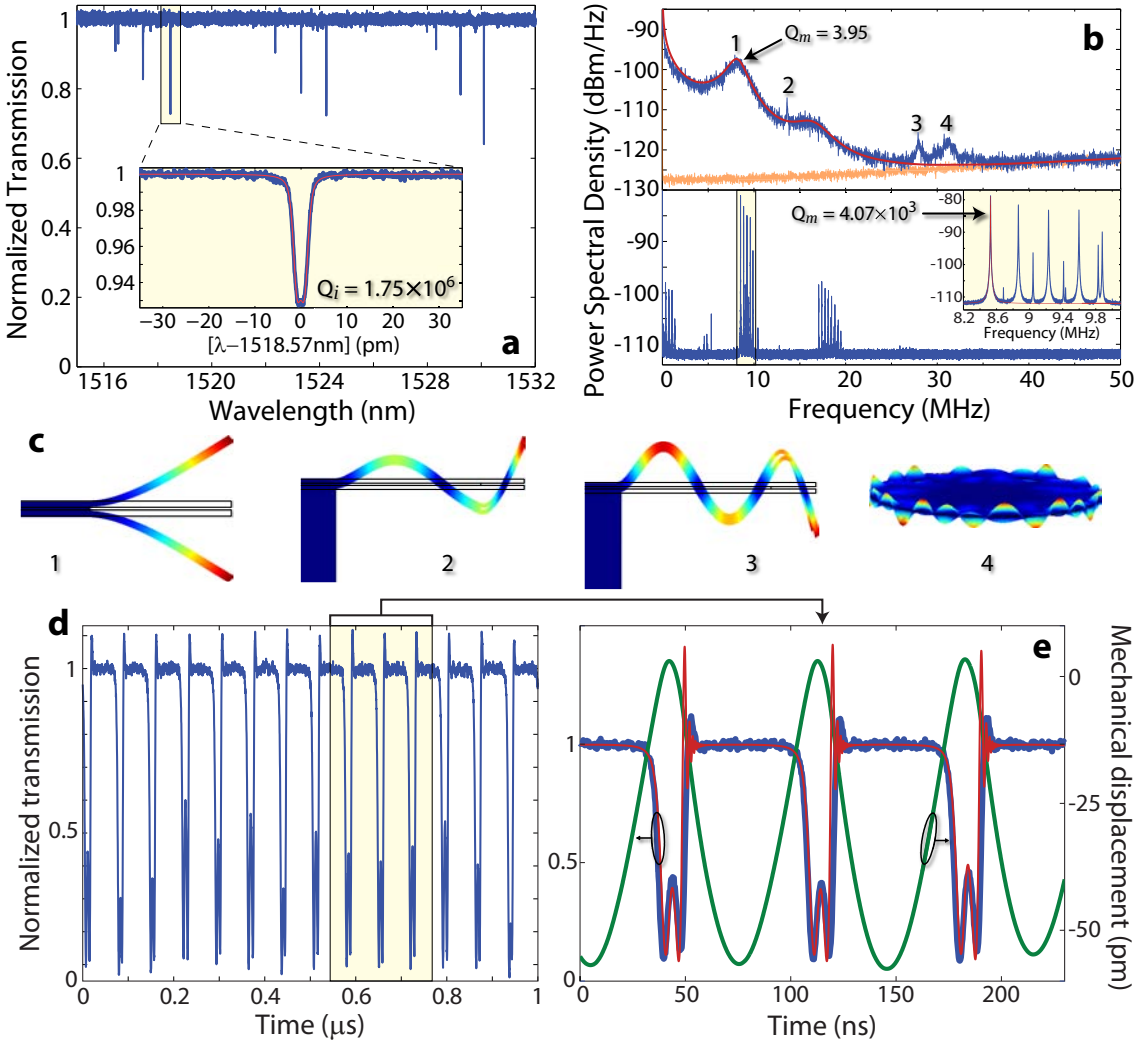

Figure 2.6: (a) Optical transmission spectrum of a large diameter ($D = 90\,\mu$m; Sample I) double-disk cavity. The inset shows the fundamental TE-like bonded mode at $\lambda = 1518.57$ nm. (b) Upper panel: optical transmission power spectral density (PSD) of a Sample I double-disk in the 1 atm. nitrogen environment for $P_i = 5.8\,\mu$W. Experimental data in blue, theoretical modeling in red, and detector noise background in yellow. Lower panel: transmission PSD of a small diameter ($D = 54\,\mu$m; Sample II) double-disk cavity in vacuum for $P_i = 44$ nW. The inset shows a zoom-in of the spectrum around the fundamental flapping mode frequency. (c) FEM simulated mechanical modes indicated in (b). (d) Recorded transmission waveform of Sample I for $P_i = 0.76$ mW. (e) Comparison of experimental (blue curve) and simulated (red curve) waveforms, with the corresponding simulated mechanical displacement (green curve).

causes the cavity transmission to oscillate over the entire coupling depth with a fundamental frequency of 13.97 MHz (this value is about 68% larger than the intrinsic mechanical frequency due to the optical spring effect [55]). A zoom-in of the recorded time waveform (Fig. 2.6e) agrees well with our numerical simulation which shows that the gradient force actuates an extremely large (50 pm) mechanical displacement amplitude, dragging the cavity resonance over more than 10 cavity-linewidths and leaving distinctive features of the Lorentzian cavity transfer function. In particular, two sequential passes of the cavity resonance across the laser frequency can be seen, along with an overshoot and oscillation of the transmitted optical power resulting from the quick release of Doppler shifted photons from the cavity.

The optomechanical oscillations are simulated through the following coupled equations governing the intracavity optical field and mechanical motions, respectively:

$$\frac{da}{dt} = (i\Delta_0 - \frac{\kappa}{2} - ig_{\mathrm{OM}}x)a + i \quad \overline{\kappa_e} A_{in}, \tag{2.53}$$

$$\frac{d^2x}{dt^2} + \Gamma_m \frac{dx}{dt} + \Omega_m^2 x = \frac{F_T(t)}{m_x} + \frac{F_o(t)}{m_x}, \tag{2.54}$$

where we have counted in both the thermal Langevin force F_T and the optical gradient force $F_o = -\frac{g_{\mathrm{OM}}\, a^{\,2}}{\omega_0}$ for actuating mechanical motions.

The threshold for regenerative oscillation depends sensitively upon the optical input power and the average laser-cavity resonance detuning, a map of which can be used to quantify the strength of the dynamic back-action. An estimate of the threshold detuning (Δ_{th}), for a given input power, can be determined from the abrupt kink in the cavity transmission that marks the onset of regenerative oscillation (Fig. 2.8(a) and Fig. 2.7).

Figure 2.7 shows an example of the cavity transmission of Sample I. The mechanical flapping mode starts to oscillate when the input laser frequency is scanned across a certain detuning. Within this detuning value, the same magnitude of optomechanical oscillation is excited over a broad range of laser blue detuning. The intense transmission oscillations cover the entire coupling depth, leaving an abrupt kink on the transmission spectrum. The coupling depth at the kink point, ΔT_{th}, corresponds to the threshold coupling at the given power level, from which we can obtain the threshold frequency detuning Δ_{th}.

The detuning dependence of the optomechanical amplification coefficient can be lumped into a

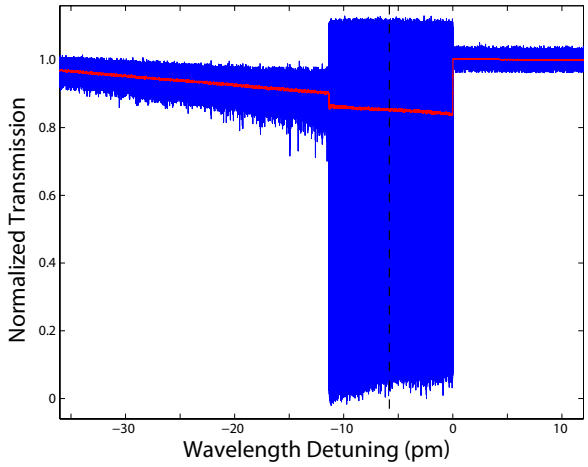

Figure 2.7: Scan of the cavity transmission of Sample I at an input power of 0.76 mW, with the instantaneous and averaged signals shown in blue and red, respectively. The dashed line indicated the laser frequency detuning used to record the time-dependent cavity transmission given in Fig. 2.6(d).

single detuning function,

$$f(\Delta) \equiv \left(\frac{\Delta^2 + (\kappa/2)^2}{\kappa\kappa_e\kappa_i^3\Delta}\right)\left((\Delta+\Omega_m)^2 + \left(\frac{\kappa}{2}\right)^2\right)\left((\Delta-\Omega_m)^2 + \left(\frac{\kappa}{2}\right)^2\right). \tag{2.55}$$

where $\kappa = \kappa_i + \kappa_e$ is the total photon decay rate of the loaded cavity. The right panel of Fig. 2.8(b) shows a map of $f(\Delta_{\rm th})$ versus optical input power for the 90 μm diameter double-disk cavity in the heavily damped nitrogen environment. The data in Fig. 2.8(b), as expected, shows a linear dependence of $f(\Delta_{\rm th})$ on input power, and is well described in the unresolved sideband regime [50] by

$$f(\Delta_{\rm th}) = \frac{2g_{\rm OM}^2 P_i}{\omega_c m_x \Gamma_m \kappa_i^3} = \left(\frac{2B}{\Gamma_m}\right) P_i, \tag{2.56}$$

where $\Gamma_m = 2.1$ MHz is the bare mechanical damping rate of the flapping mode. Fitting of eq. (2.56) to the data in Fig. 2.8(b) yields a dynamic back-action parameter of $B = 0.061$ MHz/μW, corresponding to an optomechanical coupling factor of $g_{\rm OM}/2\pi = 33.8 \pm 0.4$ GHz/nm, in good agreement with the simulated result of 33 GHz/nm.

2.5.2 Vacuum

In order to eliminate the squeeze-film damping of the nitrogen environment, measurements were also performed in vacuum ($P < 5 \times 10^{-4}$ Torr). The significantly reduced mechanical linewidth in vacuum shows that the flapping mode consists of a small cluster of modes (Fig. 2.6(b), bottom

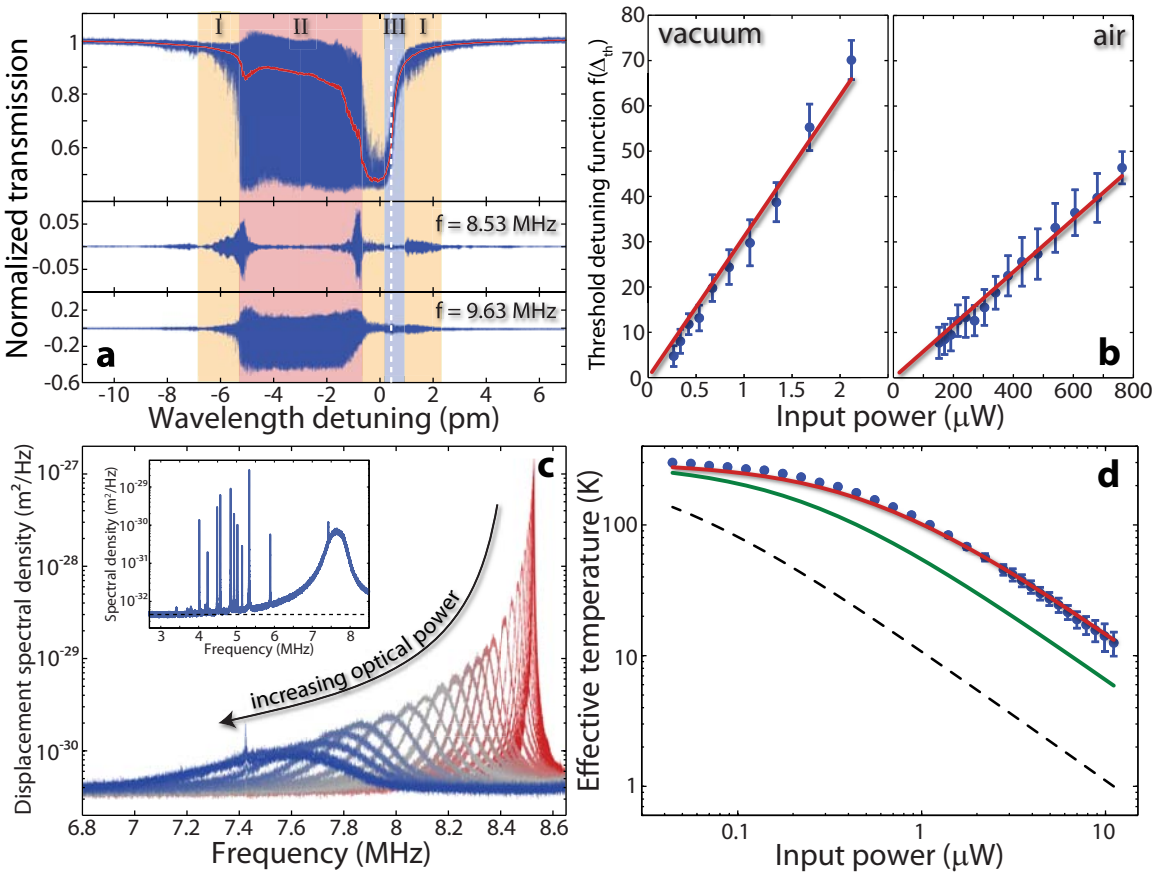

Figure 2.8: (a) Top panel: Normalized cavity transmission for Sample II in vacuum and $P_i = 11$ μW. Blue and red traces show the instantaneous and low-pass-filtered signals, respectively. Middle panel: the transduction amplitude of the frequency component at 8.53 MHz and its higher-order harmonics. Bottom panel: the transduction amplitude of the frequency component at 9.63 MHz and its higher-order harmonics. (b) $f(\Delta_{\rm th})$ as a function of optical input power. Right panel: Sample I in a 1 atm. nitrogen environment. Left panel: Sample II in vacuum (inset shows the minimum achievable threshold (green arrow)). (c) Spectral intensity of the thermally-driven fundamental flapping mode at various input powers, recorded for Sample II in vacuum, with a laser detuning of $\Delta = -1.45(\kappa/2)$ (inset shows the displacement sensitivity at the highest input power with the second optical attenuator removed), and (d) the corresponding effective temperature. In (d), the red curve is a fit to the data, the solid green (dashed black) curve is a theoretical curve obtained using the estimated B-parameter from the left panel of (b) and the experimental (optimal) detuning of $\Delta = -1.45(\kappa/2)$ $\left(\Delta = -(\kappa/2)/\sqrt{5}\right)$.

panel). These modes are a mixture of the lower-lying azimuthal modes, coupled together due to deviations in circularity of the undercut region and support pedestal.

Because of the extremely short round-trip time of the cavity mode, the optical wave is sensitive only to the variations of averaged disk spacing around the whole disk. As a result, the optomechanical coupling for the fundamental flapping mode, which has a flapping amplitude uniformly distributed around the disk perimeter, is maximum, but it is nearly zero for flapping modes with higher-order azimuthal mode numbers. However, due to the asymmetry in practical devices, the net variations in the average disk spacing induced by the higher-order flapping modes (with azimuthal mode number ≥ 1) is not zero, and their thermal motion is visible in the transmission power spectrum. In general, their optomechanical coupling is weak and does not provide efficient dynamic back action.

Measurements of the optical spring effect indicates that the optical field renormalizes the cluster of modes, with the lowest-frequency mode at 8.53 MHz transforming into the fundamental flapping mode with uniformly distributed displacement along the disk perimeter (the rest of the modes decouple from the light field). With an in-vacuum $Q_M = 4070$ (Fig. 2.6(b), inset), the fundamental flapping mode has an extremely low threshold input power for regenerative oscillation. Figure 2.8(a) shows a transmission spectrum when the laser is scanned across the cavity resonance. Three different regimes can be clearly seen: (I) transduction of thermal motion, (II) onset of optically-driven oscillation, and (III) optically damped motion. The onset of regenerative oscillation coincides with a frequency shift in the fundamental flapping mode to 9.63 MHz as shown in the bottom two panels of Fig. 2.8(a). The left panel of Figure 2.8(b) shows a plot of the in-vacuum $f(\Delta_{\text{th}})$ versus input power, with a measured minimum threshold power of $P_i = 267$ nW. Extrapolation of the experimental data using Eqs. (2.55) and (2.56) to the optimal detuning point shows a minimum threshold power of only 40 nW.

2.6 Optomechanical cooling

In general, the optomechanical effect is governed by Eqs. (2.53) and (2.54). However, the optomechanical effect during mechanical cooling is well described by linear perturbation theory since the thermal mechanical motion is significantly suppressed. The intracavity field can thus be approximated as $a(t) \approx a_0(t) + \delta a(t)$, where a_0 is the cavity field in the absence of optomechanical coupling and δa is the perturbation induced by the thermal mechanical motion. From Eq. (2.53),

they are found to satisfy the following equations:

$$\frac{da_0}{dt} = (i\Delta_0 - \kappa/2)a_0 + i \quad \overline{\kappa_e} A_{in}, \tag{2.57}$$

$$\frac{d\delta a}{dt} = (i\Delta_0 - \kappa/2)\delta a - i g_{\mathrm{OM}} x a_0. \tag{2.58}$$

In the case of a continuous-wave input, Eq. (2.57) gives a steady-state value given as:

$$a_0 = \frac{i \quad \overline{\kappa_e} A_{in}}{\kappa/2 - i\Delta_0}, \tag{2.59}$$

and Eq. (2.58) provides the spectral response for the perturbed field amplitude,

$$\delta\widetilde{a}(\Omega) = \frac{i g_{\mathrm{OM}} a_0 \widetilde{x}(\Omega)}{i(\Delta_0 + \Omega) - \kappa/2}, \tag{2.60}$$

where $\delta\widetilde{a}(\Omega)$ is the Fourier transform of $\delta a(t)$ defined as $\delta\widetilde{a}(\Omega) = \int_{-\infty}^{+\infty} \delta a(t) e^{i\Omega t} dt$. Similarly, $\widetilde{x}(\Omega)$ is the Fourier transform of $x(t)$.

The optical gradient force, $F_o = -\frac{g_{\mathrm{OM}}\ a\ ^2}{\omega_0}$, is given by

$$F_o(t) = -\frac{g_{\mathrm{OM}}}{\omega_0} \left[\ a_0\ ^2 + a_0^* \delta a(t) + a_0 \delta a^*(t)\right]. \tag{2.61}$$

The first term is a static term which only affects the equilibrium position of the mechanical motion, and can be removed simply by shifting the zero-point of the mechanical displacement to the new equilibrium position. Therefore, we neglect this term in the following discussion. The second and third terms provide the dynamic optomechanical coupling. From Eq. (2.60), the gradient force is given by the following equation in the frequency domain:

$$\widetilde{F_o}(\Omega) = -\frac{2 g_{\mathrm{OM}}^2\ a_0\ ^2 \Delta_0 \widetilde{x}(\Omega)}{\omega_0} \frac{\Delta_0^2 - \Omega^2 + (\kappa/2)^2 + i\kappa\Omega}{[(\Delta_0 + \Omega)^2 + (\kappa/2)^2]\,[(\Delta_0 - \Omega)^2 + (\kappa/2)^2]}. \tag{2.62}$$

As expected, the gradient force is linearly proportional to the thermal mechanical displacement.

Equation (2.54) can be solved easily in the frequency domain, which becomes

$$(\Omega_m^2 - \Omega^2 - i\Gamma_m \Omega)\widetilde{x} = \frac{\widetilde{F_T}}{m_x} + \frac{\widetilde{F_o}}{m_x}. \tag{2.63}$$

Equation (2.63) together with (2.62) provides the simple form for the thermal mechanical displace-

ment,

$$\widetilde{x}(\Omega) = \frac{\widetilde{F_T}}{m_x} \frac{1}{(\Omega_m)^2 - \Omega^2 - i\Gamma_m \Omega}, \tag{2.64}$$

where Ω_m and Γ_m are defined as

$$\begin{aligned}
(\Omega_m)^2 &\equiv \Omega_m^2 + \frac{2g_{\mathrm{OM}}^2\, a_0\,{}^2\Delta_0}{m_x\omega_0} \frac{\Delta_0^2 - \Omega^2 + (\kappa/2)^2}{[(\Delta_0+\Omega)^2 + (\kappa/2)^2]\,[(\Delta_0-\Omega)^2 + (\kappa/2)^2]} \\
&\approx \Omega_m^2 + \frac{2g_{\mathrm{OM}}^2\, a_0\,{}^2\Delta_0}{m_x\omega_0} \frac{\Delta_0^2 - \Omega_m^2 + (\kappa/2)^2}{[(\Delta_0+\Omega_m)^2 + (\kappa/2)^2]\,[(\Delta_0-\Omega_m)^2 + (\kappa/2)^2]}, \qquad (2.65) \\
\Gamma_m &\equiv \Gamma_m - \frac{2g_{\mathrm{OM}}^2\, a_0\,{}^2\kappa\Delta_0}{m_x\omega_0} \frac{1}{[(\Delta_0+\Omega)^2 + (\kappa/2)^2]\,[(\Delta_0-\Omega)^2 + (\kappa/2)^2]} \\
&\approx \Gamma_m - \frac{2g_{\mathrm{OM}}^2\, a_0\,{}^2\kappa\Delta_0}{m_x\omega_0} \frac{1}{[(\Delta_0+\Omega_m)^2 + (\kappa/2)^2]\,[(\Delta_0-\Omega_m)^2 + (\kappa/2)^2]}. \qquad (2.66)
\end{aligned}$$

Equations (2.64)-(2.66) show clearly that the primary effect of the optical gradient force on the mechanical motion is primarily to change its mechanical frequency (the so-called optical spring effect) and energy decay rate to the new values given by Eqs. (2.65) and (2.66). The efficiency of optomechanical control is determined by the figure of merit g_{OM}^2/m_x. On the red detuned side, the optical wave damps the thermal mechanical motion and thus increases the energy decay rate. At the same time, the mechanical frequency is modified, decreasing with increased cavity energy in the sideband-unresolved regime.

Using Eqs. (2.13) and (2.64), we find that the spectral intensity of the thermal displacement is given by a form similar to Eq. (2.14):

$$S_x(\Omega) = \frac{2\Gamma_m k_B T/m_x}{[(\Omega_m)^2 - \Omega^2]^2 + (\Omega\Gamma_m)^2}, \tag{2.67}$$

which has a maximum value $S_x(\Omega_m) = \frac{2\Gamma_m k_B T}{m_x(\Omega_m\Gamma_m)^2}$. The variance of the thermal mechanical displacement is equal to the area under the spectrum,

$$(\delta x)^2 \;= \frac{1}{2\pi}\int_{-\infty}^{+\infty} S_x(\Omega)\,d\Omega = \frac{k_B T\Gamma_m}{m_x(\Omega_m)^2\Gamma_m}. \tag{2.68}$$

Cooling the mechanical motion reduces the spectral magnitude and the variance of thermal displacement.

The large mechanical amplification of the double-disk NOMS implies a correspondingly efficient cooling of mechanical motion on the red-detuned side of the cavity resonance. As shown in Fig. 2.8(c) for Sample II in vacuum, the spectral intensity of the fundamental flapping mode de-

creases dramatically with increased input power, accompanied by a significant broadening of the mechanical linewidth. Even for the strongest damping levels, the inset to Fig. 2.8(c) shows good signal to noise for the transduced motion due to the high displacement sensitivity of the double-disk (7×10^{-17} m/Hz$^{1/2}$, as limited by the background level).

A measure of the optical cooling can be determined from the integrated area under the displacement spectrum [56]. For a mechanical mode in thermal equilibrium, the effective temperature can be inferred from the thermal mechanical energy using the equipartition theorem:

$$k_B T_{\text{eff}} = m_x (\Omega_m)^2 \ (\delta x)^2 \ . \tag{2.69}$$

The area under the displacement spectrum thus provides an accurate measure of the effective temperature. In practice, fluctuations on the laser frequency detuning may cause the mechanical frequency and damping rate to fluctuate over a certain small range [Eq. (2.65) and (2.66)], with a probability density function of $p(\Omega_m)$. As a result, the experimentally recorded displacement spectrum is given by the averaged spectrum

$$\overline{S}_x(\Omega) = \int S_x(\Omega) p(\Omega_m) d\Omega_m, \tag{2.70}$$

where $S_x(\Omega)$ is given by Eq. (2.67) and we have assumed $\int p(\Omega_m) d\Omega_m = 1$. The experimentally measured spectral area is thus

$$\frac{1}{2\pi} \int_{-\infty}^{+\infty} \overline{S}_x(\Omega) d\Omega = \int \ (\delta x)^2 \ p(\Omega_m) d\Omega_m \equiv \overline{(\delta x)^2} \ . \tag{2.71}$$

Therefore, the integrated spectral area obtained from the experimental spectrum is the averaged variance of thermal mechanical displacement, from which, according to the equipartition theorem, we obtain the effective average temperature

$$k_B \overline{T}_{\text{eff}} = m_x (\overline{\Omega}_m)^2 \overline{(\delta x)^2} \ , \tag{2.72}$$

where $\overline{\Omega}_m \equiv \int \Omega_m p(\Omega_m) d\Omega_m$ is the center frequency of the measured displacement spectrum $\overline{S}_x(\Omega)$. Compared with the room temperature, the effective temperature is thus given by

$$\frac{\overline{T}_{\text{eff}}}{T_0} = \frac{(\overline{\Omega}_m)^2 \overline{(\delta x)^2}}{\overline{\Omega}_m^2 \ (\delta x)^2 \ _0}, \tag{2.73}$$

where $(\delta x)^2_{\ 0}$ is the displacement variance at room temperature, given by the spectral area at T_0.

Figure 2.8(d) plots the inferred temperaure, $T_{\rm eff}$, which drops down to 12.5 K for a maximum input power of $P_i = 11$ μW ($P_d = 4.4$ μW). In principle, the effective temperature is related to the optical damping rate ($\Gamma_{m,\rm opt}$) through the relation $T_0/T_{\rm eff} = 1+\Gamma_m/\Gamma_{m,\rm opt}$, where $T_0 = 300$ K is the bath temperature. In Fig. 2.8d the red curve is a fit of the measured cooling curve using the relation $T_0/T_{\rm eff} = 1+\alpha P_i$, whereas the green curve represents the expected cooling curve for the dynamic back-action parameter ($B = 0.032$ MHz/μW) determined from the threshold plot in the right panel of Fig. 2.8(b) and the experimental laser-cavity detuning ($\Delta = -1.45(\kappa/2)$). For comparison, we have also plotted (dashed black line) the theoretical cooling curve in the case of optimal laser-cavity detuning ($\Delta = -(\kappa/2)/\ \overline{5}$). The difference between the two theoretical curves and the measured data, along with the limited range of optical input power studied, can largely be attributed to issues associated with the limited bandwidth and range of our current cavity locking scheme (a problem exacerbated by the very large transduction of even the Brownian motion of the disks). As the dashed black curve indicates, technical improvements in the cavity locking position and stability should enable temperature compression factors of 20 dB for less than 1 μW of dropped power.

2.7 Discussion

The large dynamic back-action of the double-disk cavity, primarily a result of the large per-photon force and small motional mass of the structure, opens up several areas of application outside the realm of more conventional ultra-high-Q cavity geometries. This can be seen by considering not only the efficiency of the cooling/amplification process, but also the maximum rate of effective cooling/amplification, the scale of which is set by the optical cavity decay rate [57, 58]. In the double-disk cavities presented here, the dynamic back-action parameter is $B \approx 0.06$ MHz/μW for a cavity decay rate of $\kappa/2\pi \approx 100$ MHz. The combination allows for higher mechanical frequencies of operation, where the bare damping is expected to scale with frequency, and makes possible enormous temperature compression ratios. A quantum mechanical analysis of the optical self-cooling process [57, 58], indicates that the sideband resolved regime ($\kappa \lesssim \ \overline{32}\Omega_m$) is necessary to reduce the phonon occupancy below unity. Having already achieved optical Q-factors in excess of 10^6, and planar silica microdisks having already been demonstrated with $Q > 10^7$ [59], we expect that further optimization of the double-disk NOMS will be able to extend its operation well into the sideband resolved regime. The combination of large dynamic back-action parameter and large maximum

amplification rate also present intriguing possibilites for sensitive, high temporal resolution force detection [60], particularly in heavily damped environments such as fluids for biological applications [46, 47]. Other application areas enabled by the chip-scale format of these devices include tunable photonics [42–44], optical wavelength conversion [61], and RF-over-optical communication.

Chapter 3

Coherent Mechanical Mode Mixing in Optomechanical Nanocavities

3.1 Introduction

The coherent mixing of multiple excitation pathways provides the underlying mechanism for many physical phenomena. Well-known examples include the Fano resonance [62] and electromagnetically induced transparency (EIT) [63], arising from the interference between excitations of discrete states and/or a continuum background. In the past few decades, Fano-like or EIT-like resonances have been discovered in a variety of physical systems, such as electron transport in quantum wells/dots [64, 65], phonon interactions in solids [66, 67], inversion-free lasers [68, 69], coupled photonic microcavities [70–73], and plasmonic metamaterials [74]. Here we report a new class of coherent excitation mixing which appears in the mechanical degree of freedom of nano-optomechanical systems (NOMS). We use two canonical systems, coupled microdisks and coupled photonic-crystal nanobeams, to show that the large optical stiffening introduced by the optical gradient force actuates significant coherent mixing of mechanical excitations, not only leading to renormalization of the mechanical modes, but also producing Fano-like and EIT-like optomechanical interference, both of which are fully tunable by optical means. The demonstrated phenomena introduce the possibility for classical/quantum information processing via optomechanical systems, providing an on-chip platform for tunable optical buffering, storage, and photonic-phononic quantum state transfer. This work was initially presented in Ref. 75.

Optical forces within micromechanical systems have attracted considerable interest of late due to the demonstration of all-optical amplification and self-cooling of mesoscopic mechanical resonators [35–39]. This technique for sensing and control of mechanical motion relies on the radia-

tion pressure forces that build up in a mechanically compliant, high-Finesse optical cavity, resulting in strong dynamical back-action between the cavity field and mechanical motion. More recently [44, 45, 48, 76–78], it has been realized that guided wave nanostructures can also be used to generate extremely large per-photon optical forces via the gradient optical force [79]. The combination of tailorable mechanical geometry, small motional mass, and large per-photon force in such nanostructures results in a regime of operation in which the dynamic response of the coupled optomechanical system can significantly differ from that of the bare mechanical structure. In particular, the mechanical motion can be renormalized by the optical spring effect [29, 33, 45, 55, 80, 81], creating a highly anistropic, intensity-dependent effective elastic modulus of the optomechanical structure.

3.2 Zipper cavity and double-disk design, fabrication, and optical characterization

We have focused on two specific implementations of nanoscale cavity optomechanical systems, shown in Fig. 3.1, in which dynamical back-action effects are particularly strong. The first system consists of two patterned nanobeams in the near-field of each other, forming what has been termed a zipper cavity [45, 82]. In this cavity structure the patterning of the nanobeams localizes light through Bragg-scattering, resulting in a series of high Finesse ($\mathcal{F} \approx 3 \times 10^4$), near-infrared ($\lambda \approx 1550$ nm) optical supermodes of the beam pair. Clamping to the substrate at either end of the suspended beams results in a fundamental in-plane mechanical beam resonance of frequency ~ 8 MHz. The second cavity optomechanical system is based upon the whispering-gallery microdisk optical cavity structure presented in Chapter 2 and Ref. 48. By creating a pair of microdisks, one on top of the other with a nanoscale gap in between, strong optical gradient forces may be generated between the microdisks while maintaining the benefits of the low-loss, high-Q ($Q \geq 10^6$) character of the whispering-gallery cavity. As shown schematically in Fig. 3.1(a), the double-disk structure [48] is supported and pinned at its center, allowing the perimeter of the disks to vibrate in myriad of different ways.

The zipper cavity is formed from a thin-film (400 nm) of tensile-stressed, stoichiometric Si_3N_4 deposited by low-pressure chemical vapor deposition on a silicon substrate. Electron beam-lithography, followed by a series of plasma and wet chemical etches, are used to form the released nanobeam structure. The double-disk structure is formed from a 158 nm sacrifical amorphous silicon layer sandwiched in between two 340 nm thick silica glass layers, all of which are deposited via plasma-

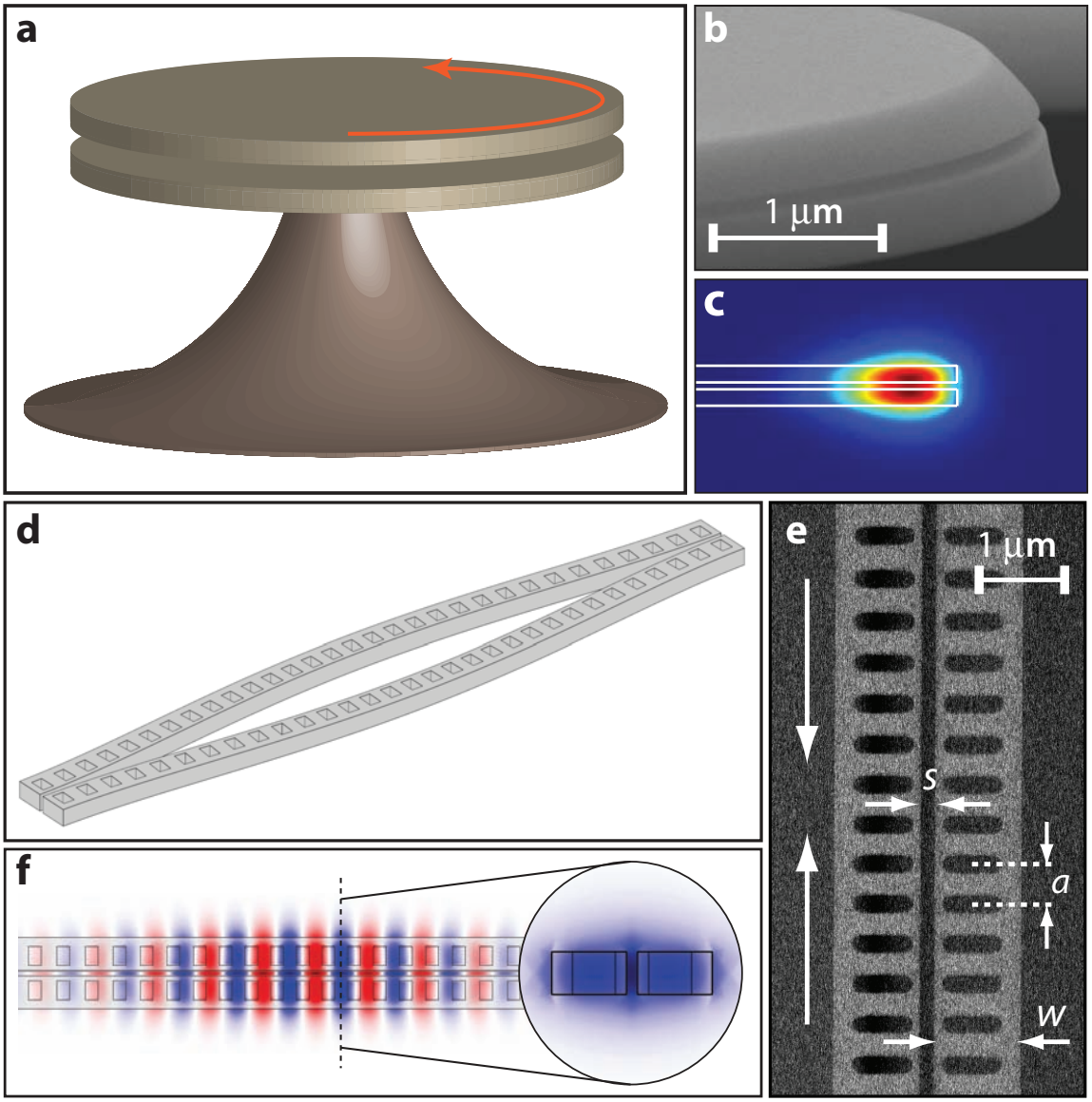

Figure 3.1: (a) Schematic and (b) zoomed-in scanning electron microscopic (SEM) image of the double-disk NOMS. (c) FEM-simulated electric field intensity of a transverse-electric (TE) polarized, bonded (even parity) whispering-gallery supermode between the two microdisks (shown in cross-section and for resonance wavelength $\lambda_c \approx 1550$ nm). The double-disk bonded supermode has an optomechanical coupling coefficient of $g_{\rm OM}/2\pi \approx 33$ GHz/nm. The device studied here has a measured resonance wavelength of $\lambda_c = 1538$ nm and an intrinsic and loaded quality (Q) factor of 1.07×10^6 and 0.7×10^6, respectively. (d) Schematic, (e) SEM image, and (f) FEM-simulated bonded (even parity) optical supermode of the zipper cavity. The zipper cavity bonded supermode has an optomechanical coupling coefficient of $g_{\rm OM}/2\pi \approx 68$ GHz/nm, a measured resonance wavelength of $\lambda_c = 1545$ nm, and an intrinsic and loaded Q-factor of 3.0×10^4 and 2.8×10^4, respectively. Additional details for both devices are in Refs. 45, 48.

enhanced chemical vapor deposition. A high temperature (1050 K) thermal anneal is used to improve the optical quality of the as-deposited silica layers. The microdisk pattern was fabricated by reactive ion etching, and the sandwiched α-Si layer was undercut by 6 μm from the disk edge using a sulfur hexafluoride dry release etch. This etch simultaneously undercuts the silicon substrate to form the underlying silicon pedestal. The final air-gap between the silica disks size is measured to be 138 nm due to shrinkage of the amorphous silicon layer during annealing.

A fiber-taper optical coupling technique is used to in-couple and out-couple light from the zipper and double-disk cavities. The fiber taper, with extremely low-loss (88% transmission efficiency), is put in contact with the substrate near the cavities in order to mechanically anchor it during all measurements (thus avoiding power-dependent movement of the taper due to thermal and/or optical forces). An optical fiber polarization controller, consisting of a series of circular loops of fiber, is used to selectively excite the transverse-electric polarized optical modes of both cavities.

RF spectra are measured by direct detection of the optical power transmitted through the cavities using a 125 MHz bandwidth photoreceiver (noise-equivalent-power NEP= 2.5 pW/Hz$^{1/2}$ from 0-10 MHz and 22.5 pW/Hz$^{1/2}$ from 10-200 MHz, responsivity $R = 1$ A/W, transimpedance gain $G = 4 \times 10^4$ V/A) and a high-speed oscilloscope (2 Gs/s sampling rate and 1 GHz bandwidth). A pair of "dueling" calibrated optical attenuators are used before and after the cavities in order to vary the input power to the cavity while keeping the detected optical power level constant. The measured electrical noise floor is set by the circuit noise of the photodetector for the optical power levels considered in this work, corresponding to -125 dBm/Hz near 10 MHz.

3.3 Theory of optomechanical effects in the presence of mode mixing

Of particular interest in both the zipper and double-disk systems are two types of motion: the differential motion of the nanobeams or disks, in which the changing gap between the elements creates a large dispersive shift in the internally propagating cavity light field; and the common motion, in which both nanobeams or disks move together, and the gap remains approximately constant, resulting in mechanical motion that is decoupled from the light field. Due to the strong light-field coupling and dynamical backaction of the differential mode, and the correspondingly weak coupling of the common mode, we term these two motional states *optically-bright* and *optically-dark*, respectively. The theory for gradient-force optomechanical systems in which there is coupling between these two types of mechanical excitations is presented in the next sections.

3.3.1 Intracavity field in the presence of optomechanical coupling

In the presence of optomechanical coupling, the optical field inside the cavity satisfies the following equation:

$$\frac{da}{dt} = (i\Delta_0 - \Gamma_t/2 - ig_{om}x_b)a + i\sqrt{\Gamma_e}A_{in}, \tag{3.1}$$

where a is the optical field of the cavity mode, normalized such that $U = |a|^2$ represents the mode energy, and A_{in} is the input optical wave, normalized such that $P_{in} = |A_{in}|^2$ represents the input power. Γ_t is the photon decay rate for the loaded cavity and Γ_e is the photon escape rate associated with the external coupling. $\Delta_0 = \omega - \omega_0$ is the frequency detuning from the input wave to the cavity resonance. g_{om} is the optomechanical coupling coefficient associated with the optically bright mode, with a mechanical displacement given by x_b. In Eq. (3.1), we have neglected the optomechanical coupling to the optically dark mode because of its negligible magnitude.

Well below the threshold of mechanical oscillation, the mechanical motion is generally small, and its impact on the intracavity optical field can be treated as a small perturbation. As a result, the intracavity field can be written as $a(t) \approx a_0(t) + \delta a(t)$, where a_0 is the cavity field in the absence of optomechanical coupling and δa is the perturbation induced by the mechanical motion. They satisfy the following two equations:

$$\frac{da_0}{dt} = (i\Delta_0 - \Gamma_t/2)a_0 + i\sqrt{\Gamma_e}A_{in}, \tag{3.2}$$

$$\frac{d\delta a}{dt} = (i\Delta_0 - \Gamma_t/2)\delta a - ig_{om}x_b a_0. \tag{3.3}$$

In the case of a continuous-wave input, Eq. (3.2) leads to a steady state given by

$$a_0 = \frac{i\sqrt{\Gamma_e}A_{in}}{\Gamma_t/2 - i\Delta_0}, \tag{3.4}$$

and Eq. (3.3) provides a spectral response for the perturbed field amplitude of

$$\delta\widetilde{a}(\Omega) = \frac{ig_{om}a_0\widetilde{x}_b(\Omega)}{i(\Delta_0 + \Omega) - \Gamma_t/2}, \tag{3.5}$$

where $\delta\widetilde{a}(\Omega)$ is the Fourier transform of $\delta a(t)$ defined as $\delta\widetilde{a}(\Omega) = \int_{-\infty}^{+\infty} \delta a(t)e^{i\Omega t}dt$. Similarly, $\widetilde{x}_b(\Omega)$ is the Fourier transform of $x_b(t)$.

3.3.2 The power spectral density of the cavity transmission

From the discussion in the previous section, the transmitted optical power from the cavity is given by

$$P_T = \left| A_{in} + i\sqrt{\Gamma_e}a \right|^2 \approx \ A_0\ ^2 + i\sqrt{\Gamma_e}\,(A_0^*\delta a - A_0\delta a^*)\,, \tag{3.6}$$

where A_0 is the steady-state cavity transmission in the absence of optomechanical coupling. It is given by

$$A_0 = A_{in}\frac{(\Gamma_0-\Gamma_e)/2 - i\Delta_0}{\Gamma_t/2 - i\Delta_0}, \tag{3.7}$$

where Γ_0 is the photon decay rate of the intrinsic cavity. It is easy to show that the averaged cavity transmission is given by $P_T\ = \ A_0\ ^2$, as expected. By using Eqs. (3.5), (3.6), and (3.7), we find the power fluctuations, $\delta P_T(t) \equiv P_T(t) - \ P_T\ $, are given in the frequency domain by

$$\delta\widetilde{P}_T(\Omega) = \frac{i\Gamma_e P_{in} g_{om}\widetilde{x}_b(\Omega)}{(\Gamma_t/2)^2+\Delta_0^2}\left[\frac{(\Gamma_0-\Gamma_e)/2 + i\Delta_0}{\Gamma_t/2 - i(\Delta_0+\Omega)} - \frac{(\Gamma_0-\Gamma_e)/2 - i\Delta_0}{\Gamma_t/2 + i(\Delta_0-\Omega)}\right], \tag{3.8}$$

where $\delta\widetilde{P}_T(\Omega)$ is the Fourier transform of $\delta P_T(t)$. By using Eq. (3.8), we obtain a power spectral density (PSD) for the cavity transmission of

$$S_P(\Omega) = g_{om}^2 P_{in}^2 S_{x_b}(\Omega) H(\Omega), \tag{3.9}$$

where $S_{x_b}(\Omega)$ is the spectral intensity of the mechanical displacement for the optically bright mode which will be discussed in detail in the following sections. $H(\Omega)$ is the cavity transfer function defined as

$$H(\Omega) \equiv \frac{\Gamma_e^2}{\left[\Delta_0^2 + (\Gamma_t/2)^2\right]^2}\frac{4\Delta_0^2(\Gamma_0^2+\Omega^2)}{[(\Delta_0+\Omega)^2+(\Gamma_t/2)^2]\,[(\Delta_0-\Omega)^2+(\Gamma_t/2)^2]}. \tag{3.10}$$

In general, when compared with $S_{x_b}(\Omega)$, $H(\Omega)$ is a slowly varying function of Ω and can be well approximated by its value at the mechanical resonance: $H(\Omega) \approx H(\Omega_{mb})$. Clearly then, the power spectral density of the cavity transmission is linearly proportional to the spectral intensity of the mechanical displacement of the optically bright mode.

3.3.3 The mechanical response with multiple excitation pathways

When the optically bright mode is coupled to an optically dark mode, the Hamiltonian for the coupled mechanical system is given by the general form:

$$\mathcal{H}_m = \frac{p_b^2}{2m_b} + \frac{1}{2}k_b x_b^2 + \frac{p_d^2}{2m_d} + \frac{1}{2}k_d x_d^2 + \kappa x_b x_d, \tag{3.11}$$

where x_j, p_j, k_j, and m_j ($j = b, d$) are the mechanical displacement, kinetic momentum, the spring constant, and the effective motional mass for the j^{th} mechanical mode, respectively, and κ represents the mechanical coupling between the bright and dark modes. The subscripts b and d denote the optically bright and optically dark modes, respectively. With this system Hamiltonian, including the optical gradient force on the optically bright mode and counting in the mechanical dissipation induced by the thermal mechanical reservoir, we obtain the equations of motion for the two mechanical modes:

$$\frac{d^2x_b}{dt^2} + \Gamma_{mb}\frac{dx_b}{dt} + \Omega_{mb}^2 x_b + \frac{\kappa}{m_b}x_d = \frac{F_b}{m_b} + \frac{F_o}{m_b}, \tag{3.12}$$

$$\frac{d^2x_d}{dt^2} + \Gamma_{md}\frac{dx_d}{dt} + \Omega_{md}^2 x_d + \frac{\kappa}{m_d}x_b = \frac{F_d}{m_d}, \tag{3.13}$$

where $\Omega_{mj}^2 \equiv \frac{k_j}{m_j}$ is the mechanical frequency for the j^{th} mode. F_j ($j = b, d$) represents the Langevin forces from the thermal reservoir actuating the Brownian motion, with the following statistical properties in the frequency domain:

$$\widetilde{F}_i(\Omega_u)\widetilde{F}_j^*(\Omega_v) \;\; = 2m_i\Gamma_{mi}k_BT\delta_{ij}2\pi\delta(\Omega_u - \Omega_v), \tag{3.14}$$

where $i, j = b, d$, T is the temperature and k_B is the Boltzmann constant. $\widetilde{F}_i(\Omega)$ is the Fourier transform of $F_i(t)$.

In Eq. (3.12), $F_o = -\frac{g_{om}\,a\,^2}{\omega_0}$ represents the optical gradient force. From the previous section, we find that it is given by

$$F_o(t) = -\frac{g_{om}}{\omega_0}\left[\, a_0\,^2 + a_0^*\delta a(t) + a_0\delta a^*(t)\right]. \tag{3.15}$$

The first term is a static term which only changes the equilibrium position of the mechanical motion. It can be removed simply by shifting the mechanical displacement to be centered at the new equilibrium position. Therefore, we neglect this term in the following discussion. The second and

third terms provide the dynamic optomechanical coupling. From Eq. (3.5), the gradient force is found to be given in the frequency domain by

$$\widetilde{F}_o(\Omega) \equiv f_o(\Omega)\widetilde{x}_b(\Omega) = -\frac{2g_{om}^2\, a_0\,{}^2\Delta_0\widetilde{x}_b(\Omega)}{\omega_0}\frac{\Delta_0^2-\Omega^2+(\Gamma_t/2)^2+i\Gamma_t\Omega}{[(\Delta_0+\Omega)^2+(\Gamma_t/2)^2]\,[(\Delta_0-\Omega)^2+(\Gamma_t/2)^2]}, \quad (3.16)$$

which is linearly proportional to the mechanical displacement of the optically bright mode.

Equations (3.12) and (3.13) can be solved easily in the frequency domain, in which the two equations become

$$L_b(\Omega)\widetilde{x}_b + \frac{\kappa}{m_b}\widetilde{x}_d = \frac{\widetilde{F}_b}{m_b} + \frac{\widetilde{F}_o}{m_b}, \quad (3.17)$$

$$L_d(\Omega)\widetilde{x}_d + \frac{\kappa}{m_d}\widetilde{x}_b = \frac{\widetilde{F}_d}{m_d}, \quad (3.18)$$

where $L_j(\Omega) \equiv \Omega_{mj}^2 - \Omega^2 - i\Gamma_{mj}\Omega$ ($j = b,d$). Substituting Eq. (3.16) into Eq. (3.17), we find that Eq. (3.17) can be written in the simple form,

$$L_b(\Omega)\widetilde{x}_b + \frac{\kappa}{m_b}\widetilde{x}_d = \frac{\widetilde{F}_b}{m_b}, \quad (3.19)$$

where $L_b(\Omega)$ is now defined with a new mechanical frequency Ω_{mb} and energy decay rate Γ_{mb} as

$$L_b(\Omega) = \Omega_{mb}^2 - \Omega^2 - i\Gamma_{mb}\Omega - \frac{f_o(\Omega)}{m_b} \equiv (\Omega_{mb})^2 - \Omega^2 - i\Gamma_{mb}\Omega, \quad (3.20)$$

and the new Ω_{mS} and Γ_{mS} are given by

$$\begin{aligned}(\Omega_{mb})^2 &\equiv \Omega_{mb}^2 + \frac{2g_{om}^2\, a_0\,{}^2\Delta_0}{m_b\omega_0}\frac{\Delta_0^2-\Omega^2+(\Gamma_t/2)^2}{[(\Delta_0+\Omega)^2+(\Gamma_t/2)^2]\,[(\Delta_0-\Omega)^2+(\Gamma_t/2)^2]} \\ &\approx \Omega_{mb}^2 + \frac{2g_{om}^2\, a_0\,{}^2\Delta_0}{m_b\omega_0}\frac{\Delta_0^2-\Omega_{mb}^2+(\Gamma_t/2)^2}{[(\Delta_0+\Omega_{mb})^2+(\Gamma_t/2)^2]\,[(\Delta_0-\Omega_{mb})^2+(\Gamma_t/2)^2]}, \quad (3.21)\\ \Gamma_{mb} &\equiv \Gamma_{mb} - \frac{2g_{om}^2\, a_0\,{}^2\Gamma_t\Delta_0}{m_b\omega_0}\frac{1}{[(\Delta_0+\Omega)^2+(\Gamma_t/2)^2]\,[(\Delta_0-\Omega)^2+(\Gamma_t/2)^2]} \\ &\approx \Gamma_{mb} - \frac{2g_{om}^2\, a_0\,{}^2\Gamma_t\Delta_0}{m_b\omega_0}\frac{1}{[(\Delta_0+\Omega_{mb})^2+(\Gamma_t/2)^2]\,[(\Delta_0-\Omega_{mb})^2+(\Gamma_t/2)^2]}. \quad (3.22)\end{aligned}$$

Clearly, the effect of the optical gradient force on the optically bright mode is primarily to change its mechanical frequency (the optical spring effect) and energy decay rate (mechanical amplification or damping).

Equations (3.18) and (3.19) can be solved easily to obtain the solution for the optically bright mode,

$$\widetilde{x}_b(\Omega) = \frac{\frac{\widetilde{F}_b(\Omega)}{m_b} L_d(\Omega) - \frac{\kappa}{m_b}\frac{\widetilde{F}_d(\Omega)}{m_d}}{L_b(\Omega)L_d(\Omega) - \eta^4}, \tag{3.23}$$

where $\eta^4 \equiv \frac{\kappa^2}{m_b m_d}$ represents the mechanical coupling coefficient. By using Eq. (3.14) and (3.23), we obtain the spectral intensity of the mechanical displacement for the optically bright mode,

$$S_{x_b}(\Omega) = \frac{2k_B T}{m_b} \frac{\eta^4 \Gamma_{md} + \Gamma_{mb}\ L_d(\Omega)^{\ 2}}{L_b(\Omega)L_d(\Omega) - \eta^{4\ 2}}, \tag{3.24}$$

where $L_b(\Omega)$ is given by Eq. (3.20). The mechanical response given by Eq. (3.24) is very similar to the atomic response in EIT.

3.3.4 The mechanical response with external optical excitation

The previous section focuses on the case in which the mechanical excitations are primarily introduced by the thermal perturbations from the environmental reservoir. However, the mechanical motion can be excited more intensely through the optical force by modulating the incident optical wave. In this case, the input optical wave is composed of an intense CW beam together with a small modulation: $A_{in} = A_{in0} + \delta A(t)$. As a result, Eq. (3.3) now becomes

$$\frac{d\delta a}{dt} = (i\Delta_0 - \Gamma_t/2)\delta a - i g_{om} x_b a_0 + i\sqrt{\Gamma_e}\delta A. \tag{3.25}$$

This equation leads to the intracavity field modulation given in the frequency domain as:

$$\delta\widetilde{a}(\Omega) = \frac{i g_{om} a_0 \widetilde{x}_b(\Omega) - i\ \ \sqrt{\Gamma_e}\delta\widetilde{A}(\Omega)}{i(\Delta_0 + \Omega) - \Gamma_t/2}, \tag{3.26}$$

where $\delta\widetilde{A}(\Omega)$ is the Fourier transform of $\delta A(t)$. By use of this solution together with Eq. (3.15), the gradient force now becomes

$$\widetilde{F}_o(\Omega) = f_o(\Omega)\widetilde{x}_b(\Omega) + \widetilde{F}_e(\Omega), \tag{3.27}$$

where $f_o(\Omega)$ is given by Eq. (3.16) and $\widetilde{F}_e(\Omega)$ represents the force component introduced by the input modulation. It is given by the following form:

$$\widetilde{F}_e(\Omega) = \frac{i\ \ \sqrt{\Gamma_e} g_{om}}{\omega_0}\left[\frac{a_0^* \delta\widetilde{A}(\Omega)}{i(\Delta+\Omega) - \Gamma_t/2} + \frac{a_0 \delta\widetilde{A}^*(-\Omega)}{i(\Delta-\Omega) + \Gamma_t/2}\right]. \tag{3.28}$$

In particular, in the sideband-unresolved regime, Eq. (3.28) can be well approximated by

$$\widetilde{F}_e(\Omega) \approx \frac{i \sqrt{\Gamma_e} g_{om}}{\omega_0 (i\Delta - \Gamma_t/2)} \left[a_0^* \delta\widetilde{A}(\Omega) + a_0 \delta\widetilde{A}^*(-\Omega) \right]. \tag{3.29}$$

In the case that the mechanical excitation is dominated by the external optical modulation, the thermal excitation from the reservoir is negligible and Eqs. (3.12) and (3.13) become

$$\frac{d^2 x_b}{dt^2} + \Gamma_{mb} \frac{dx_b}{dt} + \Omega_{mb}^2 x_b + \frac{\kappa}{m_b} x_d = \frac{F_o}{m_b}, \tag{3.30}$$

$$\frac{d^2 x_d}{dt^2} + \Gamma_{md} \frac{dx_d}{dt} + \Omega_{md}^2 x_d + \frac{\kappa}{m_d} x_b = 0. \tag{3.31}$$

Using Eqs. (3.26) and (3.27), following a similar procedure as the previous section, we find that the mechanical displacement for the optically bright mode is now given by

$$\widetilde{x}_b(\Omega) = \frac{\widetilde{F}_e(\Omega)}{m_b} \frac{L_d(\Omega)}{L_b(\Omega) L_d(\Omega) - \eta^4}, \tag{3.32}$$

where $L_b(\Omega)$ and $L_d(\Omega)$ are given in the previous section. Clearly, the mechanical response given in Eq. (3.32) is directly analogous to the atomic response in EIT systems [83].

3.4 Mechanical mode renormalization in zipper cavities

We begin with an analysis of the zipper cavity, in which the strong optically-induced rigidity associated with differential in-plane motion of the nanobeams results in a dressing of the mechanical motion by the light field. Optical excitation provides both a means to transduce mechanical motion (which is imparted on the transmitted light field through phase and intensity modulation) and to apply an optical-intensity-dependent mechanical rigidity via the strong optical gradient force. By fitting a Lorentzian to the two lowest-order in-plane mechanical resonances in the radio-frequency (RF) optical transmission spectrum, we display in Fig. 3.2(a) and (b) the resonance frequency and resonance linewidth, respectively, of the two coupled mechanical modes of the nanobeam pair as a function of laser-cavity detuning. At large detuning (low intra-cavity photon number) the nanobeams' motion is transduced without inducing significant optical rigidity, and the measured mechanical resonances are split by ~ 200 kHz, with similar linewidths (damping) and transduced amplitudes (Fig. 3.2(c)). As the laser is tuned into resonance from the blue-side of the cavity, and the intra-cavity photon number increases (to ~ 7000), the higher frequency resonance is seen to

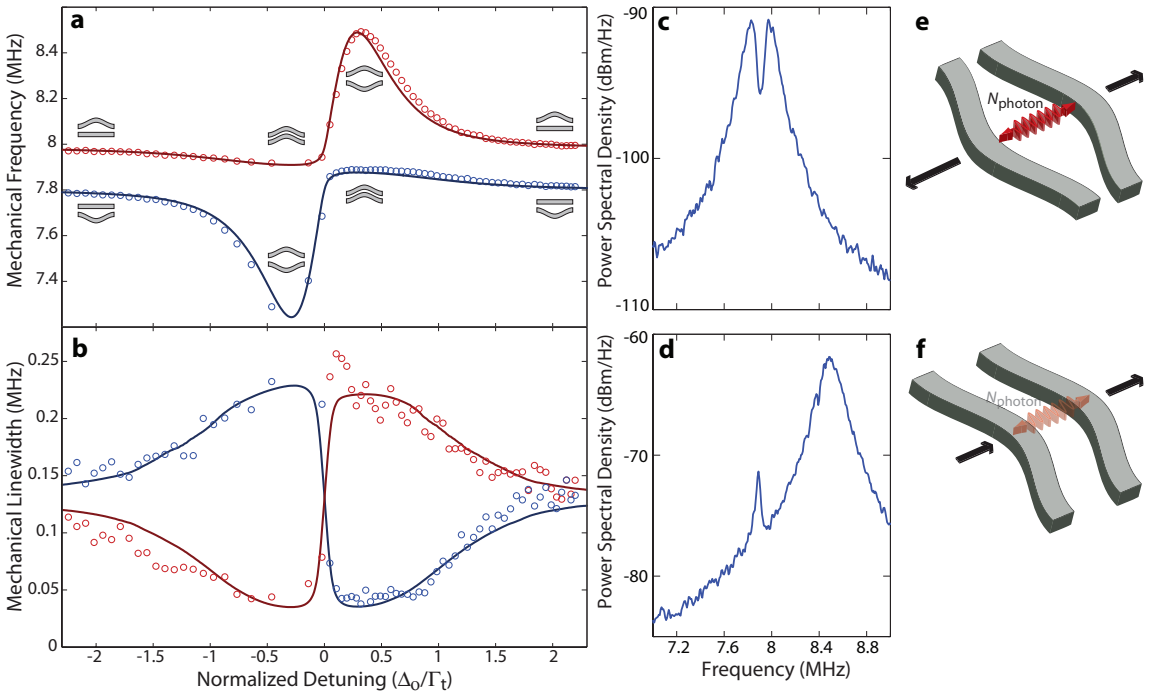

Figure 3.2: (a) Mechanical frequency and (b) linewidth of the fundamental in-plane mechanical resonances of the zipper cavity's coupled nanobeams as a function of laser frequency detuning. The input power for these measurements is 127 μW, corresponding to a maximum cavity photon number of ~ 7000 on resonance. The circles show the experimental data and the solid curves correspond to a fit to the data using Eq. (3.37). Optically-transduced RF spectrum at a laser-cavity detuning of (c) $\Delta_0/\Gamma_t = 2.1$ and (d) $\Delta_0/\Gamma_t = 0.32$. The two nanobeams vibrate independently when the laser-cavity detuning is large, but are renormalized to the cooperative (e) differential and (f) common motions near resonance.

significantly increase in frequency while the lower frequency mode tunes to the average of the independent beam frequencies with its transduced amplitude significantly weaker. The linewidth of the high frequency resonance also tends to increase, while that of the lower frequency mode drops. Tuning from the red-side of the cavity resonance reverses the sign of the frequency shifts and the roles of the high and low frequency modes.

A qualitative understanding of the light-induced tuning and damping of the zipper cavity nanobeam motion emerges if one considers the effects of squeeze-film damping [84]. Squeeze-film effects, a result of trapped gas in-between the beams (measurements were performed in 1 atm. of nitrogen), tend to strongly dampen differential motion of the beams and should be negligible for common motion of the beams. Similarly, the optical gradient force acts most strongly on the differential beam motion and negligibly on the common-mode motion. The sign of the resulting optical spring is positive for blue detuning and negative for red detuning from the cavity resonance. Putting all of this

together, a consistent picture emerges from the data in Fig. 3.2 in which the nanobeams start out at large detuning moving independently with similar damping (the frequency splitting of ~ 200 kHz is attributable to fabrication assymetries in the beams). As the detuning is reduced, and approaches the cavity half-linewidth, the motion of the nanobeams is dressed by the internal cavity field into differential motion with a large additional optical spring constant (either positive or negative) and large squeeze-film damping component, and common motion with reduced squeeze-film damping and minimal coupling to the light field. Due to the strong light-field coupling of the differential mode and the correspondingly weak coupling of the common mode, we term these dressed motional states *optically-bright* and *optically-dark*, respectively.

In general, the motion of individual disks or nanobeams satisfies the following equations:

$$\frac{d^2x_1}{dt^2}+\Gamma_{m1}\frac{dx_1}{dt}+\Omega_{m1}^2x_1=\frac{F_1}{m_1}+\frac{F_o}{m_1}+\frac{F_q}{m_1}, \tag{3.33}$$

$$\frac{d^2x_2}{dt^2}+\Gamma_{m2}\frac{dx_2}{dt}+\Omega_{m2}^2x_2=\frac{F_2}{m_2}-\frac{F_o}{m_2}-\frac{F_q}{m_2}, \tag{3.34}$$

where F_q is the viscous force from the squeeze film damping, and m_j, x_j, Ω_{mj}, Γ_{mj}, F_j ($j=1,2$) are the effective mass, the mechanical displacement, resonance frequency, damping rate, and the Langevin force for individual disks (or beams), respectively.

The optically bright mechanical mode corresponds to the differential motion of the two disks/beams, with a mechanical displacement given by $x_b \equiv x_1 - x_2$. By transferring Eqs. (3.33) and (3.34) into the frequency domain, it is easy to find that the mechanical displacement of the optically bright mode is given by

$$\widetilde{x}_b(\Omega)=\frac{\widetilde{F}_1(\Omega)}{m_1L_1(\Omega)}-\frac{\widetilde{F}_2(\Omega)}{m_2L_2(\Omega)}+\left[\frac{1}{m_1L_1(\Omega)}+\frac{1}{m_2L_2(\Omega)}\right]\left[\widetilde{F}_q(\Omega)+\widetilde{F}_o(\Omega)\right], \tag{3.35}$$

where $L_j(\Omega)=\Omega_{mj}^2-\Omega^2-i\Gamma_{mj}\Omega$ ($j=1,2$). The squeeze-film effect is produced by the pressure differential between the gap and the outer region introduced by the differential mechanical motion, and thus has a magnitude linearly proportional to the differential displacement. In general, it can be described by $\widetilde{F}_q(\Omega)=f_q(\Omega)\widetilde{x}_b(\Omega)$, where $f_q(\Omega)$ represents the spectral response of the squeeze gas film [84]. Using this form together with Eq. (3.16) in Eq. (3.35), we obtain the spectral intensity of

the optically bright mode displacement,

$$S_{x_b}(\Omega) = \frac{2k_BT\left[\frac{\Gamma_{m1}}{m_1}\ L_2(\Omega)\ ^2 + \frac{\Gamma_{m2}}{m_2}\ L_1(\Omega)\ ^2\right]}{\left|L_1(\Omega)L_2(\Omega) - [f_o(\Omega)+f_q(\Omega)]\left[\frac{L_1(\Omega)}{m_2}+\frac{L_2(\Omega)}{m_1}\right]\right|^2}. \tag{3.36}$$

As the squeeze-film effect primarily damps the differential motion, its spectral response can be approximated as $f_q(\Omega) \approx i\alpha_q\Omega$. Moreover, since the two disks or nanobeams generally have only slight asymmetry due to fabrication imperfections, they generally have quite close effective masses and energy damping rates: $m_1 \approx m_2 = 2m_b$ and $\Gamma_{m1} \approx \Gamma_{m2} \equiv \Gamma_m$, where we have used the fact that the effective motional mass of the differential motion is given by $m_b = m_1m_2/(m_1+m_2)$. As a result, Eq. (3.36) can be well approximated by

$$S_{x_b}(\Omega) \approx \frac{k_BT\Gamma_m}{m_b}\frac{L_1(\Omega)\ ^2 +\ L_2(\Omega)\ ^2}{\left|L_1(\Omega)L_2(\Omega) - \frac{1}{2}\left[f_o(\Omega)/m_b + i\Gamma_q\Omega\right]\left[L_1(\Omega)+L_2(\Omega)\right]\right|^2}, \tag{3.37}$$

where $\Gamma_q \equiv \alpha_q/m_b$ represents the damping rate introduced by the squeeze gas film, and the spectral response of the gradient force $f_o(\Omega)$ is given by Eq. (3.16).

The intrinsic mechanical frequencies of 7.790 and 7.995 MHz for the two individual nanobeams are measured from the experimental recorded PSD with a large laser-cavity detuning. The optomechanical coupling coefficient is 68 GHz/nm and the effective mass is 10.75 pg for the fundamental differential mode, both obtained from FEM simulations (note that these values are different than those quoted in Ref. 45 due to the different definition of mode amplitude for x_b). The intrinsic and loaded optical Q factors are 3.0×10^4 and 2.8×10^4, respectively, obtained from optical characterization of the cavity resonance. By using these values in Eqs. (3.37) and (3.16), we can easily find the mechanical frequencies and linewidths for the two renormalized modes, where we treat the intrinsic mechanical damping rate Γ_m and the squeeze-film-induced damping rate Γ_q as fitting parameters. As shown in Fig. 3.2, this theoretical model provides an accurate description of the mechanical mode renormalization, with a fitted intrinsic mechanical and squeeze-film damping rate of 0.03 and 0.2 MHz, respectively.

Similarly, we can obtain the spectral intensity of $x_d \equiv x_1 + x_2$ for the optically-dark mechanical

mode, which is given by the following form:

$$S_{x_d}(\Omega) = 2k_BT \frac{\frac{\Gamma_{m2}}{m_2}\left|L_1(\Omega) - \frac{2}{m_1}\left[f_o(\Omega)+f_q(\Omega)\right]\right|^2 + \frac{\Gamma_{m1}}{m_1}\left|L_2(\Omega) - \frac{2}{m_2}\left[f_o(\Omega)+f_q(\Omega)\right]\right|^2}{\left|L_1(\Omega)L_2(\Omega) - \left[f_o(\Omega)+f_q(\Omega)\right]\left[\frac{L_1(\Omega)}{m_2}+\frac{L_2(\Omega)}{m_1}\right]\right|^2}. \quad (3.38)$$

Similar to the optically-bright mode, with $m_1 \approx m_2 = 2m_b$ and $\Gamma_{m1} \approx \Gamma_{m2} \equiv \Gamma_m$, Eq. (3.38) can be well approximated by

$$S_{x_d}(\Omega) \approx \frac{k_BT\Gamma_m}{m_d} \frac{L_1(\Omega) - h(\Omega)^{\,2} + L_2(\Omega) - h(\Omega)^{\,2}}{\left|L_1(\Omega)L_2(\Omega) - \frac{1}{2}h(\Omega)\left[L_1(\Omega)+L_2(\Omega)\right]\right|^2}, \quad (3.39)$$

where $m_d = m/2$ is the effective mass of the common mode and $h(\Omega) \equiv [f_o(\Omega)/m_b + i\Gamma_q\Omega]$ represents the total spectral response of the optical gradient force and squeeze film damping. In particular, when the optical-spring-induced frequency shift is much larger than the intrinsic mechanical frequency splitting, the spectral intensities of these two modes reduce to

$$S_{x_b}(\Omega) \approx \frac{2k_BT\Gamma_m/m_b}{L_o(\Omega) - h(\Omega)^{\,2}}, \qquad S_{x_d}(\Omega) \approx \frac{2k_BT\Gamma_m/m_d}{L_o(\Omega)^{\,2}} \quad (3.40)$$

where $L_0(\Omega) = (\Omega_{m1}+\Omega_{m2})^2/4 - \Omega^2 - i\Gamma_m\Omega$. Equation (3.40) indicates that the optically bright and dark modes reduce to pure differential and common modes, respectively.

3.5 Coherent mechanical mode mixing in double-disks

A similar optically-induced renormalization mechanism applies to the double-disk cavity structure shown in Fig. 3.1(a-c). In this case, the large optical spring effect for the differential motion of the two microdisks excites another, more intriguing form of coherent optomechanical mixing with the optically dark common mode of the disks. Unlike in the zipper cavity, FEM modeling of the mechanics of the double-disk structure indicates a significant frequency splitting between the differential and common modes of motion of the double disk (shown in Fig. 3.3(b) and (c)), primarily due to the difference in the extent of the undercut between the disk layers and the extent of the central pedestal which pins the two disk layers. The result is that the differential, or "flapping" motion, of the undercut disk region has a lower frequency of 7.95 MHz, whereas the common motion of the disks results in a higher frequency (14.2 MHz) "breathing" motion of the entire double-disk structure.

The RF-spectrum of the transmitted optical intensity through a double-disk cavity, measured using the same fiber probing technique as for the zipper cavity, is shown in Fig. 3.2(c) versus laser-cavity detuning. For the largest detuning (in which the optical spring is negligible) the spectrum shows a broad (2.1 MHz) resonance at 8.3 MHz and a much narrower (0.11 MHz) resonance at 13.6 MHz, in good corresponce with the expected frequencies of the flapping and breathing modes, respectively. The difference in damping between the two resonances can be attributed to the strong squeeze-film damping of the differential flapping motion of the disks. As shown in Fig. 3.2(c), the flapping mode can be tuned in frequency via the optical spring effect from its bare value of 8.3 MHz all the way out to 15.7 MHz (optical input power of $P_i = 315\ \mu$W). In the process, the flapping mode is tuned across the breathing mode at 13.6 MHz. Although the optically-dark breathing mode is barely visible in the tranduced spectrum at large laser-cavity detunings, its spectral amplitude is considerably enhanced as the optically-bright flapping mode is tuned into resonance. In addition, a strong Fano-like lineshape, with $\sim$13 dB anti-resonance, appears in the power spectrum near resonance of the two modes (Fig. 3.3(f-h)).

As shown schematically in Fig. 3.5(a), the Fano-like interference in the optically-bright power spectral density can be attributed to an internal mechanical coupling between the flapping and breathing mechanical modes. This is quite similar to the phonon-phonon interaction during the structural phase transition in solids [66, 85–89], in which the internal coupling between phonon modes produces Fano-like resonances in the Raman-scattering spectra.

The power spectral density (PSD) of the cavity transmission is linearly proportional to Eq. (3.24). Equation (3.24) together with (3.9) is used to find the theoretical PSD shown in Fig. 3.3, by using an optomechanical coupling coefficient of $g_{om}/2\pi = 33$ GHz/nm and an effective mass of $m_b = 264$ pg for the flapping mode, both obtained from FEM simulations. The intrinsic and loaded optical quality factors of 1.07×10^6 and 0.7×10^6 are obtained from optical characterization of the cavity resonance, and are also given in the caption of Fig. 3.1. The intrinsic mechanical frequencies and damping rates of the two modes (Ω_{mb}, Ω_{md}, Γ_{mb}, and Γ_{md}) are obtained from the experimentally recorded PSD of cavity transmission with a large laser-cavity detuning, as given in the caption of Fig. 3.3. The mechanical coupling coefficient η is treated as a fitting parameter. Fitting of the PSDs results in $\eta = 3.32$ MHz, indicating a strong internal coupling between the two mechanical modes. As shown clearly in Fig. 3.3(d, f-h), our theory provides an excellent description of the observed phenomena.

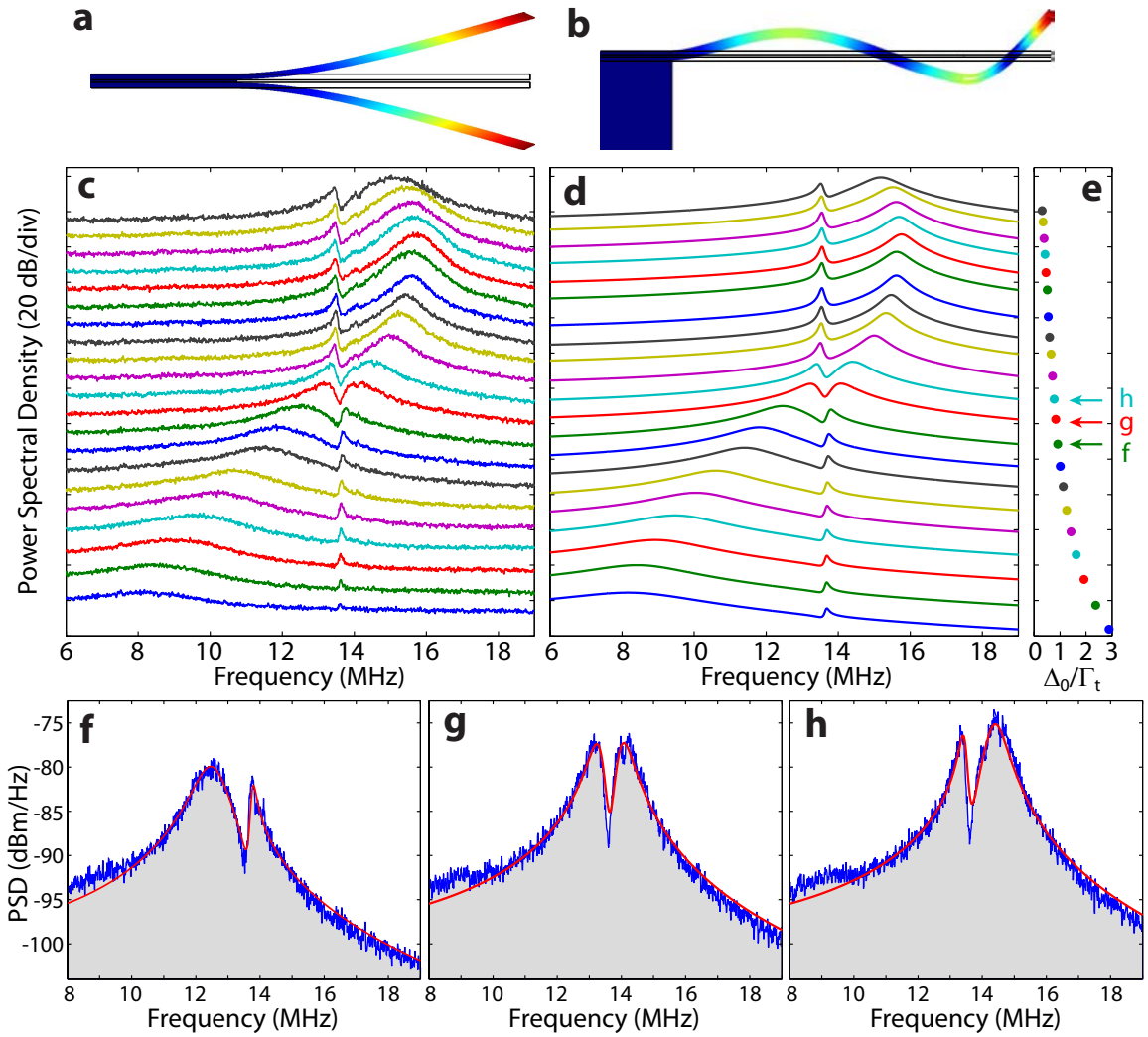

Figure 3.3: (a,b) FEM simulated mechanical motion of the differential flapping mode (a) and the common breathing mode (b), with simulated frequencies of 7.95 and 14.2 MHz. The color map indicates the relative magnitude (exaggerated) of the mechanical displacement. (c) Recorded power spectral density (PSD) of the cavity transmission for the double-disk, with an input power of 315 μW. Each curve corresponds to a normalized laser-cavity frequency detuning, Δ_0/Γ_t indicated in (e). For display purposes, each curve is relatively shifted by 10 dB in the vertical axis. (d) The corresponding theoretical PSD. (f-h) Detailed PSD at three frequency detunings indicated by the arrows in (e), with the experimental and theoretical spectra in blue and red, respectively.

3.6 Coherent mechanical mode mixing in zipper cavities

The coherent mixing of mechanical excitation is universal to gradient-force-based NOMS with a giant optical spring effect. Similar phenomena to that presented for double-disks were also observed in the zipper cavity. However, due to the device geometry, the coupled nanobeams have more complex mechanical mode families in which all the even-order mechanical modes are optically dark, because they exhibit a mechanical node at the beam center where the optical mode is located. As the same-order common and differential motions of the two beams have similar mechanical frequencies, they can simultaneously couple to the same optically bright mode, leading to multiple excitation interferences on the mechanical response.

In the case when the optically bright mode is coupled to two optically dark modes, the Hamiltonian for the mechanical system is given by the following general form:

$$\mathcal{H}_m = \sum_{i=b,1,2} \left(\frac{p_i^2}{2m_i} + \frac{1}{2} k_i x_i^2 \right) + \kappa_1 x_b x_1 + \kappa_2 x_b x_2, \tag{3.41}$$

where $i = b, 1, 2$ corresponds to the optically bright mode and optically dark modes 1 and 2, respectively. With this Hamiltonian, counting in both the optical gradient force and the Langevin forces from the thermal reservoir, we obtain the equations of motions for the three modes:

$$\frac{d^2 x_b}{dt^2} + \Gamma_{mb} \frac{dx_b}{dt} + \Omega_{mb}^2 x_b + \frac{\kappa_1}{m_b} x_1 + \frac{\kappa_2}{m_b} x_2 = \frac{F_b}{m_b} + \frac{F_o}{m_b}, \tag{3.42}$$

$$\frac{d^2 x_1}{dt^2} + \Gamma_{m1} \frac{dx_1}{dt} + \Omega_{m1}^2 x_2 + \frac{\kappa_1}{m_1} x_b = \frac{F_1}{m_1}, \tag{3.43}$$

$$\frac{d^2 x_2}{dt^2} + \Gamma_{m2} \frac{dx_2}{dt} + \Omega_{m2}^2 x_3 + \frac{\kappa_2}{m_2} x_b = \frac{F_2}{m_2}, \tag{3.44}$$

where the gradient force F_o is given by Eq. (3.15), and the statistical properties of the Langevin forces are given by Eq. (3.14). Following the same analysis as in Section 3.3.3, we can obtain the spectral intensity for the mechanical displacement of the optically bright mode as

$$S_{x_b}(\Omega) = \frac{2k_B T}{m_b} \frac{\eta_1^4 \Gamma_{m1} \ L_2(\Omega)\ ^2 + \eta_2^4 \Gamma_{m2} \ L_1(\Omega)\ ^2 + \Gamma_{mb} \ L_1(\Omega) L_2(\Omega)\ ^2}{\left| L_b(\Omega) L_1(\Omega) L_2(\Omega) - \eta_1^4 L_2(\Omega) - \eta_2^4 L_1(\Omega) \right|^2}, \tag{3.45}$$

where $\eta_j^4 \equiv \frac{\kappa_j^2}{m_b m_j}$ $(j = 1, 2)$ represents the mechanical coupling coefficient. $L_j(\Omega) = \Omega_{mj}^2 - \Omega^2 - i\Gamma_{mj}\Omega$ $(j = 1, 2)$ and $L_b(\Omega)$ is given by Eq. (3.20) with Ω_{mb} and Γ_{mb} given in Eqs. (3.21) and (3.22), respectively. As the optical wave is coupled to the optically bright mode only, the power spectral

density of the cavity transmission is still given by Eq. (3.9), with the mechanical response S_{x_b} given in Eq. (3.45).

Figure 3.4 shows the PSD of the cavity transmission by launching a continuous wave into a resonance of the coupled nanobeams with an intrinsic and loaded Q factor of 3.0×10^4 and 2.8×10^4, respectively. Three mechanical modes are clearly visible, where mode I is the fundamental differential mode [Fig. 3.4(h)I], and mode II and III correspond to the second-order common and differential modes [Fig. 3.4(h)II and III], respectively. Similar to the double-disk NOMS, the gigantic optical spring effect shifts the frequency of the optically bright mode I from its intrinsic value of 8.06 MHz to 19 MHz, crossing over both optically dark modes II and III closely located at 16.54 and 17.04 MHz and resulting in complex interferences on the power spectra [Fig. 3.4(a)]. Equation (3.45) provides an accurate description of the observed phenomena, as shown clearly in Fig. 3.4(b), (d)-(f). Fitting of the PSD results in mechanical coupling coefficients of $\eta_1 = 3.45$ MHz and $\eta_2 = 3.48$ MHz, implying that the two optically dark modes couple to the fundamental optically bright mode with a similar magnitude.

3.7 Analogy to electromagnetically-induced transparency

The mechanical response given by Eq. (3.24) is directly analogous to the atomic response in EIT [83]. Just as in EIT, one can understand the resulting Fano lineshape in two different ways. The first perspective considers the interference associated with multiple excitation pathways. In the optomechanical system, the mechanical motion of the flapping mode is thermally excited along two different pathways, either directly into the broadband (lossy) flapping mode, or indirectly, through the flapping mode, into the long-lived breathing mode, and then back again into the flapping mode. The two excitation pathways interfere with each other, resulting in the Fano-like resonance in the spectral response of the optically bright flapping mode. An alternative, but perfectly equivalent view of the coupled optomechanical system considers the dressed states resulting from the internal mechanical coupling. In this picture the internal mechanical coupling renormalizes the broadband flapping mode and the narrowband breathing mode into two dressed mechanical modes, both broadband and optically-bright. In particular, when the flapping and breathing mechanical frequencies coincide, the two dressed modes are excited with equal amplitude and opposite phase at the center frequency between the split dressed states. Destructive interference results, suppressing excitation of the mechanical system at the line center. Consequently, the mechanical motion becomes purely a trapped

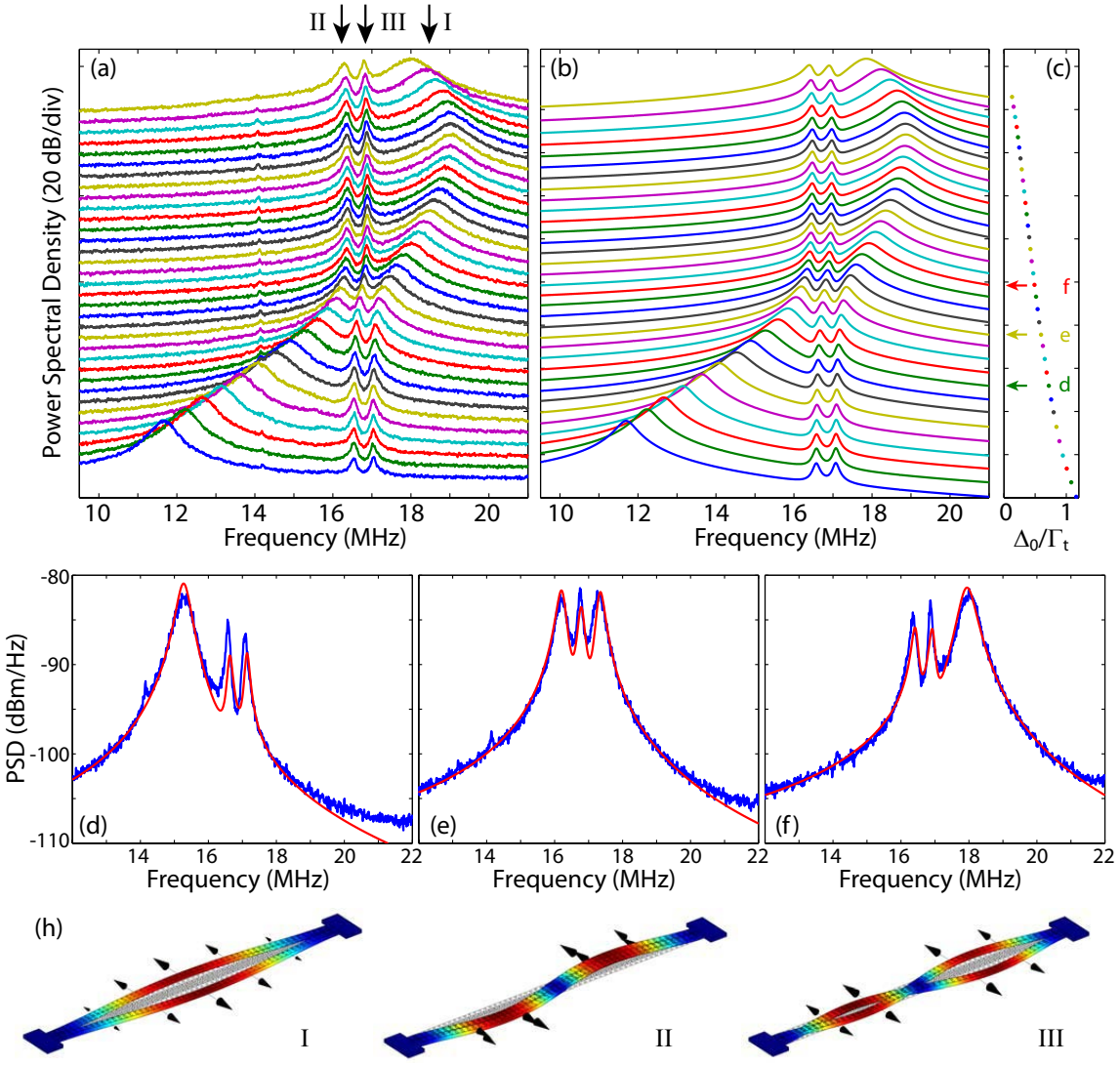

Figure 3.4: (a) Experimentally recorded power spectral densities of the cavity transmission for the zipper cavity of Fig. 3.1(d-f), with an input power of 5.1 mW. Each curve corresponds to a laser frequency detuning indicated in (c). Each curve is relatively shifted by 5 dB in the vertical axis for a better vision of the mechanical frequency tuning and the induced mechanical interference. The optically dark mode II and III have a full-width at half maximum (FWHM) of 0.16 and 0.15 MHz, respectively. The optically bright mode I has an intrinsic FWHM of 0.30 MHz. (b) The corresponding theoretical spectra of the power spectral density. (d)-(f) The detailed spectra of the power spectral density at three frequency detunings indicated by the three arrows in (c). The blue and red curves show the experimental and theoretical spectra, respectively. (h) FEM simulated mechanical motions for the fundamental *differential* mode (I), the second-order *common* (II) and *differential* (III) modes, whose frequencies are indicated by the arrows in (a). The color map indicates the relative magnitude (exaggerated) of the mechanical displacement.

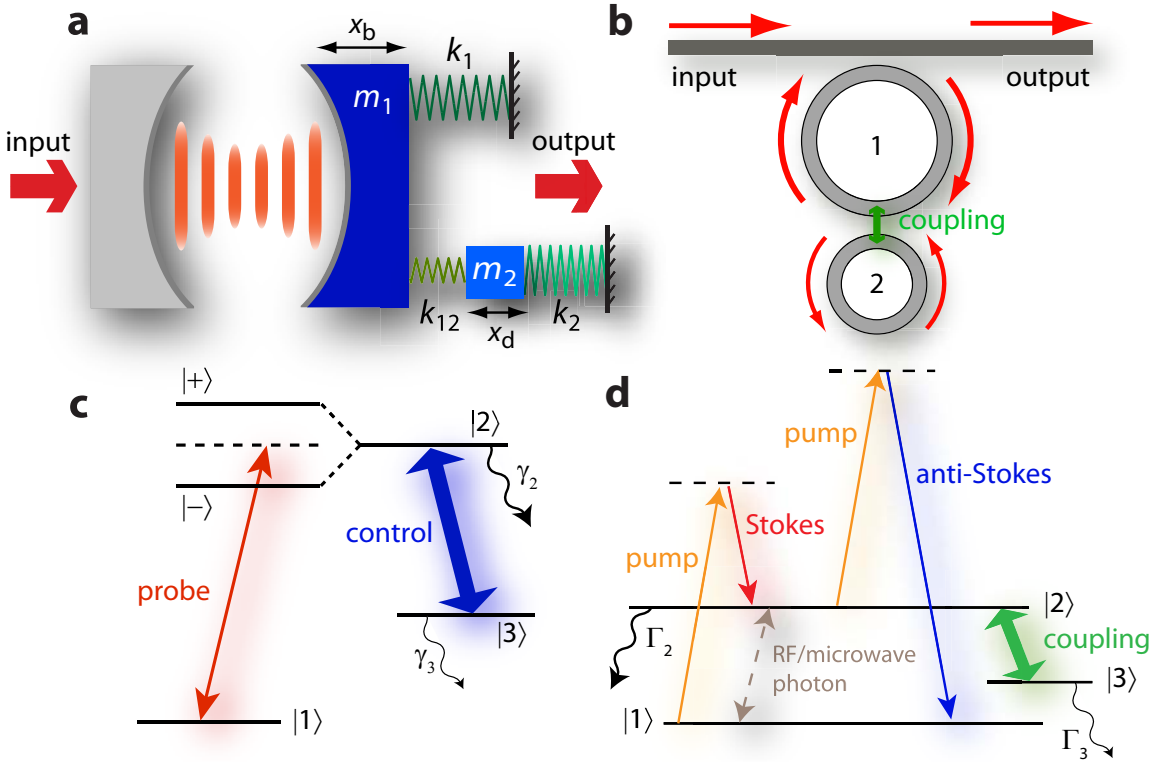

Figure 3.5: (a) Schematic of an equivalent Fabry-Perot cavity system showing mechanical mode mixing. The mechanical motion of the cavity mirror (m_1, equivalent to the optically-bright flapping mode) is primarily actuated by the spring k_1 and the optical force. It is internally coupled to a second mass-spring system (m_2, equivalent to the breathing mode) actuated by the spring k_2 which is decoupled from the optical wave. The two masses are internally coupled via spring k_{12}. (b) A photonic analogue to the optomechanical system involving coupled resonators. Microcavity 1 is directly coupled to the external optical waveguide (equivalent to the optically-bright flapping mode) and also internally coupled the narrowband cavity 2 (equivalent to the optically-dark breathing mode). (c) State diagram of an EIT-like medium. The excited state (2) is split by the optical control beam into two broadband dressed states ($+$ and $-$). The dipole transition between ground-states 1 and 3 is forbidden. (d) The state diagram corresponding to the optomechanical system of (a) where 1 is the phonon vacuum state, and 2 and 3 correspond to the flapping and breathing modes, respectively.

mechanically-dark state, transparent to external excitation. As shown in Fig. 3.3(c), this induced mechanical transparency is a direct analogue to EIT in atomic systems [63, 83, 90, 91], in which the quantum interference between the transition pathways to the dressed states of the excited electronic state, through either $1 \quad +$ or $1 \quad -$, leads to an induced spectral window of optical transparency.

Despite the intriguing similarities between the optomechanical system studied here and EIT in atomic media, there are some important, subtle differences. For instance, in the optomechanical system, rather than the linear dipole transition of EIT, the interaction corresponds to a second-order transition. The dynamic backaction between the cavity field and mechanical motion creates Stokes and anti-Stokes optical sidebands, whose beating with the fundamental optical wave resonates with the mechanical motion to create/annihilate phonons (see Fig. 3.3(d)). Functionally, this is like coherent Stokes and anti-Stokes Raman scattering, albeit with unbalanced scattering amplitudes resulting from the coloring of the electromagnetic density of states by the optical cavity.

The system Hamiltonian of an optomechanical cavity is given by the following general form:

$$\mathcal{H} = \hbar\omega_0 a^\dagger a + \hbar\Omega_m b^\dagger b + \hbar g_{om} x_b a^\dagger a, \tag{3.46}$$

where a and b are the annihilation operators for photon and phonon, respectively, normalized such that $a^\dagger a$ and $b^\dagger b$ represent the operators for photon and phonon number. x_b is the mechanical displacement for the optically bright mode, related to b by

$$x_b = \sqrt{\frac{\hbar}{2m_b\Omega_{mb}}}\left(b + b^\dagger\right). \tag{3.47}$$

Therefore, the interaction Hamiltonian between the optical wave and the mechanical motion is given by

$$\mathcal{H}_i = hga^\dagger a\left(b + b^\dagger\right), \tag{3.48}$$

where the factor $g \equiv \left(\frac{g_{om}^2\hbar^3}{2m_b\Omega_{mb}}\right)^{1/2}$.

The mechanical motion modulates the intracavity field to create two optical sidebands. As a result, the optical field can be written as

$$a = a_p + a_s e^{-i\Omega_{mb}t} + a_i e^{i\Omega_{mb}t}, \tag{3.49}$$

where a_p is the field amplitude of the fundamental wave, and a_s and a_i are those of the generated Stokes and anti-Stokes wave, respectively. As the magnitudes of the Stokes and anti-Stokes sidebands are much smaller than the fundamental wave, when we substitute Eq. (3.49) into Eq. (3.48) and leave only the first-order terms of a_s and a_i, under the rotating-wave approximation, the interaction Hamiltonian becomes

$$\mathcal{H}_i = \hbar g \left(b + b^\dagger\right) a_p^\dagger a_p + \hbar g b^\dagger \left(a_s^\dagger a_p + a_p^\dagger a_i\right) + \hbar g b \left(a_p^\dagger a_s + a_i^\dagger a_p\right). \tag{3.50}$$

In Eq. (3.50), the first term describes the static mechanical actuation, which changes only the equilibrium position of mechanical motion and is neglected in the current analysis, as discussed previously. The second and third terms show clearly that the process corresponds directly to coherent Stokes and anti-Stokes Raman scattering as shown in Fig. 3.5(d).

Therefore, in analogy to EIT, it is the modulation signal carried by the incident optical wave (radio-frequency or microwave photons) that fundamentally probes/excites the mechanical motion and to which the trapped *mechanically-dark* state becomes transparent. Moreover, rather than tuning the Rabi-splitting through the intensity of a control beam resonant with the 3 2 electronic transition (Fig. 3.3(c)), this *optically-induced mechanical transparency* is controlled via optical spring tuning of the resonance frequency of the optically bright flapping mechanical mode. Perhaps the most apt analogy to the optomechanical system can be made to the photonic resonator system shown in Fig. 3.3(d). The interference in this case is between the two optical pathways composed of the waveguide-coupled low-Q optical resonator 1, and the waveguide-decoupled high-Q resonator 2. This interference again leads to a Fano-like resonance, or what has been termed coupled-resonator-induced transparency, in the optical cavity transmission [70–73].

3.8 Discussion

Although the studies considered here involve thermal excitation of the optomechanical system, the same phenomena can be excited more efficiently, and with greater control, using external optical means (Sec. 3.3.4). As such, beyond the interesting physics of these devices, exciting application in RF/microwave photonics and quantum optomechanics exist. Similar to the information storage realized through EIT [83, 92, 93], optical information can be stored and buffered in the dark mechanical degree of freedom in the demonstrated NOMS. This can be realized through a procedure

similar to that recently proposed for coupled optical resonators [94, 95] in which dynamic, adiabatic tuning of optical resonances are used to slow, store, and retrieve optical pulses. The corresponding optomechanical system would consist of an array of double-disk resonators, all coupled to a common optical bus waveguide into which an optical signal carrying RF/microwave information would be launched. In this scheme, a second control optical beam would adiabatically tune the frequency of the optically-bright flapping mode of each resonator, allowing for the RF/microwave signal to be coherently stored in (released from) the long-lived breathing mode through adiabatic compression (expansion) of the mechanical bandwidth [94, 95]. In comparison to the all-photonic system, optomechanical systems have several advantages, primarily related to the attainable lifetime of the dark mechanical state. For example, the radial breathing mechanical mode of a similar whispering-gallery cavity has been shown to exhibit a lifetime of more than 2 ms [96], a timescale more than seven orders of magnitude longer than that in demonstrated photonic-coupled-resonator systems [97] and comparable with EIT media [92, 93]. Moreover, mechanical lifetimes of more than one second have recently been demonstrated using stressed silicon nitride nanobeam [98] and nanomembrane [40] mechanical resonators operating in the MHz frequency regime. In the quantum realm, such a system operating in the good-cavity or sideband-resolved regime (by increasing either the optical Q factor [59] or the mechanical frequency), would reduce the *simultaneous* creation and annihilation of Stokes and anti-Stokes photons, enabling efficient information storage and retrieval at the single-quanta-level suitable for quantum state transfer.

Chapter 4

Mechanically Pliant Double Disk Resonators

4.1 Introduction

Optical information processing in photonic interconnects relies critically on the capability for wavelength management [99, 100]. The underlying essential functionalities are optical filtering and wavelength routing, which allow for precise selection and flexible switching of optical channels at high speeds over a broad bandwidth [99, 101–103]. In the past two decades, a variety of technologies have been developed for this purpose [104–106]; those based on micro/nano-resonators are particularly attractive because of their great potential for future on-chip integrated photonic applications [107–119]. In general, reconfigurable tuning of cavity resonances is realized through thermo-optic [109, 110, 117, 119], electro-optic [112, 118, 119], photochemical [111], optofluidic [115], or microelectricalmechanical approaches [108, 114, 120]. However, all of these tuning mechanisms have intrinsic limitations on their tuning speed [108–111, 114, 115, 117], tuning bandwidth [112, 118, 119], routing efficiency [108, 109, 118, 119], and/or routing quality [112, 118, 119]. Here we propose and demonstrate an all-optical wavelength-routing approach which combines the advantages of various approaches into one nanophotonic device. By using a tuning mechanism based upon the optical gradient forces in a specially-designed nano-optomechanical system, we are able to realize seamless wavelength routing over a range about 3000 times the channel intrinsic linewidth, with a tuning efficiency of 309 GHz/mW, a switching time of less than 200 ns, and 100% channel-quality preservation over the entire tuning range. The demonstrated approach and device geometry indicates great prospects for a variety of applications such as channel routing/switching, buffering, dispersion compensation, pulse trapping/release, and tunable lasing, with easy on-chip

integration on a silicon-compatible platform. This work was initially presented in Ref. 78.

The physics of electromagnetic forces within mechanically-compliant resonant cavities is by now well established, with some of the early experimental considerations being related to the quantum-limited measurement of weak, classical forces [29]. In the optical domain, experiments involving optical Fabry-Perot "pendulum cavities" were first explored [121], with more recent studies having measured radiation pressure forces in micro- and nano-mechanical structures [35–38, 40, 44, 45, 48, 51]. In each of these systems, whether it be gravitational wave observatory [31] or photonic crystal nanomechanical cavity [45], the same fundamental physics applies. A narrowband laser input to the system, of fixed frequency, results in a "dynamical back-action" [33] between mechanical fluctuations and the internal electromagnetic field. This dynamical back-action modifies both the real and imaginary parts of the frequency of the mechanical motion, yielding an optically-controllable, dynamic mechanical susceptibility. A separate effect occurs when the laser frequency is swept across the cavity resonance, pushing on the mechanical system as the internal light field builds up near cavity resonance. The more compliant the mechanical system, the larger the static displacement and the larger the tuning of the optical cavity. Here we utilize both the static and dynamic mechanical susceptibilities of a coupled opto-mechanical system to realize a chip-based optical filter technology in which wideband tuning and fast switching can be simultaneously accomplished.

4.2 Spiderweb resonator design and optical characterization

The optomechanical system we consider here is a simple modification to the common microring whispering-gallery cavity that has found widespread application in microphotonics. As shown in Fig. 4.1(d), it consists of a pair of planar microrings, one stacked on top of the other [122, 123]. The resulting near-field modal coupling forms a "super-cavity,", with a resonance frequency ω_0 strongly dependent on the vertical cavity spacing, x.

Fabrication of the spiderweb whispering-gallery resonator began with initial deposition of the cavity layers. The two silica web layers and the sandwiched amorphous silicon (α-Si) layer were deposited on a (100) silicon substrate by plasma-enhanced chemical vapor deposition, with a thickness of 400 ± 4 nm and 150 ± 3 nm for the silica and α-Si layers, respectively. The wafer was then thermally annealed in a nitrogen environment at a temperature of $T = 1050$ K for 10 hours to drive out water and hydrogen in the film, improving the optical quality of the material. The spider-

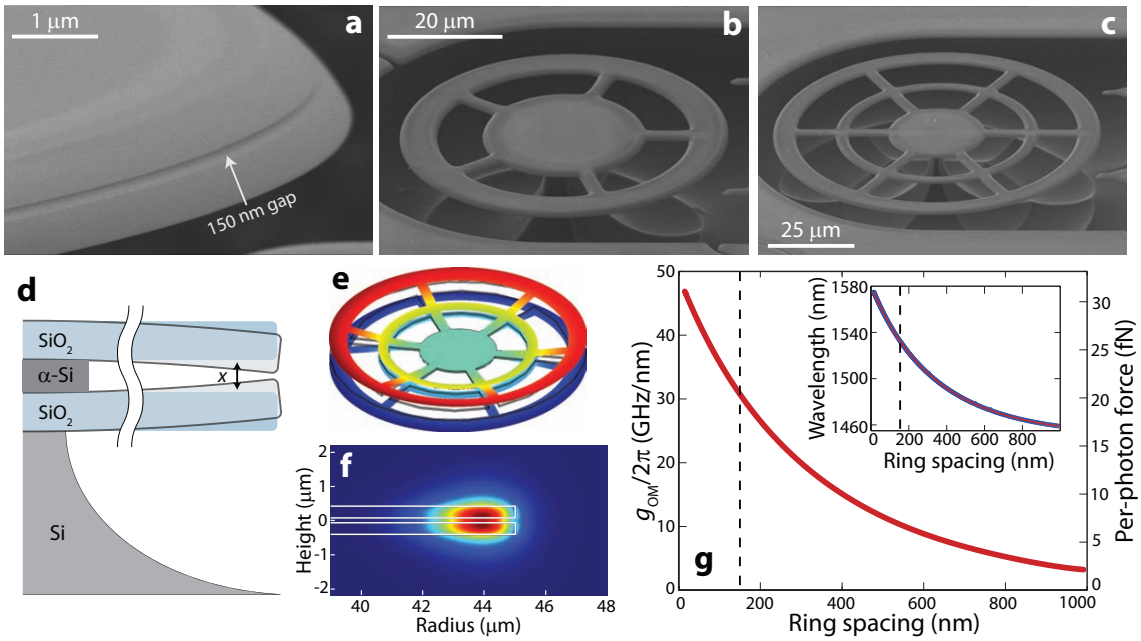

Figure 4.1: Scanning electron microscope images of (a) the between-ring gap, (b) the 54 μm spiderweb resonator, and (c) the 90 μm spiderweb resonator. (d) Schematic of a cross-section of the resonator, showing the bending of the two silica rings under the influence of the optical force. (e) Mechanical FEM simulation of the bending of the 90 μm spiderweb resonator. The outward bending motion is shown for ease of viewing, and is exaggerated for clarity. (f) FEM simulation of the radial component of the electric field for the fundamental TE bonding mode of the 90 μm spiderweb structure. (g) The theoretical wavelength tunability, per-photon force, and wavelength (inset) of the spiderweb cavity as a function of the ring spacing. The vertical dashed lines represent the experimentally-realized ring spacing of 150 nm.

web pattern was created using electron beam lithography followed by an optimized C_4F_8-SF_6 gas chemistry reactive ion etch. Release of the web structure was accomplished using a SF_6 chemical plasma etch which selectively $(30,000:1)$ attacks the intermediate α-Si layer and the underlying Si substrate, resulting in a uniform undercut region which extends radially inwards 4 μm on all boundaries, fully releasing the web. Simultaneously, the underlying silicon support pedestal is formed. Two nanoforks were also fabricated near the double-disk resonator to mechanically stabilize and support the fiber taper during optical coupling; the geometry was optimized such that the forks introduce a total insertion loss of only $\sim$4%.

The optomechanical coupling coefficient, $g_{\rm OM} \equiv d\omega_0/dx$, determines both the tunability and per-photon optical force [43, 76]. Finite-element-method (FEM) simulation shows that, for two 400-nm-thick planar silica whispering-gallery microcavities placed 150 nm apart (Fig. 4.1(f-g)), the resonance tunability is as large as $g_{\rm OM}/2\pi = 31$ GHz/nm (corresponding to a 21 fN/photon force). The corresponding static mechanical displacement for N photons stored inside the cavity is $\Delta x_{\rm static} = N\hbar g_{\rm OM}/k$, where k is the intrinsic spring constant of the mechanical structure. The overall magnitude of the cavity resonance tuning is then,

$$\Delta\omega_0 = g_{\rm OM}\Delta x_{\rm static} = \frac{N\hbar g_{\rm OM}^2}{k} = \frac{g_{\rm OM}^2 P_{\rm d}}{k\omega_0\Gamma_0}, \tag{4.1}$$

where $P_{\rm d}$ is the power dropped into the cavity and Γ_0 is the intrinsic photon decay rate, inversely proportional to the optical quality factor.

As the optical gradient force stems from the evanescent field coupling between the two near-field-spaced cavities, it is completely independent of the round-trip length of the cavity. This feature enables independent control of the optical and mechanical properties, allowing us to freely engineer the intrinsic mechanical rigidity through the scalability of the structure without changing the per-photon force. In order to minimize the mechanical stiffness while also providing mechanical stability, we utilize a spiderweb-like support structure consisting of an arrangement of spokes and inner rings [96]. The zeroth-order spiderweb cavity (Fig. 4.1(b)) has a 54 μm diameter outer ring supported by five spokes, while the first-order structure (Fig. 4.1(c)) has a 90 μm outer diameter ring with six spokes and one supporting inner ring. FEM simulations show that these structures have spring constants of 9.25 N/m and 1.63 N/m for the smaller and larger resonators, respectively.

In addition to the favorable mechanical properties, the whispering-gallery nature of the spiderweb resonator provides for high-Q optical resonances. Optical spectroscopy of the devices is

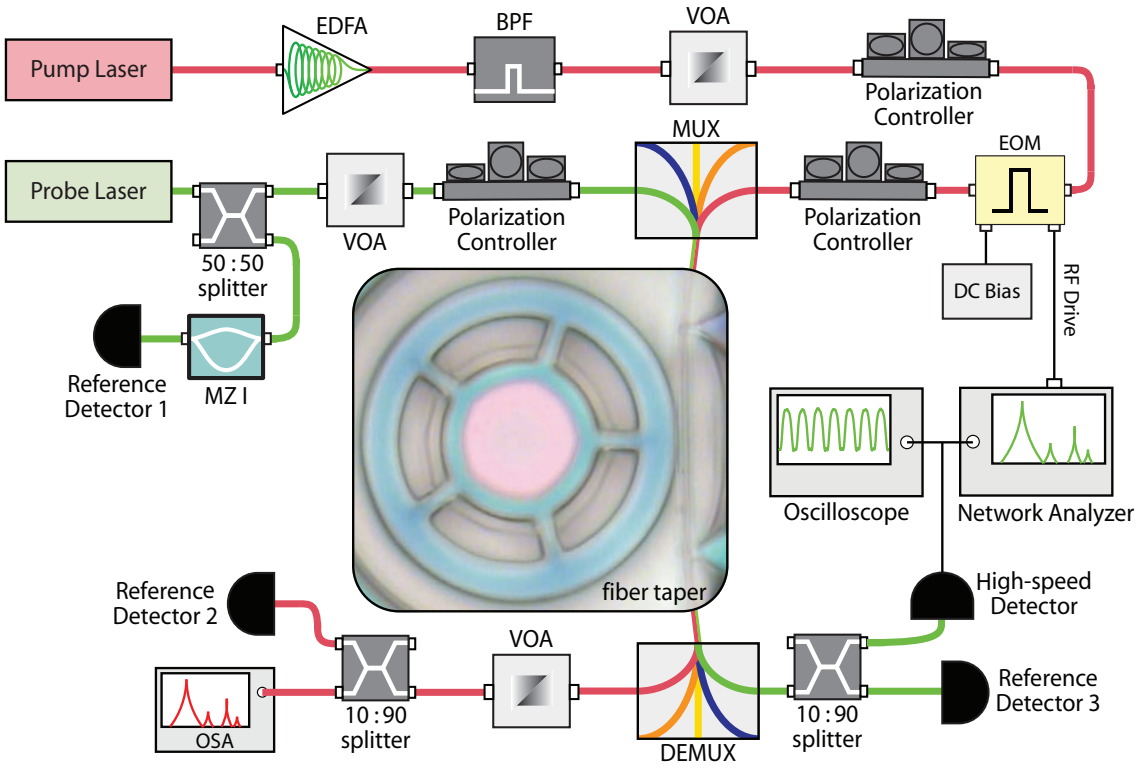

Figure 4.2: The pump and probe lasers are coupled to the spiderweb resonator via a single-mode silica fiber taper stabilized by two nanoforks fabricated near the device. The pump laser power is boosted by an erbium-doped fiber amplifier (EDFA) and passed through a band-pass filter (BPF). The two lasers are split into separate wavelength channels using a mux/demux system (providing greater than 120 dB pump-probe isolation). For modulation experiments, the pump laser wavelength is modulated using an electro-optic modulator (EOM) driven by a network analyzer. The laser power levels are controlled by several variable optical attenuators (VOAs), the probe wavelength is calibrated by a Mach-Zehnder interferometer (MZI), and the pump wavelength is monitored by an optical spectrum analyzer (OSA). The spiderweb device itself is contained within a nitrogen environment at atmospheric pressure.

performed using the experimental set-up shown in Fig. 4.2. Figure 4.3(a) shows the low power, in-plane polarized, wavelength scan of a 54-μm diameter resonator. The excited family of resonances, corresponding to the fundamental transverse-electric-like (TE-like) modes, has a free-spectral range (FSR) of 9.7 nm, with resonances at $\lambda = 1529$ nm and $\lambda = 1549$ nm exhibiting intrinsic quality factors of $Q_i = 1.04 \times 10^6$ and $Q_i = 0.90 \times 10^6$, respectively.

The extremely small intrinsic spring constant of the spiderweb resonator leads to significant thermal Brownian mechanical motion and introduces considerable fluctuations on the cavity transmission spectrum, as shown in Fig. 4.5(a). This makes it difficult to measure the optical Q factor of a cavity resonance. As discussed previously, the thermal Brownian mechanical motion can be significantly suppressed through the optical spring effect. This feature provides an elegant way to accurately characterize the optical Q of a cavity mode, by launching a relatively intense wave at a different resonance to suppress the perturbations induced by the thermal mechanical motion. Moreover, a complete theory developed previously in Sec. 2.4 and Ref. 48 was used to describe the linear cavity transmission with the inclusion of the optomechanical effect.

4.3 Static lter response

The combination of high cavity Q-factor, large g_{OM}, and floppy spiderweb structure result in the large optomechanical bistability shown in Fig. 4.3(b). With a power of 1.7 mW dropped into the cavity, the cavity resonance initially at $\lambda = 1549$ nm is shifted by 4.4 nm (a little more than 0.5 THz), corresponding to a static mechanical displacement of $\Delta x_{\mathrm{static}} = 17.7$ nm. We observed similar performance from the larger 90 μm spiderweb structures, although device yield (20%) and a slow change in device properties over time (despite devices being tested in a nitrogen environment to avoid water adsorption), indicate that further mechanical design optimization may be necessary for the larger structures. By comparison, the smaller 54-μm diameter structures had near-100% yield and maintained their properties over the entire period of testing.

As the mechanical displacement is universally experienced by all double-ring cavity modes, the displacement actuated by one cavity mode can be used to control the wavelength routing of an entire mode family, indicating a great potential for broad waveband translation and switching in the wavelength-division multiplexing configuration. This is demonstrated in Fig. 4.3(d), where the mechanical displacement actuated by the "pump" mode at $\lambda = 1549$ nm is used to control the wavelength of a "probe" mode initially located at $\lambda = 1529$ nm. With increased dropped pump

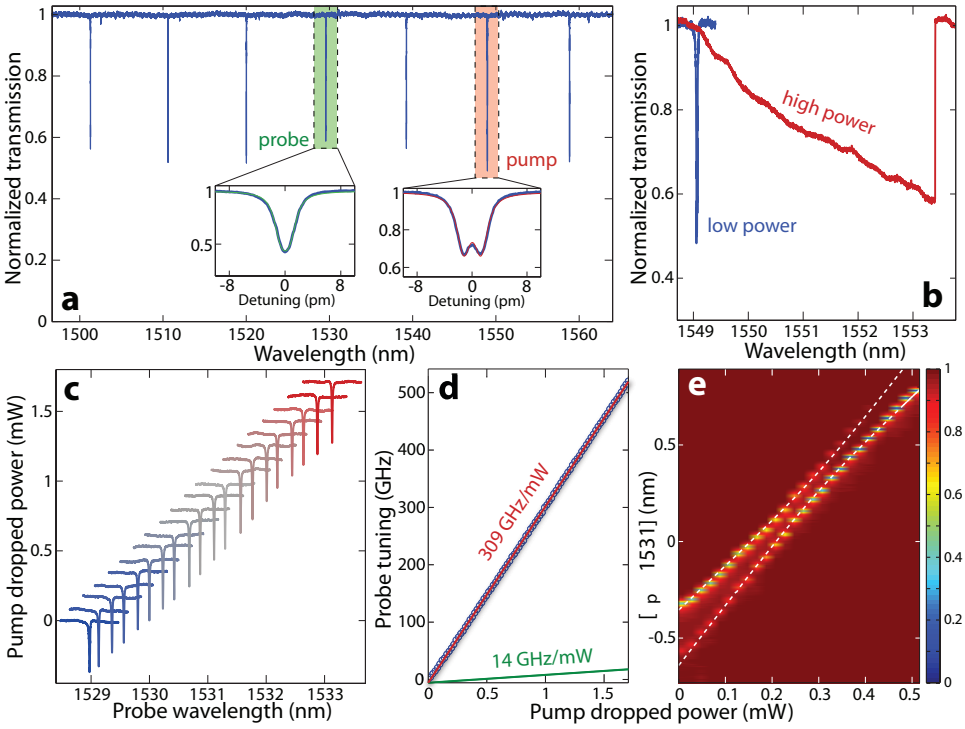

Figure 4.3: (a) Broadband optical transmission spectrum of the 54 μm spiderweb cavity. Inset: fine frequency scan of pump (probe) mode, highlighed in red (green), with Lorentzian fit to the lineshape. (b) Overcoupled pump-mode transmission spectrum at $P_d = 275$ nW (blue) and $P_d =$ 1.7 mW (red). (c) Probe-mode transmission curves for a selection of dropped powers in **d**, with P_d indicated by the baseline of each transmission curve. (d) Measured (blue circles) and linear fit (red curve) to the probe resonance wavelength tuning versus P_d. Green curve corresponds to thermo-optic component of tuning. (e) Intensity image of the optical transmission spectrum near the anticrossing of two TE- and TM-like probe modes.

power, the probe wavelength is tuned linearly and continuously by 4.2 nm, approximately 3000 times the probe resonance intrinsic channel linewidth (or 500 times the loaded linewidth). This factor is at least one order of magnitude larger than any other conventional approach previously reported [108–115, 117–119]. The tuning range shown in Fig. 4.3(d) is about 43% of the FSR. In principle, it is possible to tune over the entire free-spectral range with a moderate dropped pump power of only 4 mW. Importantly, this wavelength-routing approach is purely dispersive in nature and completely preserves the channel quality during the wavelength routing process as can be clearly seen in Fig. 4.3(c). This is in contrast to other tuning mechanisms such as the electro-optic approach via carrier injection [112, 118, 119], in which the accompanying carrier absorption degrades the quality of the switched channel and thus limits the ultimate tuning bandwidth.

A linear fit to the probe resonance tuning data data in Fig. 4.3(d) gives a tuning efficiency of 309 GHz/mW. This value agrees reasonably well with the theoretically predicted value of 393 GHz/mW, inferred from optical and mechanical FEM simulations and the measured optical Q-factor (see eq. (4.1)). Independent measurements show that the thermo-optic effect contributes only a small component to the overall tuning rate (13.8 GHz/mW; green curve in Fig. 4.3(d)), and FEM simulations indicate a negligible thermo-mechanical component ($\sim 0.06\%$).

The thermo-optical effect on the resonance tuning was calibrated by using another identical device on the same sample. To isolate the thermo-optic effect from the optomechanical effect, we caused the two rings to stick together through the van der Waals force, so the flapping mechanical motion was completely eliminated. Testing was performed on a cavity mode at 1552 nm using exactly the same conditions as for the wavelength routing measurements. A power of 2.1 mW dropped into the cavity introduces a maximum resonance red tuning by 0.23 nm, corresponding to a tuning rate of 0.11 nm/mW (13.8 GHz/mW), about 4% of the total tuning rate recorded experimentally.

The thermo-optic resonance tuning indicates a maximum temperature change of 21 K in the resonator. FEM simulations show that such a temperature variation of the resonator introduces a ring-gap change by only about 10 pm, shown by the differential displacement of the top and bottom rings in Fig. 4.4. Therefore, thermally induced static mechanical deformation has only a negligible contribution of 0.06% of the experimentally recorded wavelength tuning. The negligible contributions of both thermo-optic and thermo-mechanical effects are confirmed by the pump-probe modulation spectra shown in Fig. 4.5(d) and (e). This, and properties of the dynamical response of the system (see below), show that the wavelength routing is indeed a result of the optical gradient force. The difference between theoretical and experimental optical force tuning rates ($\sim 25\%$) can

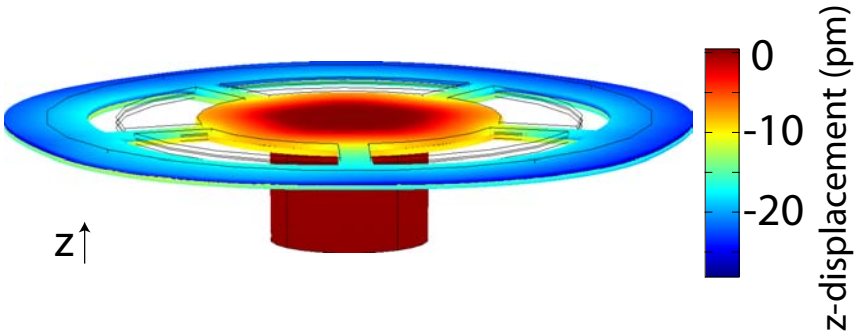

Figure 4.4: FEM simulation illustrating the z-displacement of a 54 μm spiderweb resonator under the 21 K temperature differential between substrate and ring induced by 2.1 mW dropped optical power.

likely be attributed to the uncertaintity in the Young's modulus of the annealed PECVD silica used to form the spiderweb structure.

In addition to the TE-like modes, the spiderweb double-ring resonator also supports a family of high-Q transverse-magnetic-like (TM-like) modes with a FSR of 10 nm. FEM simulations show that the per-photon force is slightly larger for the TM modes (26.5 fN/photon, or a 59% larger tuning efficiency), due primarily to the enhanced electric field strength in the nanoscale gap between the rings for polarization normal to the plane of the rings. Figure 4.3(e) shows the mode hybridization between a pair of TE and TM-like modes (the slight angle in the outer sidewall of the two rings breaks the vertical symmetry, allowing for mode-mixing) induced by the optical force tuning of the two mode families.

The anti-crossing between the two probe modes when they approach each other is primarily due to the internal coupling between the two cavity modes, which can be described by a simple theory as follows. Assume two cavity resonances located at ω_{01} and ω_{02}. For an input probe wave at ω, the two cavity modes are excited through the following equations:

$$\frac{da_1}{dt} = (i\Delta_1 - \frac{\Gamma_{t1}}{2})a_1 + i\beta a_2 + i\sqrt{\Gamma_{e1}}A_{in}, \tag{4.2}$$

$$\frac{da_2}{dt} = (i\Delta_2 - \frac{\Gamma_{t2}}{2})a_2 + i\beta a_1 + i\sqrt{\Gamma_{e2}}A_{in}, \tag{4.3}$$

where $\Delta_j = \omega - \omega_{0j}$ represents the cavity detuning of the j^{th} mode, and β is the optical coupling coefficient between the two cavity modes. With a continuous-wave input, the steady state of Eqs. (4.2)

and (4.3) is given by the following solution

$$a_1 = \frac{-iA_{\text{in}}\left[(i\Delta_2 - \Gamma_{t2}/2) \quad \overline{\Gamma_{e1}} - i\beta \quad \overline{\Gamma_{e2}}\right]}{(i\Delta_1 - \Gamma_{t1}/2)(i\Delta_2 - \Gamma_{t2}/2) + \beta^2}, \tag{4.4}$$

$$a_2 = \frac{-iA_{\text{in}}\left[(i\Delta_1 - \Gamma_{t1}/2) \quad \overline{\Gamma_{e2}} - i\beta \quad \overline{\Gamma_{e1}}\right]}{(i\Delta_1 - \Gamma_{t1}/2)(i\Delta_2 - \Gamma_{t2}/2) + \beta^2}. \tag{4.5}$$

As the transmitted field from the cavity is given by $A_T = A_{\text{in}} + i \quad \overline{\Gamma_{e1}} a_1 + i \quad \overline{\Gamma_{e2}} a_2$, the cavity transmission thus has the following equation

$$T \equiv \frac{A_T{}^2}{A_{\text{in}}{}^2} = \left| \frac{(i\Delta_1 - \frac{\Gamma_{01}-\Gamma_{e1}}{2})(i\Delta_2 - \frac{\Gamma_{02}-\Gamma_{e2}}{2}) + (\beta - i \quad \overline{\Gamma_{e1}\Gamma_{e2}})^2}{(i\Delta_1 - \Gamma_{t1}/2)(i\Delta_2 - \Gamma_{t2}/2) + \beta^2} \right|^2. \tag{4.6}$$

The experimental observation agrees well with this simple theory (dashed curve in Fig. 4.3(e)), giving a tuning efficiency for the TM modes which is 42% larger than that of the TE modes. This precisely tunable channel coupling may find applications in polarization switching/multiplexing/demultiplexing in optical signal processing, or carrier-sideband filtering in microwave photonics [124].

4.4 Dynamic lter response

In addition to the static mechanical actuation of the spiderweb structure, the optical gradient force also introduces dynamical back action which alters the dynamic response of the mechanical motion [33, 50, 125]. The in-phase component of the optical force leads to a modified mechanical resonance frequency and effective dynamical spring constant of

$$k \ = k + \frac{2g_{\text{OM}}^2 P_{\text{d}} \Delta}{\omega_0 \Gamma_0 [\Delta^2 + (\Gamma_t/2)^2]}, \tag{4.7}$$

where $\Delta = \omega_l - \omega_o$ is the detuning of the input laser (ω_l) from the cavity resonance (ω_o) frequency and Γ_t is the photon decay rate of the loaded cavity. As the intrinsic spring constant of the spiderweb resonator is small (9.5 N/m), the dynamical spring can be greatly modified optically. The alteration of the effective dynamic spring is clearly seen in the resonance spectra of the cavity resonances (left panel of Fig. 4.5(a)). For the floppy spiderweb structure, thermal Brownian motion introduces significant fluctuations in the cavity resonances. As pump power is dropped into the cavity, however, the dynamic spring stiffens and strongly suppresses the magnitude of the thermal fluctuations (right panel of Fig. 4.5(a)).

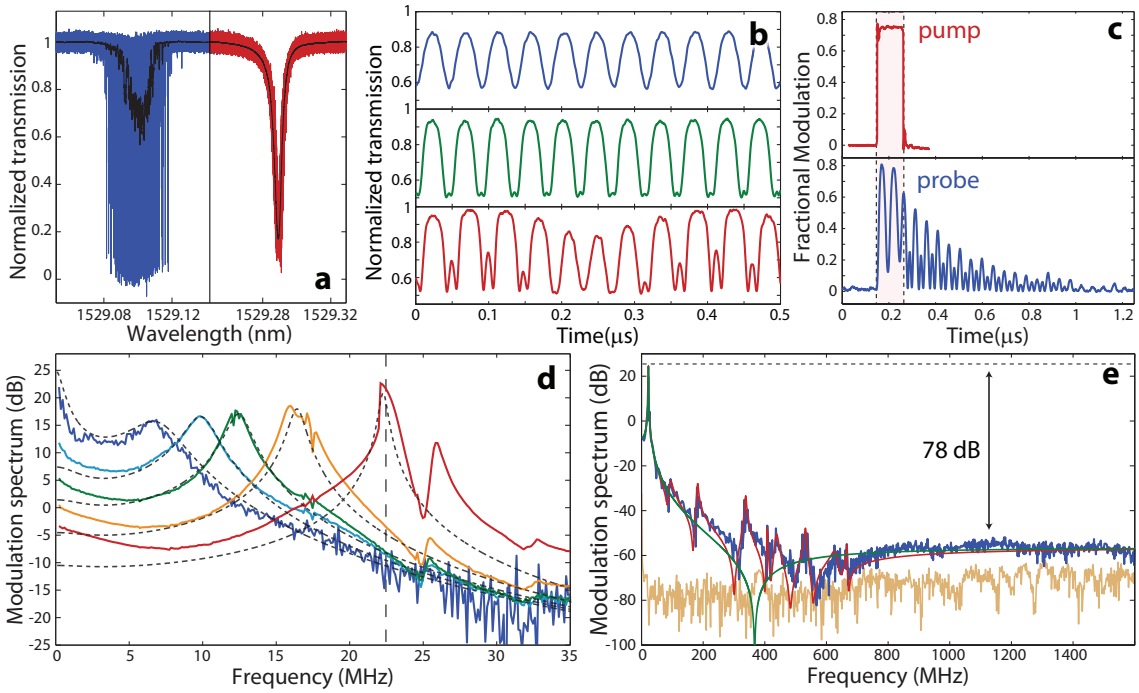

Figure 4.5: (a) Undercoupled probe transmission spectra recorded at low ($P_d = 0$ mW (blue)) and high ($P_d = 0.20$ mW (red)) pump power (time-averaged trace in black). (b) Time waveforms of the probe transmission for sinusoidally modulated (22.3 MHz; vertical dashed line in (d)) pump mode with modulation depths of 1.9% (blue), 14.9% (green), and 20.5% (red) at average $P_d = 0.85$ mW. (c) Pulsed modulation of the pump (top) and corresponding probe response (bottom). The fractional modulation for the pump is defined relative to the average dropped power, while that for the probe is defined relative to the on-resonance probe-mode coupling depth. (d) Normalized probe modulation spectra for $P_d = \ 14, 110, 210, 430, 850 \ \ \mu$W. The dashed black curves show the corresponding model. (e) Probe modulation spectrum ($P_d = 0.85$ mW) shown over a wide frequency span. The green curve shows the modeled response including only the dominant flapping mechanical mode (the red curve includes other, breathing-like, mechanical resonances). The orange curve shows the measured noise floor.

Optical control of the dynamic response is most clearly demonstrated through the pump-probe modulation response of the spiderweb structure. In general, the pump wave inside the cavity satisfies the following equation:

$$\frac{da_p}{dt} = (i\Delta_p - \frac{\Gamma_{\rm tp}}{2})a_p - ig_{\rm OM}xa_p + i\gamma\, a_p\,^2 a_p + i\sqrt{\Gamma_{\rm ep}}A_{\rm p}, \tag{4.8}$$

where a_p and A_p are the intracavity and input field of the pump wave, respectively, normalized such that $U_p \equiv a_p\,^2$ and $P_p \equiv A_p\,^2$ represent the intracavity energy and input power. $\Delta_p = \omega_p - \omega_{0\rm p}$ represents the detuning of pump frequency ω_p to the cavity resonance $\omega_{0\rm p}$ and $\Gamma_{\rm tp}$ is the photon decay rate of the loaded cavity for the pump mode. In Eq. (4.8), the third term represents the back action of mechanical motion on the cavity resonance, where $g_{\rm OM}$ is the optomechanical coupling coefficient and $x(t)$ is the mechanical displacement of the cavity structure. The fourth term describes the self-phase modulation introduced by the Kerr nonlinearity, where the nonlinear parameter $\gamma = \frac{c\omega_p n_2}{n_0^2 V_{\rm eff}}$, $n_2 = 2.6\times10^{-20}$ m^2/W is the Kerr nonlinear coefficient of silica, $n_0 = 1.44$ is the silica refractive index, and $V_{\rm eff} = 370\ \mu$m^2 (from FEM simulation) is the effective mode volume [126–128]. However, compared with the dominant optomechanical effect, the self-phase modulation on the pump wave is negligible in the spiderweb ring resonator. The final term in Eq. (4.8) represents the external field coupling with a photon escape rate of $\Gamma_{\rm ep}$.

Assume that the input pump wave consists of an intense continuous wave together with a small time-varying modulation, $A_p = A_{\rm p0} + \delta A_p(t)$. The intracavity field can be written as $a_p = a_{\rm p0} + \delta a_p(t)$, governed by the following equations:

$$\frac{da_{\rm p0}}{dt} = (i\Delta_p - \frac{\Gamma_{\rm tp}}{2})a_{\rm p0} + i\sqrt{\Gamma_{\rm ep}}A_{\rm p0}, \tag{4.9}$$

$$\frac{d\delta a_p}{dt} = (i\Delta_p - \frac{\Gamma_{\rm tp}}{2})\delta a_p - ig_{\rm OM}xa_{\rm p0} + i\sqrt{\Gamma_{\rm ep}}\delta A_{\rm p}, \tag{4.10}$$

where we have neglected the negligible self-phase modulation for the pump wave. Equation (4.9) provides a steady-state solution of

$$a_{\rm p0} = \frac{i\sqrt{\Gamma_{\rm ep}}A_{\rm p0}}{\Gamma_{\rm tp}/2 - i\Delta_p}, \tag{4.11}$$

from which we obtain the average pump power dropped into the cavity, $P_{\rm pd}$, given by

$$P_{\rm pd} = \frac{P_{\rm p0}\Gamma_{0\rm p}\Gamma_{\rm ep}}{\Delta_p^2 + (\Gamma_{\rm tp}/2)^2}, \tag{4.12}$$

where $P_{\mathrm{p0}} = |A_{\mathrm{p0}}|^2$ is the averaged input pump power and $\Gamma_{0\mathrm{p}}$ is the intrinsic photon decay rate of the pump mode. Clearly, to the zeroth order, the relative magnitude of the dropped pump power modulation is directly equal to that of the input modulation:

$$\frac{\delta P_{\mathrm{pd}}(t)}{P_{\mathrm{pd}}} = \frac{\delta P_p(t)}{P_{\mathrm{p0}}}, \tag{4.13}$$

where $\delta P_p = A^*_{\mathrm{p0}}\delta A_p + A_{\mathrm{p0}}\delta A^*_p$ is the time-varying component of the input pump power.

Eq. (4.10) leads to a pump-field modulation in the frequency domain of

$$\delta\widetilde{a}_p(\Omega) = \frac{ig_{\mathrm{OM}}a_{\mathrm{p0}}\widetilde{x}(\Omega) - i\sqrt{\Gamma_{\mathrm{ep}}}\delta\widetilde{A}_p(\Omega)}{i(\Delta_p+\Omega)-\Gamma_{\mathrm{tp}}/2}, \tag{4.14}$$

where $\delta\widetilde{a}_p(\Omega)$, $\widetilde{x}(\Omega)$, and $\delta\widetilde{A}_p(\Omega)$ are Fourier transforms of $\delta a_p(t)$, $x(t)$, and $\delta A_p(t)$, respectively, defined as $\widetilde{B}(\Omega) = \int_{-\infty}^{+\infty} B(t)e^{i\Omega t}dt$. Physically, the first term in Eq. (4.14) represents the perturbation induced by the mechanical motion, while the second term represents the effect of direct input modulation.

The optical gradient force is linearly proportional to the cavity energy as $F_o = -\frac{g_{\mathrm{OM}}U_p}{\omega_p}$. With modulation of the pump energy, the gradient force thus consists of two terms, $F_o = F_{o0} + \delta F_o(t)$, where $F_{o0} = -\frac{g_{\mathrm{OM}}U_{\mathrm{p0}}}{\omega_p}$ is the static force component introduced by the averaged pump energy $U_{\mathrm{p0}} = |a_{\mathrm{p0}}|^2$, and $\delta F_o(t)$ is the dynamic component related to the pump energy modulation $\delta U_p(t)$, given by

$$\delta F_o(t) = -\frac{g_{\mathrm{OM}}\delta U_p}{\omega_p} = -\frac{g_{\mathrm{OM}}}{\omega_p}\left[a^*_{\mathrm{p0}}\delta a_p(t) + a_{\mathrm{p0}}\delta a^*_p(t)\right]. \tag{4.15}$$

Substituting Eq. (4.14) into Eq. (4.15), we find the force modulation is described by this general form in the frequency domain:

$$\delta\widetilde{F}_0(\Omega) = f_o(\Omega)\widetilde{x}(\Omega) + \frac{i\sqrt{\Gamma_{\mathrm{ep}}}g_{\mathrm{OM}}}{\omega_p}\left[\frac{a^*_{\mathrm{p0}}\delta\widetilde{A}_p(\Omega)}{i(\Delta_p+\Omega)-\Gamma_{\mathrm{tp}}/2} + \frac{a_{\mathrm{p0}}\delta\widetilde{A}^*_p(-\Omega)}{i(\Delta_p-\Omega)+\Gamma_{\mathrm{tp}}/2}\right], \tag{4.16}$$

where the first term represents the back action introduced by the mechanical motion, with a spectral response $f_0(\Omega)$ given by

$$f_o(\Omega) \equiv -\frac{2g^2_{\mathrm{OM}}\,|a_{\mathrm{p0}}|^2\Delta_p}{\omega_p}\frac{\Delta_p^2 - \Omega^2 + (\Gamma_{\mathrm{tp}}/2)^2 + i\Gamma_{\mathrm{tp}}\Omega}{\left[(\Delta_p+\Omega)^2+(\Gamma_{\mathrm{tp}}/2)^2\right]\left[(\Delta_p-\Omega)^2+(\Gamma_{\mathrm{tp}}/2)^2\right]}. \tag{4.17}$$

Figure 4.5(d) shows the spectral response of a probe resonance to small-signal sinusoidal pump

modulation for several different (average) pump dropped powers. When the pump dropped power is low, the pump back-action on mechanical motion is negligible and the probe response is given by a combination of the intrinsic mechanical stiffness and the squeeze-film effect [84] of trapped gas in between the rings. When the pump power is increased, however, the mechanical resonance frequency increases correspondingly, reaching a value of 22.3 MHz at a dropped power of 0.85 mW. This value is about 32 times larger than the intrinsic mechanical frequency, and implies a dynamical stiffness more than 1000 times that of the silica rings.

The spiderweb ring resonators are separated by a 150 nm gap, which is only about 2.2 times the mean free path in a nitrogen environment ($\sim$68 nm). As the ring is ~ 6.3 μm wide, much larger than the ring gap, the nitrogen gas sandwiched in the gap is highly confined by the two silica layers and cannot move freely during the flapping motion of the two rings. The resulting significant pressure differential between the internal and external regions of the paired silica rings functions as a viscous force to damp the mechanical motion. This phenomenon is well-known as the squeeze-film effect, which has a profound impact on the dynamic response of micro/nano-mechanical systems [84]. Apart from the optical gradient force, the squeeze-film effect is the dominant mechanism responsible for the dynamic mechanical response of our devices. The associated damping force can be described by a general form of $\widetilde{F}_{\rm sq}(\Omega) = f_{\rm sq}(\Omega)\widetilde{x}(\Omega)$, where $f_{\rm sq}(\Omega)$ represents the spectral response of the squeeze film.

In general, the squeeze-film effect is typically described by two theories which work in quite different regimes, depending on the Knudsen number K_n characterizing the ratio between the mean-free path and the gap [84]. In the classical regime with $K_n \ll 1$ where the gas can be considered a continuum, the squeeze-film viscous force for a rectangular plate is well described by $f_{\rm sq}(\Omega) = -k_e(\Omega) + iC_d(\Omega)$, where k_e and C_d represent the spring constant and damping, respectively, induced by the squeeze film. They are given by the following equations [129]

$$k_e(\Omega) = \frac{64\sigma^2 P_a L_0 W_0}{\pi^8 h_0} \sum_{m,n\ odd} \frac{1}{m^2 n^2 \left[(m^2+(n/\eta)^2)^2 + \sigma^2/\pi^4\right]}, \tag{4.18}$$

$$C_d(\Omega) = \frac{64\sigma P_a L_0 W_0}{\pi^6 h_0} \sum_{m,n\ odd} \frac{m^2+(n/\eta)^2}{m^2 n^2 \left[(m^2+(n/\eta)^2)^2 + \sigma^2/\pi^4\right]}, \tag{4.19}$$

where P_a is the ambient gas pressure, W_0 and L_0 are the width and length of the plate, h_0 is the gap,

$\eta = L_0/W_0$ is the aspect ratio of the plate, and σ is the squeeze number given by

$$\sigma(\Omega) = \frac{12\mu_{\text{eff}} W_0^2 \Omega}{P_a h_0^2}, \tag{4.20}$$

where $\mu_{\text{eff}} = \mu/(1 + 9.638K_n^{1.159})$ is the effective value of the viscosity coefficient μ [130]. Under this model, the squeeze film functions primarily as a damping (or elastic) force when the modulation frequency is below (or above) the cutoff frequency given by

$$\Omega_c = \frac{\pi^2 P_a h_0^2}{12\mu_{\text{eff}}} \left(\frac{1}{W_0^2} + \frac{1}{L_0^2} \right). \tag{4.21}$$

In contrast, in the free-molecule regime with $K_n \gg 1$ where the interaction between gas molecules is negligible, the squeeze film approximately behaves like a damping force, $f_{\text{sq}}(\Omega) = iC_r\Omega$, with C_r given by the following equation [131, 132]

$$C_r = \left(\frac{S}{16\pi h_0} \right) 4P_a L_0 W_0 \sqrt{\frac{2M_m}{\pi \mathcal{R} T}}, \tag{4.22}$$

where M_m is the molar mass of gas, T is the temperature, $\mathcal{R}$ is the ideal gas constant, S is the perimeter length of the gap region.

However, our devices have a Knudsen number of $K_n = 0.45$, falling in the crossover regime where neither theory adequately describes the squeeze-film effect [133]. As the device works in the regime between the continuum and free-molecule limit, we heuristically propose that the damping/elastic force of the squeeze film is effectively described by a composite of the two theories:

$$f_{\text{sq}}(\Omega) = -k_e(\Omega) + iC_d(\Omega) + i\eta_r C_r \Omega, \tag{4.23}$$

with a modified effective coefficient of viscosity $\mu_{\text{eff}} = \eta_\mu \mu_{\text{eff}}$, where η_r and η_μ are parameters used for a best description of the squeeze-film response in our devices. Detailed analysis shows that $\eta_\mu = 0.7$ and $\eta_r = 0.03$ provides the best fit for our devices. As our devices have a spiderweb geometry, we approximate it with an equivalent rectangular shape with W_0 given by the ring width, L_0 given by the circumference at the ring center, and $S \approx 2L_0$. As shown by the experimental results and theoretical fits, this model provides an accurate description of the squeeze-film effect in our devices.

Although the intrinsic mechanical frequency of the 54 μm spiderweb structure is 694 kHz (in-

dicated by FEM simulation), Fig. 4.5(d) shows a minimum dynamic frequency response of 6 MHz, dominated by the squeeze-film damping. Interestingly, although squeeze-film damping is generally detrimental in other micro/nanomechanical systems [84, 134], it is beneficial in this case, as it helps to extend the modulation bandwidth for wavelength routing.

With the optical gradient force and the squeeze-film damping force, the mechanical motion of the cavity satisfies the following equation:

$$\frac{d^2x}{dt^2}+\Gamma_m\frac{dx}{dt}+\Omega_m^2 x=\frac{1}{m_{\text{eff}}}(F_o+F_{\text{sq}}+F_T)=\frac{1}{m_{\text{eff}}}(F_{o0}+\delta F_o+F_{\text{sq}}+F_T), \tag{4.24}$$

where m_{eff} is the effective motional mass of the flapping mechanical mode, and Ω_m and Γ_m are intrinsic mechanical frequency and damping rate, respectively. F_T is the thermal Langevin force responsible for the thermal Brownian motion, a Markovin process with the following correlation function:

$$F_T(t)F_T(t+\tau) \ = 2m_{\text{eff}}\Gamma_m k_B T\delta(\tau), \tag{4.25}$$

where k_B is Boltzmann's constant.

As the squeeze-film viscous force is zero at $\Omega=0$, the squeeze gas film impacts only the dynamic response of mechanical motion. Equation (4.24) shows clearly that the static mechanical displacement is actuated only by the static component of the optical force given by

$$x_0=\frac{F_{o0}}{m_{\text{eff}}\Omega_m^2}=\frac{g_{\text{om}}U_{\text{p0}}}{k_m\omega_p}=\frac{g_{\text{om}}P_{\text{pd}}}{k_m\omega_p\Gamma_{0\text{p}}}, \tag{4.26}$$

where $k_m=m_{\text{eff}}\Omega_m^2$ is the intrinsic spring constant of the spiderweb structure. With a specifically designed extremely small spring constant, x_0 can be quite significant for a given dropped power. As a result, the cavity resonance can be tuned by a significant magnitude of $g_{\text{OM}}x_0$. This is the primary mechanism responsible for the resonance tuning. On the other hand, this static mechanical displacement primarily changes the equilibrium position of the mechanical motion. It is convenient to remove this component in Eq. (4.24) by defining $x \ = x-x_0$, since both the squeeze-film damping force and dynamic component of the optical force affect only the dynamics of x .

Substituting Eqs. (4.16), (4.17), (4.23) into Eq. (4.24) in the frequency domain, we find that the squeeze-film damping force and the backaction term of the optical force primarily change the values

of the resonant frequency and damping rate of the mechanical motions. Defining

$$\mathcal{L}(\Omega) \equiv \Omega_m^2 - \Omega^2 - i\Gamma_m\Omega - \frac{f_o(\Omega)}{m_{\text{eff}}} - \frac{f_{\text{sq}}(\Omega)}{m_{\text{eff}}}, \tag{4.27}$$

the mechanical displacement is thus given by

$$\widetilde{x}(\Omega) = \frac{\widetilde{F}_T(\Omega)}{m_{\text{eff}}\mathcal{L}(\Omega)} + \frac{i\sqrt{\Gamma_{\text{ep}}}g_{\text{OM}}}{m_{\text{eff}}\omega_p\mathcal{L}(\Omega)}\left[\frac{a_{\text{p0}}^*\delta\widetilde{A}_p(\Omega)}{i(\Delta_p+\Omega)-\Gamma_{\text{tp}}/2} + \frac{a_{\text{p0}}\delta\widetilde{A}_p^*(-\Omega)}{i(\Delta_p-\Omega)+\Gamma_{\text{tp}}/2}\right], \tag{4.28}$$

where we have dropped the prime notation of x for simplicity.

The first term in Eq. (4.28) represents the thermal Brownian motion while the second term describes the motions actuated by the pump modulation. In the absence of pump modulation, the mechanical motion is dominated by the Brownian motion. By using Eq. (4.25), we find the spectral density of thermal mechanical displacement has the form

$$\mathcal{S}_x(\Omega) = \frac{2\Gamma_m k_B T}{m_{\text{eff}}\ \mathcal{L}(\Omega)\ ^2}. \tag{4.29}$$

Equations (4.16), (4.17), and (4.27) show that one dominant effect of the pump energy inside the cavity is to increase the mechanical rigidity, the so-called optical spring effect. In most cases, $\mathcal{L}(\Omega)$ can be well approximated by $\mathcal{L}(\Omega) \approx (\Omega_m)^2 - \Omega^2 - i\Gamma_m\Omega$ with a new mechanical resonance Ω_m and damping rate Γ_m affected by the optical force. Equation (4.29) thus leads to a variance of the thermal mechanical displacement given by

$$(\delta x)^2 \ = \frac{1}{2\pi}\int_{-\infty}^{+\infty}\mathcal{S}_x(\Omega)d\Omega = \frac{k_B T\Gamma_m}{k_m\Gamma_m} \approx \frac{k_B T}{k_m}, \tag{4.30}$$

where $k_m = m_{\text{eff}}(\Omega_m)^2$ is the effective spring constant and the approximation in the final term assumes a negligible change in the mechanical linewidth. Clearly, the increase of the mechanical resonance frequency through the optical spring effect dramatically suppresses the magnitude of the thermal mechanical displacement and its perturbation of the cavity resonance, as shown in Fig. 4.5(a). In the presence of pump modulation, the mechanical motion is primarily dominated by the dynamic optical force rather than the actuation from the thermal Langevin force, and the first term is negligible compared with the second term in Eq. (4.28). Thus, we neglect the thermal Brownian term in the following discussion.

The probe wave inside the cavity is governed by a dynamic equation similar to Eq. (4.8):

$$\frac{da_s}{dt} = (i\Delta_s - \frac{\Gamma_{\rm ts}}{2})a_s - ig_{\rm OM}xa_s + 2i\gamma\, a_p\,^2 a_s + i\sqrt{\Gamma_{\rm es}}A_{\rm s}, \tag{4.31}$$

except that the Kerr-nonlinear term now describes the cross-phase modulation from the pump wave. With the perturbations induced by the pump modulation, similar to the previous discussion of the pump wave, the intracavity probe field can be written as $a_s = a_{\rm s0} + \delta a_s(t)$, governed by the following equations:

$$\frac{da_{\rm s0}}{dt} = (i\Delta_s - \frac{\Gamma_{\rm ts}}{2})a_{\rm s0} + 2i\gamma U_{\rm p0}a_{\rm s0} + i\sqrt{\Gamma_{\rm es}}A_{\rm s}, \tag{4.32}$$

$$\frac{d\delta a_s}{dt} = (i\Delta_s - \frac{\Gamma_{\rm ts}}{2})\delta a_s + 2i\gamma U_{\rm p0}\delta a_{\rm s} - ig_{\rm OM}xa_{\rm s0} + 2i\gamma\delta U_p a_{\rm s0}, \tag{4.33}$$

where we have assumed the probe input is a continuous wave with a power of $P_s = A_s\,^2$. The second terms of Eqs. (4.32) and (4.33) represent the static cavity tuning introduced by cross-phase modulation, which can be included in the cavity tuning term Δ_s for simplicity. In general, it is negligible compared with the cavity linewidth at the power level used for exciting optomechanical effects, leading to $2\gamma U_{\rm p0} \ll \Gamma_{\rm tp}, \Gamma_{\rm ts}$.

Equation (4.32) provides a steady-state solution of

$$a_{\rm s0} = \frac{i\ \ \overline{\Gamma_{\rm es}}A_{\rm s}}{\Gamma_{\rm ts}/2 - i\Delta_s}, \tag{4.34}$$

and Eq. (4.33) results in a probe-field modulation in the frequency domain of

$$\delta\widetilde{a}_s(\Omega) = \frac{ia_{\rm s0}\left[g_{\rm OM}\widetilde{x}(\Omega) - 2\gamma\delta\widetilde{U}_p(\Omega)\right]}{i(\Delta_s + \Omega) - \Gamma_{\rm ts}/2}, \tag{4.35}$$

where $\delta\widetilde{U}_p(\Omega)$ is the Fourier transform of $\delta U_p(t)$. As the transmitted field of the probe is given by $A_{\rm Ts} = A_s + i\ \ \overline{\Gamma_{\rm es}}a_s$, the modulation of the transmitted probe power thus takes the form

$$\delta P_{\rm Ts} = i\sqrt{\Gamma_{\rm es}}(A^*_{\rm 0s}\delta a_s - A_{\rm 0s}\delta a^*_s), \tag{4.36}$$

where $A_{\rm 0s} = A_s + i\ \ \overline{\Gamma_{\rm es}}a_{\rm s0}$ is the transmitted probe wave in the absence of modulation. By use of Eqs. (4.14), (4.28), (4.34) and (4.35), we find that the power spectrum of the transmitted probe

modulation is given by the following equation:

$$\frac{\delta\widetilde{P}_{\mathrm{Ts}}(\Omega)^{\,2}}{P_s^2}=\left|\frac{g_{\mathrm{OM}}^2}{m_{\mathrm{eff}}\omega_p\mathcal{L}(\Omega)}+2\gamma\right|^2\frac{P_{\mathrm{pd}}^2}{\Gamma_{0\mathrm{p}}^2}\frac{\delta\widetilde{P}_{\mathrm{pd}}(\Omega)^{\,2}}{P_{\mathrm{pd}}^2}\frac{4\Gamma_{\mathrm{es}}^2\Gamma_{0\mathrm{s}}^2\Delta_s^2}{[\Delta_s^2+(\Gamma_{\mathrm{ts}}/2)^2]^4}, \tag{4.37}$$

where $\Gamma_{0\mathrm{s}}$ is the intrinsic photon decay rate of the probe mode, and $\delta\widetilde{P}_{\mathrm{Ts}}(\Omega)$ and $\delta\widetilde{P}_{\mathrm{pd}}(\Omega)$ are the Fourier transforms of $\delta P_{\mathrm{Ts}}(t)$ and $\delta P_{\mathrm{pd}}(t)$, respectively. To obtain Eq. (4.37), we have used Eq. (4.13) to relate the dropped pump power to the input, and have also taken into account the fact that the Kerr effect is relatively small, such that $2\gamma U_{\mathrm{p0}}\ll\Gamma_{\mathrm{tp}}$. We also assume the cavity is in the sideband-unresolved regime with $\Omega_m\ll\Gamma_{\mathrm{tp}},\Gamma_{\mathrm{ts}}$. The modulation spectra given in Fig. 4.5 are defined as

$$\rho(\Omega)\equiv\frac{\delta\widetilde{P}_{\mathrm{Ts}}(\Omega)^{\,2}/P_s^2}{\delta\widetilde{P}_{\mathrm{pd}}(\Omega)^{\,2}/P_{\mathrm{pd}}^2}. \tag{4.38}$$

For a better comparison of the dynamic-backaction induced variations on the probe modulation, the modulation spectra shown in Fig. 4.5(d) are normalized by a factor corresponding to the ratio of the dropped power for each curve relative to the maximum dropped power. Therefore, the plotted modulation spectra are given by

$$\rho\ (\Omega)\equiv\rho(\Omega)\frac{P_{\mathrm{pd0}}^2}{P_{\mathrm{pd}}^2}=\frac{\delta\widetilde{P}_{\mathrm{Ts}}(\Omega)^{\,2}/P_s^2}{\delta\widetilde{P}_{\mathrm{pd}}(\Omega)^{\,2}/P_{\mathrm{pd0}}^2}, \tag{4.39}$$

where $P_{\mathrm{pd0}}=0.85$ mW is the maximum drop power used in Fig. 4.5(d).

The derivations above take into account only the flapping mechanical mode, since it is most strongly actuated by the optical gradient force. In general, there are many mechanical resonances for the spiderweb resonators, but weakly coupled to the optical waves inside the cavity. In this case, following the same procedure above, it is easy to show that the spectral response of probe modulation now becomes

$$\rho(\Omega)=\left|2\gamma+\sum_j\frac{g_j^2}{m_{\mathrm{j}}\omega_p\mathcal{L}_j(\Omega)}\right|^2\frac{P_{\mathrm{pd}}^2}{\Gamma_{0\mathrm{p}}^2}\frac{4\Gamma_{\mathrm{es}}^2\Gamma_{0\mathrm{s}}^2\Delta_s^2}{[\Delta_s^2+(\Gamma_{\mathrm{ts}}/2)^2]^4}, \tag{4.40}$$

where g_j, m_j, and $\mathcal{L}_j(\Omega)$ are optomechanical coupling coefficient, effective motional mass, and the spectral response of mechanical motions, respectively, for the j^{th} mechanical mode. For those weakly actuated mechanical modes, $\mathcal{L}_j(\Omega)=\Omega_{\mathrm{mj}}^2-\Omega^2-i\Gamma_{\mathrm{mj}}\Omega$ where Ω_{mj} and Γ_{mj} are the resonance frequency and damping rate of the j^{th} mechanical mode. Equation (4.40) was used to describe

the modulation spectrum shown in Fig. 4.5(d).

As shown in the dashed curves in Fig. 4.5(d), eq. (4.37) provides an accurate description of the pump-probe modulation response (the Fano-like resonance seen at $P_d = 0.85$ mW is due to intrinsic mechanical coupling between different types of motion, and is discussed in Chapter 3). In general, the small modulation of the pump wave which actuates the mechanical oscillation is greatly magnified on the probe resonance. Figure 4.5(d) shows that for $P_d = 0.85$ mW there is a resonant modulation "gain" of greater than 20 dB. This can also be seen in the time waveform of the probe in Fig. 4.5(b), where a 1.9% modulation of the pump power is large enough to introduce considerable fractional modulation in the probe time waveform (top panel). Increasing the pump modulation to 14.9% (Fig. 4.5(b), middle panel) results in a probe modulation of larger than a half-linewidth (full contrast modulation). Further increase in the pump modulation depth actuates flapping mechanical motion so intense it begins to excite a second mechanical mode (the Fano-like feature in Fig. 4.5(d)), resulting in a beat signal with a period of 0.36 μs on the probe time waveform.

One metric for characterizing the response time of the spiderweb optomechanical cavity is the resonant oscillation period [120]. Figure 4.5(d) shows that the optical spring effect enables a modulation time as fast as 44.8 ns. This can be further enhanced by using the transduction "gain" to push the probe modulation into the nonlinear regime, where in the lower panel of Fig. 4.5(b) the probe wavelength (10%–90%) on-off switching time is reduced to 7 ns, roughly 3 orders of magnitude faster than modulation schemes based upon thermo-optic, optofluidic, photochemical, or micro-electricalmechancial approaches [108–111, 113–115, 117, 120]. For many switching applications, however, one is more interested in the impulse response of the system. The pulsed response of the probe is shown in Fig. 4.5(c). As is common in micro/nanomechanical systems [114, 120], the resonant response causes ringing during switching, with a settling time determined by the mechanical linewidth. The measured settling time constant of the probe response is 196 ns, consistent with the mechanical linewidth of $\sim$ 2-3 MHz (see Fig. 4.5(d)).

In addition to the optomechanical nonlinearity, other optical (material, etc.) nonlinearities can also contribute to the probe modulation. As shown in the expanded modulation spectrum of Fig. 4.5(e), the resonant optomechanical nonlinearity is dominant out to a frequency of 500 MHz, after which the response plateaus due to the ultrafast Kerr nonlinearity of silica. The Kerr nonlinearity is measured to be 78 dB below the resonant optomechanical response. This ratio agrees well with the theoretical value of 81 dB given by $\left(\frac{g_{\mathrm{OM}}^2}{2\gamma m_{\mathrm{eff}}\omega_p\Omega_m\Gamma_m}\right)^2$, where Ω_m and Γ_m are the effective mechanical resonance frequency and damping rate, respectively. The Kerr nonlinearity in silica has

been extensively studied over more than three decades for optical signal processing [126, 135, 136], and the excellent agreement between the theoretical and experimental spectra provides yet another indication that the optical gradient force is the dominant tuning mechanism in the spiderweb cavity structure.

4.5 Discusssion

The versatility of the gradient optical force tuning approach described here provides considerable room for future improvement of device performance. An increase in the tuning range and efficiency (actuation power) can be expected with further engineering of the mechanical stability of the spiderweb structure. For example, the 90 μm diameter first-order spiderweb cavities should allow for a six-fold increase in tuning efficiency to approximately 15 nm/mW. There are also many well-established methods for managing the dynamical response, in particular the ringing, of resonant micro- and nano-mechanical systems [114, 120]. In contrast to cavity-optomechanical applications such as cooling and amplification of mechanical motion [50, 125], a reduction in the mechanical Q-factor, which can be obtained through elevated gas pressure or incorporation of damping materials, is sought to improve the switching time. Given the similarity of the double-ring spiderweb stucture to other more conventional planar microring technologies, one can also incorporate other chip-based optical components such as waveguides, lasers, and modulators to enable full control and functionality of the optomechanics. One example technology would be an on-chip reconfigurable optical add/drop multiplexer or wavelength selective switch/crossconnect, which could be accomplished by integrating an array of double-ring cavities into a parallel or cascaded configuration. In addition to the demonstrated wavelength routing, other prospective applications for optomechanical devices include tunable optical buffering [137], dispersion compensation [138], tunable lasers [139], and nonlinear signal processing [126].

Chapter 5

Conclusion

Here has been presented work on several optical resonator systems: the single and double-metal plasmonic photonic crystal resonator, the double-disk whispering-gallery cavity, and the double-ring spiderweb cavity. Each of these resonator designs was developed and optimized for a particular range of applications, and each has been shown to be effective in at least initial demonstrations.

Multispectral mid-infrared resonant detectors were demonstrated with enhanced responsivity and detectivity, and tailorable polarization and spectral sensitivity. These devices were fabricated using a very simple single-etch process, and are detector agnostic, with design principles that are easily transferrable to any other detector material or frequency range with a minimum of difficulty. Expanding to a double-metal device structure, this method could be used to easily and inexpensively impart frequency and polarization selectivity, as well as absorption enhancement, to current detector focal plane array processing.

A novel optomechanical device structure has also been presented, consisting of two stacked microdisks with an optically narrow gap between them. This device has a very large optomechanical coupling and a high quality factor, giving rise to extremely large dynamical backaction in the form of both regenerative mechanical oscillation and optomechanical cooling. Due to the large optical spring effect in these structures, we also demonstrate tunable coherent mechanical mode mixing with an analogy to electromagnetically induced transparency, showing the possibility for slow-light effects on the very long phononic timescale, and the potential for phonon-photon quantum state transfer.

Finally, an extremely flexible double-ring optomechanical device is shown, demonstrating all-optical wavelength routing with unprecedented range and efficiency, and 100% channel quality preservation. As this device can be easily integrated on-chip, it shows great promise for optical communications applications, as well as for more fundamental physics-based applications such as

in cavity quantum electrodynamics or for dispersion compensation in nonlinear optics.

Bibliography

[1] A. Rogalski, J. Antoszewski, and L. Faraone, "Third-generation infrared photodetector arrays," *Journal of Applied Physics* **105**, 091101 (2009).

[2] J. Phillips, "Evaluation of the fundamental properties of quantum dot infrared detectors," *Journal of Applied Physics* **91**, 4590–4594 (2002).

[3] Y. Sidorov, "Peculiarities of the MBE growth physics and technology of narrow-gap IIVI compounds," *Thin Solid Films* **306**, 253–265 (1997).

[4] S. Krishna, "Quantum dots-in-a-well infrared photodetectors," *Journal of Physics D: Applied Physics* **38**, 2142–2150 (2005).

[5] R. V. Shenoi, R. S. Attaluri, A. Siroya, J. Shao, Y. D. Sharma, A. Stintz, T. E. Vandervelde, and S. Krishna, "Low-strain InAs/InGaAs/GaAs quantum dots-in-a-well infrared photodetector," *Journal of Vacuum Science and Technology B* **26**, 1136–1139 (2008).

[6] O. Painter and K. Srinivasan, "Polarization properties of dipolelike defect modes in photonic crystal nanocavities," *Optics Letters* **27**, 339–341 (2002).

[7] M. Loncar, T. Yoshie, A. Scherer, P. Gogna, and Y. Qiu, "Low-threshold photonic crystal laser," *Applied Physics Letters* **81**, 2680–2682 (2002).

[8] O. Painter, J. Vuckovic, and A. Scherer, "Defect modes of a two-dimensional photonic crystal in an optically thin dielectric slab," *Journal of the Optical Society of America B: Optical Physics* **16**, 275–285 (1999).

[9] M. L. Althouse and C. I. Chang, "Chemical vapor detection with a multispectral thermal imager," *Optical Engineering* **30**, 1725–1733 (1991).

[10] H. Raether, *Surface Plasmons on Smooth and Rough Surfaces and on Gratings (Springer Tracts in Modern Physics)* (Springer, Berlin, 1988).

[11] B. Prade, J. Y. Vinet, and A. Mysyrowicz, "Guided optical waves in planar heterostructures with negative dielectric constant," *Physical Review B: Condensed Matter* **44**, 13556–13572 (1991).

[12] M. Bahriz, V. Moreau, R. Colombelli, O. Crisafulli, and O. Painter, "Design of mid-IR and THz quantum cascade laser cavities with complete TM photonic bandgap," *Optics Express* **15**, 5948–5965 (2007).

[13] J. Rosenberg, R. V. Shenoi, T. E. Vandervelde, S. Krishna, and O. Painter, "A multispectral and polarization-selective surface-plasmon resonant midinfrared detector," *Applied Physics Letters* **95**, 161101 (2009).

[14] E. Homeyer, J. Houel, X. Checoury, F. Delgehier, S. Sauvage, P. Boucaud, R. Braive, L. Le Gratiet, L. Leroy, A. Miard, A. Lemaˆtre, and I. Sagnes, "Resonant coupling of quantum dot intersublevel transitions with midinfrared photonic crystal modes," *Applied Physics Letters* **95**, 041108 (2009).

[15] E. Laux, C. Genet, T. Skauli, and T. W. Ebbesen, "Plasmonic photon sorters for spectral and polarimetric imaging," *Nature Photonics* **2**, 161–164 (2008).

[16] J. K. Yang, M. K. Seo, I. K. Hwang, S. B. Kim, and Y. H. Lee, "Polarization-selective resonant photonic crystal photodetector," *Applied Physics Letters* **93**, 211103 (2008).

[17] X. Hu, M. Li, Z. Ye, W. Y. Leung, K. M. Ho, and S. Y. Lin, "Design of midinfrared photodetectors enhanced by resonant cavities with subwavelength metallic gratings," *Applied Physics Letters* **93**, 241108 (2008).

[18] J. S. White, G. Veronis, Z. Yu, E. S. Barnard, A. Chandran, S. Fan, and M. L. Brongersma, "Extraordinary optical absorption through subwavelength slits," *Optics Letters* **34**, 686–688 (2009).

[19] R. V. Shenoi, D. A. Ramirez, Y. Sharma, R. S. Attaluri, J. Rosenberg, O. J. Painter, and S. Krishna, "Plasmon assisted photonic crystal quantum dot sensors," vol. 6713, p. 67130P (SPIE, 2007).

[20] J. Rosenberg, R. V. Shenoi, S. Krishna, and O. Painter, "Design of plasmonic photonic crystal resonant cavities for polarization sensitive infrared photodetectors," *Opt. Express* **18**, 3672–3686 (2010).

[21] M. Tinkham, *Group Theory and Quantum Mechanics* (Dover Publications, New York, NY, 2003).

[22] O. Painter, K. Srinivasan, and P. E. Barclay, "Wannier-like equation for the resonant cavity modes of locally perturbed photonic crystals," *Physical Review B: Condensed Matter* **68**, 035214 (2003).

[23] J. D. Joannopoulos, R. D. Meade, and J. N. Winn, *Photonic Crystals* (Princeton University Press, Princeton, New Jersey, 1995).

[24] W. L. Barnes, A. Dereux, and T. W. Ebbesen, "Surface plasmon subwavelength optics," *Nature* **424**, 824–830 (2003).

[25] J. B. Pendry, L. Martin-Moreno, and F. J. Garcia-Vidal, "Mimicking Surface Plasmons with Structured Surfaces," *Science* **305**, 847–848 (2004).

[26] P. B. Johnson and R. W. Christy, "Optical Constants of the Noble Metals," *Physical Review B: Condensed Matter* **6**, 4370–4379 (1972).

[27] M. Cai, O. Painter, and K. J. Vahala, "Observation of Critical Coupling in a Fiber Taper to a Silica-Microsphere Whispering-Gallery Mode System," *Physical Review Letters* **85**, 74–77 (2000).

[28] T. E. Vandervelde, M. C. Lenz, E. Varley, A. Barve, J. Shao, R. V. Shenoi, D. A. Ramirez, W. Jan, Y. D. Sharma, and S. Krishna, "Quantum Dots-in-a-Well Focal Plane Arrays," *IEEE Journal of Selected Topics in Quantum Electronics* **14**, 1150–1161 (2008).

[29] V. B. Braginsky and A. B. Manukin, *Measurements of Weak Forces in Physics Experiments* (The University of Chicago Press, Chicago, IL, 1977).

[30] C. Caves, K. S. Thorne, R. W. P. Drever, V. D. Sandberg, and M. Zimmermann, "On the measurement of a weak classical force coupled to a quantum-mechanical oscillator," *Reviews of Modern Physics* **52**, 341–392 (1980).

[31] A. Abramovici, W. E. Althouse, R. W. P. Drever, Y. Gursel, Seiji, D. Shoemaker, L. Sievers, R. E. Spero, K. S. Thorne, R. E. Voigt, R. Weiss, S. E. Whitcomb, and M. E. Zucker, "LIGO: The Laser Interferometer Gravitational-Wave Observatory," *Science* **256**, 325 (1992).

[32] C. A. Regal, J. D. Tuefel, and K. W. Lehnert, "Measuring nanomechanical motion with a microwave cavity interferometer," *Nature Physics* **4**, 555–560 (2008).

[33] V. B. Braginsky, F. Y. Khalili, and K. S. Thorne, *Quantum Measurement* (Cambridge University Press, Cambridge, UK, 1995).

[34] T. J. Kippenberg and K. J. Vahala, "Cavity Optomechanics: Back-Action at the Mesoscale," *Science* **321**, 1172–1176 (2008).

[35] T. J. Kippenberg, H. Rokhsari, T. Carmon, A. Scherer, and K. J. Vahala, "Analysis of Radiation-Pressure Induced Mechanical Oscillation of an Optical Microcavity," *Physical Review Letters* **95**, 033901 (2005).

[36] S. Gigan, H. R. Bohm, M. Paternostro, F. Blaser, G. Langer, J. B. Hertzberg, K. C. Schwab, D. Bauerle, M. Aspelmeyer, and A. Zeilinger, "Self-cooling of a micromirror by radiation pressure." *Nature* **444**, 67–70 (2006).

[37] O. Arcizet, P. F. Cohadon, T. Briant, M. Pinard, and A. Heidmann, "Radiation-pressure cooling and optomechanical instability of a micromirror," *Nature* **444**, 71–73 (2006).

[38] D. Kleckner and D. Bouwmeester, "Sub-kelvin optical cooling of a micromechanical resonator," *Nature* **444**, 75–78 (2006).

[39] A. Schliesser, P. Del'haye, N. Nooshi, K. J. Vahala, and T. J. Kippenberg, "Radiation Pressure Cooling of a Micromechanical Oscillator Using Dynamical Backaction," *Physical Review Letters* **97**, 243905 (2006).

[40] J. D. Thompson, B. M. Zwickl, A. M. Jayich, F. Marquardt, S. M. Girvin, and J. G. E. Harris, "Strong dispersive coupling of a high-finesse cavity to a micromechanical membrane," *Nature* **452**, 72–75 (2008).

[41] A. Schliesser, R. Riviere, G. Anetsberger, O. Arcizet, and T. J. Kippenberg, "Resolved-sideband cooling of a micromechanical oscillator," *Nature Physics* **4**, 415–419 (2008).

[42] M. L. Povinelli, S. G. Johnson, M. Loncar, M. Ibanescu, E. J. Smythe, F. Capasso, and J. D. Joannopoulos, "High-Q enhancement of attractive and repulsive optical forces between coupled whispering-gallery-mode resonators," *Optics Express* **13**, 8287–8295 (2005).

[43] P. T. Rakich, M. A. Popovic, M. Soljacic, and E. P. Ippen, "Trapping, corralling and spectral bonding of optical resonances through optically induced potentials," *Nature Photonics* **1**, 658–665 (2007).

[44] M. Li, W. H. P. Pernice, C. Xiong, T. Baehr-Jones, M. Hochberg, and H. X. Tang, "Harnessing optical forces in integrated photonic circuits," *Nature* **456**, 480–484 (2008).

[45] M. Eichenfield, R. Camacho, J. Chan, K. J. Vahala, and O. Painter, "A picogram- and nanometre-scale photonic-crystal optomechanical cavity," *Nature* **459**, 550–555 (2009).

[46] J. K. H. Horber and M. J. Miles, "Scanning Probe Evolution in Biology," *Science* **302**, 1002–1005 (2003).

[47] J. Arlett, "Properties of piezoresistive silicon nano-scale cantilevers with applications to BioNEMS," Ph.D. thesis, California Institute of Technology (2006).

[48] Q. Lin, J. Rosenberg, X. Jiang, K. J. Vahala, and O. Painter, "Mechanical Oscillation and Cooling Actuated by the Optical Gradient Force," *Physical Review Letters* **103**, 103601 (2009).

[49] P. Meystre, E. M. Wright, J. D. Mccullen, and E. Vignes, "Theory of radiation-pressure-driven interferometers," *Journal of the Optical Society of America B: Optical Physics* **2**, 1830–1840 (1985).

[50] T. J. Kippenberg and K. J. Vahala, "Cavity Opto-Mechanics," *Optics Express* **15**, 17172–17205 (2007).

[51] G. Anetsberger, O. Arcizet, Q. P. Unterreithmeier, E. M. Weig, J. P. Kotthaus, and T. J. Kippenberg, "Near-field cavity optomechanics with nanomechanical oscillators," *Nature Physics* **5**, 909–914 (2009).

[52] S. S. Verbridge, R. Illic, H. G. Craighead, and J. M. Parpia, "Size and frequency dependent gas damping of nanomechanical resonators," *Applied Physics Letters* **93**, 013101 (2008).

[53] R. Kubo, *A Stochastic Theory of Line Shape* (John Wiley & Sons, New York, NY, 1969).

[54] H. J. Kimble and L. Mandel, "Resonance fluorescence with excitation of finite bandwidth," *Physical Review A: Atomic, Molecular, and Optical Physics* **15**, 689–699 (1977).

[55] B. S. Sheard, M. B. Gray, C. M. Mow Lowry, D. E. McClelland, and S. E. Whitcomb, "Observation and characterization of an optical spring," *Physical Review A: Atomic, Molecular, and Optical Physics* **69**, 051801 (2004).

[56] P. F. Cohadon, A. Heidmann, and M. Pinard, "Cooling of a Mirror by Radiation Pressure," *Physical Review Letters* **83**, 3174–3177 (1999).

[57] F. Marquardt, J. P. Chen, A. A. Clerk, and S. M. Girvin, "Quantum theory of cavity-assisted sideband cooling of mechanical motion," *Physical Review Letters* **99**, 093902 (2007).

[58] I. W. Rae, N. Nooshi, W. Zwerger, and T. J. Kippenberg, "Theory of ground state cooling of a mechanical oscillator using dynamical backaction," *Physical Review Letters* **99**, 093901 (2007).

[59] T. J. Kippenberg, J. Kalkman, A. Polman, and K. J. Vahala, "Demonstration of an erbium-doped microdisk laser on a silicon chip," *Physical Review A: Atomic, Molecular, and Optical Physics* **74**, 051802 (2006).

[60] T. D. Stowe, K. Yasumura, T. W. Kenny, D. Botkin, K. Wago, and D. Rugar, "Attonewton force detection using ultrathin silicon cantilevers," *Applied Physics Letters* **71**, 288–290 (1997).

[61] M. Notomi, H. Taniyama, S. Mitsugi, and E. Kuramochi, "Optomechanical Wavelength and Energy Conversion in High-Q Double-Layer Cavities of Photonic Crystal Slabs," *Physical Review Letters* **97**, 023903 (2006).

[62] U. Fano, "Effects of Configuration Interaction on Intensities and Phase Shifts," *Physical Review Online Archive (Prola)* **124**, 1866–1878 (1961).

[63] S. E. Harris, J. E. Field, and A. Imamoglu, "Nonlinear optical processes using electromagnetically induced transparency," *Physical Review Letters* **64**, 1107–1110 (1990).

[64] J. Faist, F. Capasso, C. Sirtori, K. W. West, and L. N. Pfeiffer, "Controlling the sign of quantum interference by tunnelling from quantum wells," *Nature* **390**, 589–591 (1997).

[65] M. Kroner, A. O. Govorov, S. Remi, B. Biedermann, S. Seidl, A. Badolato, P. M. Petroff, W. Zhang, R. Barbour, B. D. Gerardot, R. J. Warburton, and K. Karrai, "The nonlinear Fano effect," *Nature* **451**, 311–314 (2008).

[66] J. F. Scott, "Soft-mode spectroscopy: Experimental studies of structural phase transitions," *Reviews of Modern Physics* **46**, 83 (1974).

[67] M. Hase, J. Demsar, and M. Kitajima, "Photoinduced Fano resonance of coherent phonons in zinc," *Physical Review B: Condensed Matter* **74**, 212301 (2006).

[68] S. E. Harris, "Lasers without inversion: Interference of lifetime-broadened resonances," *Physical Review Letters* **62**, 1033–1036 (1989).

[69] D. E. Nikonov, A. Imamoglu, and M. O. Scully, "Fano interference of collective excitations in semiconductor quantum wells and lasing without inversion," *Physical Review B: Condensed Matter* **59**, 12212–12215 (1999).

[70] S. Fan, "Sharp asymmetric line shapes in side-coupled waveguide-cavity systems," *Applied Physics Letters* **80**, 908–910 (2002).

[71] D. D. Smith, H. Chang, K. A. Fuller, A. T. Rosenberger, and R. W. Boyd, "Coupled-resonator-induced transparency," *Physical Review A: Atomic, Molecular, and Optical Physics* **69**, 063804 (2004).

[72] Q. Xu, S. Sandhu, M. L. Povinelli, J. Shakya, S. Fan, and M. Lipson, "Experimental Realization of an On-Chip All-Optical Analogue to Electromagnetically Induced Transparency," *Physical Review Letters* **96**, 123901 (2006).

[73] K. Totsuka, N. Kobayashi, and M. Tomita, "Slow Light in Coupled-Resonator-Induced Transparency," *Physical Review Letters* **98**, 213904 (2007).

[74] N. Liu, L. Langguth, T. Weiss, J. Kastel, M. Fleischhauer, T. Pfau, and H. Giessen, "Plasmonic analogue of electromagnetically induced transparency at the Drude damping limit," *Nature Materials* **8**, 758–762 (2009).

[75] Q. Lin, J. Rosenberg, D. Chang, R. Camacho, M. Eichenfield, K. J. Vahala, and O. Painter, "Coherent mixing of mechanical excitations in nano-optomechanical structures," *Nature Photonics* (2010). doi:10.1038/nphoton.2010.4.

[76] M. L. Povinelli, M. Loncar, M. Ibanescu, E. J. Smythe, S. G. Johnson, F. Capasso, and J. D. Joannopoulos, "Evanescent-wave bonding between optical waveguides," *Optics Letters* **30**, 3042–3044 (2005).

[77] M. Eichenfield, C. P. Michael, R. Perahia, and O. Painter, "Actuation of micro-optomechanical systems via cavity-enhanced optical dipole forces," *Nature Photonics* **1**, 416–422 (2007).

[78] J. Rosenberg, Q. Lin, and O. Painter, "Static and dynamic wavelength routing via the gradient optical force," *Nature Photonics* **3**, 478–483 (2009).

[79] A. Ashkin, "History of optical trapping and manipulation of small-neutral particle, atoms, and molecules," *IEEE Journal of Selected Topics in Quantum Electronics* **6**, 841–856 (2000).

[80] M. H. Zadeh and K. J. Vahala, "Observation of optical spring effect in a microtoroidal optomechanical resonator," *Optics Letters* **32**, 1611–1613 (2007).

[81] T. Corbitt, C. Wipf, T. Bodiya, D. Ottaway, D. Sigg, N. Smith, S. Whitcomb, and N. Mavalvala, "Optical Dilution and Feedback Cooling of a Gram-Scale Oscillator to 6.9 mK," *Physical Review Letters* **99**, 160801 (2007).

[82] J. Chan, M. Eichenfield, R. Camacho, and O. Painter, "Optical and mechanical design of a "zipper" photonic crystal optomechanical cavity," *Optics Express* **17**, 3802–3817 (2009).

[83] M. Fleischhauer, A. Imamoglu, and J. P. Marangos, "Electromagnetically induced transparency: Optics in coherent media," *Reviews of Modern Physics* **77**, 633–673 (2005).

[84] M. Bao and H. Yang, "Squeeze film air damping in MEMS," *Sensors and Actuators A: Physical* **136**, 3–27 (2007).

[85] A. S. Barker and J. J. Hopfield, "Coupled-optical-phonon-mode theory of the infrared dispersion in $BaTiO_3$, $SrTiO_3$, and $KTaO_3$," *Physical Review Online Archive (Prola)* **135**, A1732–A1737 (1964).

[86] D. L. Rousseau and S. P. S. Porto, "Auger-Like Resonant Interference in Raman Scattering from One- and Two-Phonon States of $BaTiO_3$," *Physical Review Letters* **20**, 1354–1357 (1968).

[87] J. F. Scott, "Hybrid Phonons and Anharmonic Interactions in $AlPO_4$," *Physical Review Letters* **24**, 1107–1110 (1970).

[88] A. Zawadowski and J. Ruvalds, "Indirect Coupling and Antiresonance of Two Optic Phonons," *Physical Review Letters* **24**, 1111–1114 (1970).

[89] A. Chaves, R. S. Katiyar, and S. P. S. Porto, "Coupled modes with $A1$ symmetry in tetragonal $BaTiO_3$," *Physical Review B: Condensed Matter* **10**, 3522–3533 (1974).

[90] C. L. G. Alzar, M. A. G. Martinez, and P. Nussenzveig, "Classical analog of electromagnetically induced transparency," *American Journal of Physics* **70**, 37–41 (2002).

[91] P. R. Hemmer and M. G. Prentiss, "Coupled-pendulum model of the stimulated resonance Raman effect," *Journal of the Optical Society of America B: Optical Physics* **5**, 1613–1623 (1988).

[92] C. Liu, Z. Dutton, C. H. Behroozi, and L. V. Hau, "Observation of coherent optical information storage in an atomic medium using halted light pulses," *Nature* **409**, 490–493 (2001).

[93] M. Bajcsy, A. S. Zibrov, and M. D. Lukin, "Stationary pulses of light in an atomic medium," *Nature* **426**, 638–641 (2003).

[94] M. Fatih and S. Fan, "Stopping Light All Optically," *Physical Review Letters* **92**, 083901 (2004).

[95] M. F. Yanik and S. Fan, "Stopping and storing light coherently," *Physical Review A: Atomic, Molecular, and Optical Physics* **71**, 013803 (2005).

[96] G. Anetsberger, R. Riviere, A. Schliesser, O. Arcizet, and T. J. Kippenberg, "Ultralow-dissipation optomechanical resonators on a chip," *Nature Photonics* **2**, 627–633 (2008).

[97] Q. Xu, P. Dong, and M. Lipson, "Breaking the delay-bandwidth limit in a photonic structure," *Nature Physics* **3**, 406–410 (2007).

[98] S. S. Verbridge, H. G. Craighead, and J. M. Parpia, "A megahertz nanomechanical resonator with room temperature quality factor over a million," *Applied Physics Letters* **92**, 013112 (2008).

[99] R. G. Beausoleil, P. J. Kuekes, G. S. Snider, S.-Y. Wang, and R. S. Williams, "Nanoelectronic and Nanophotonic Interconnect," *Proceedings of the IEEE* **96**, 230–247 (2008).

[100] J. Berthold, A. A. M. Saleh, L. Blair, and J. M. Simmons, "Optical networking: past, present, and future," *Journal of Lightwave Technology* **26**, 1104–1118 (2008).

[101] J. Gripp, M. Duelk, J. E. Simsarian, A. Bhardwaj, P. Bernasconi, O. Laznicka, and M. Zirngibl, "Optical switch fabrics for ultra-high-capacity IP routers," *Journal of Lightwave Technology* **21**, 2839 (2003).

[102] J. Strand and A. Chiu, "Realizing the advantages of optical reconfigurability and restoration with integrated optical cross-connects," *Journal of Lightwave Technology* **21**, 2871 (2003).

[103] D. T. Neilson, C. R. Doerr, D. M. Marom, R. Ryf, and M. P. Earnshaw, "Wavelength selective switching for optical bandwidth management," *Bell Labs Technical Journal* **11** (2006).

[104] D. Sadot and E. Boimovich, "Tunable optical filters for dense WDM networks," *IEEE Communications Magazine* **36**, 50–55 (1998).

[105] L. Eldada, "Optical communication components," *Review of Scienti c Instruments* **75**, 575–593 (2004).

[106] W. J. Tomlinson, "Evolution of passive optical component technologies for fiber-optic communication systems," *Journal of Lightwave Technology* **26**, 1046–1063 (2008).

[107] B. E. Little, J. S. Foresi, G. Steinmeyer, E. R. Thoen, S. T. Chu, H. A. Haus, E. P. Ippen, L. C. Kimerling, and W. Greene, "Ultra-compact Si-SiO_2 microring resonator optical channel dropping filters," *IEEE Photonics Technology Letters* **10**, 549–551 (1998).

[108] Y. Yi, P. Bermel, K. Wada, X. Duan, J. D. Joannopoulos, and L. C. Kimerling, "Tunable multichannel optical filter based on silicon photonic band gap materials actuation," *Applied Physics Letters* **81**, 4112 (2002).

[109] P. Rabiei and W. H. Steier, "Tunable polymer double micro-ring filters," *IEEE Photonics Technology Letters* **15**, 1255–1257 (2003).

[110] T. Asano, W. Kunishi, M. Nakamura, B. S. Song, and S. Noda, "Dynamic wavelength tuning of channel-drop device in two-dimensional photonic crystal slab," *Electronics Letters* **41**, 37–38 (2005).

[111] J. K. S. Poon, Y. Huang, G. T. Paloczi, A. Yariv, C. Zhang, and L. R. Dalton, "Wide-range tuning of polymer microring resonators by the photobleaching of CLD-1 chromophores," *Optics Letters* **29**, 2584–2586 (2004).

[112] Q. Xu, B. Schmidt, S. Pradhan, and M. Lipson, "Micrometre-scale silicon electro-optic modulator," *Nature* **435**, 325–327 (2005).

[113] V. S. Ilchenko and A. B. Matsko, "Optical resonators with whispering-gallery modes-Part II: applications," *IEEE Journal on Selected Topics in Quantum Electronics* **12**, 15–32 (2006).

[114] M. C. Wu, O. Solgaard, and J. E. Ford, "Optical MEMS for lightwave communication," *Journal of Lightwave Technology* **24**, 4433–4454 (2006).

[115] C. Monat, P. Domachuk, and B. J. Eggleton, "Integrated optofluidics: A new river of light," *Nature Photonics* **1**, 106–114 (2007).

[116] F. Xia, M. Rooks, L. Sekaric, and Y. Vlasov, "Ultra-compact high order ring resonator filters using submicron silicon photonic wires for on-chip optical interconnects," *Optics Express* **15**, 11934–11941 (2007).

[117] N. S. Droz, H. Wang, L. Chen, B. G. Lee, A. Biberman, K. Bergman, and M. Lipson, "Optical 4x4 hitless silicon router for optical networks-on-chip (NoC)," *Optics Express* **16**, 15915–15922 (2008).

[118] Y. Vlasov, W. M. J. Green, and F. Xia, "High-throughput silicon nanophotonic wavelength-insensitive switch for on-chip optical networks," *Nature Photonics* **2**, 242–246 (2008).

[119] I. Fushman, E. Waks, D. Englund, N. Stoltz, P. Petroff, and J. Vucković, "Ultrafast nonlinear optical tuning of photonic crystal cavities," *Applied Physics Letters* **90**, 091118 (2007).

[120] M. Yano, F. Yamagishi, and T. Tsuda, "Optical MEMS for photonic switching-compact and stable optical crossconnect switches for simple, fast, and flexible wavelength applications in recent photonic networks," *IEEE Journal on Selected Topics in Quantum Electronics* **11**, 383–394 (2005).

[121] A. Dorsel, J. D. Mccullen, P. Meystre, E. Vignes, and H. Walther, "Optical Bistability and Mirror Confinement Induced by Radiation Pressure," *Physical Review Letters* **51**, 1550–1553 (1983).

[122] M. Eichenfield and O. J. Painter, "Optomechanics of Strongly Coupled Stacked Monolithic Microdisks," in *Conference on Lasers and Electro-Optics/Quantum Electronics and Laser*

Science Conference and Photonic Applications Systems Technologies (Optical Society of America, 2008).

[123] G. S. Wiederhecker, L. Chen, A. Gonarenko, and M. Lipson, "Controlling photonic structures using optical forces," *Nature* **462**, 633–636 (2009).

[124] A. J. Seeds and K. J. Williams, "Microwave Photonics," *Journal of Lightwave Technology* **24**, 4628–4641 (2006).

[125] I. Favero and K. Karrai, "Optomechanics of deformable optical cavities," *Nature Photonics* **3**, 201–205 (2009).

[126] G. P. Agrawal, *Nonlinear Fiber Optics 4th ed* (Academic Press, New York, NY, 2007).

[127] Q. Lin, O. J. Painter, and G. P. Agrawal, "Nonlinear optical phenomena in silicon waveguides: modeling and applications," *Optics Express* **15**, 16604–16644 (2007).

[128] Q. Lin, T. J. Johnson, R. Perahia, C. P. Michael, and O. J. Painter, "A proposal for highly tunable optical parametric oscillation in silicon micro-resonators," *Optics Express* **16**, 10596–10610 (2008).

[129] J. J. Blech, "On isothermal squeeze films," *Journal of Lubrication Technology* **105**, 615–620 (1983).

[130] T. Veijola, H. Kuisma, J. Lahdenperä, and T. Ryhänen, "Equivalent-circuit model of the squeezed gas film in a silicon accelerometer," *Sensors and Actuators A: Physical* **48**, 239–248 (1995).

[131] R. G. Christian, "The theory of oscillating-vane vacuum gauges," *Vacuum* **16**, 175–178 (1966).

[132] M. Bao, H. Yang, H. Yin, and Y. Sun, "Energy transfer model for squeeze-film air damping in low vacuum," *Journal of Micromechanics and Microengineering* **12**, 341–346 (2002).

[133] R. B. Bhiladvala and Z. J. Wang, "Effect of fluids on the Q factor and resonance frequency of oscillating micrometer and nanometer scale beams," *Physical Review E: Statistical, Nonlinear, and Soft Matter Physics* **69**, 036307 (2004).

[134] S. S. Verbridge, J. M. Parpia, R. B. Reichenbach, L. M. Bellan, and H. G. Craighead, "High quality factor resonance at room temperature with nanostrings under high tensile stress," *Journal of Applied Physics* **99**, 124304 (2006).

[135] P. Del'haye, A. Schliesser, O. Arcizet, T. Wilken, R. Holzwarth, and T. J. Kippenberg, "Optical frequency comb generation from a monolithic microresonator," *Nature* **450**, 1214–1217.

[136] M. Ferrera, L. Razzari, D. Duchesne, R. Morandotti, Z. Yang, M. Liscidini, J. E. Sipe, S. Chu, B. E. Little, and D. J. Moss, "Low-power continuous-wave nonlinear optics in doped silica glass integrated waveguide structures," *Nature Photonics* **2**, 737–740 (2008).

[137] N. K. Fontaine, J. Yang, Z. Pan, S. Chu, W. Chen, B. E. Little, and S. J. B. Yoo, "Continuously Tunable Optical Buffering at 40 Gb/s for Optical Packet Switching Networks," *Journal of Lightwave Technology* **26**, 3776–3783 (2008).

[138] C. K. Madsen, G. Lenz, A. J. Bruce, M. A. Cappuzzo, L. T. Gomez, and R. E. Scotti, "Integrated all-pass filters for tunable dispersion and dispersion slope compensation," *IEEE Photonics Technology Letters* **11**, 1623–1625 (1999).

[139] M. C. Y. Huang, Y. Zhou, and C. J. C. Hasnain, "A nanoelectromechanical tunable laser," *Nature Photonics* **2**, 180–184 (2008).